



Aalborg Universitet

AALBORG UNIVERSITY  
DENMARK

## Probabilistic analysis methods for support structures

*Work Package - D7.42*

Gintautas, Tomas; Sørensen, John Dalsgaard; Natarajan, Anand; Wandji, Wilfried Njomo; Dimitrov, Nikolay Krasimirov; Ehrmann, Andreas; Hübler, Clemens; Schmoor, Kirill; Pfaffel, Sebastian; Faulstich, Stefan

*Creative Commons License*  
Unspecified

*Publication date:*  
2018

*Document Version*  
Publisher's PDF, also known as Version of record

[Link to publication from Aalborg University](#)

*Citation for published version (APA):*

Gintautas, T., Sørensen, J. D., Natarajan, A., Wandji, W. N., Dimitrov, N. K., Ehrmann, A., Hübler, C., Schmoor, K., Pfaffel, S., & Faulstich, S. (2018). *Probabilistic analysis methods for support structures: Work Package - D7.42*. European Commission \* Office for Official Publications of the European Union.

### General rights

Copyright and moral rights for the publications made accessible in the public portal are retained by the authors and/or other copyright owners and it is a condition of accessing publications that users recognise and abide by the legal requirements associated with these rights.

- Users may download and print one copy of any publication from the public portal for the purpose of private study or research.
- You may not further distribute the material or use it for any profit-making activity or commercial gain
- You may freely distribute the URL identifying the publication in the public portal -

### Take down policy

If you believe that this document breaches copyright please contact us at [vbn@aub.aau.dk](mailto:vbn@aub.aau.dk) providing details, and we will remove access to the work immediately and investigate your claim.



## Integrated Research Programme on Wind Energy

Project acronym: **IRPWIND**  
Grant agreement n° 609795  
Collaborative project  
Start date: 01<sup>st</sup> December 2013  
Duration: 4 years

## Probabilistic analysis methods for support structures Work Package – D7.42

Lead Beneficiary:  
Delivery date:  
Dissemination level: PU



The research leading to these results has received funding from the European Union Seventh Framework Programme under the agreement 609795.

**Author(s) information (alphabetical):**

Name	Organisation	Email
Tomas Gintautas	AAU	tg@civil.aau.dk
John Dalsgaard Sørensen	AAU	jds@civil.aau.dk
Anand NatarajanWilfried N. Wandji	DTU Wind Energy	wilw@dtu.dk
Nikolay Dimitrov	DTU Wind Energy	
Andreas Ehrmann	ForWind-Hannover	a.ehrmann@isd.uni-hannover.de
Clemens Hübler	ForWind-Hannover	c.huebler@isd.uni-hannover.de
Kirill Schmoor	ForWind-Hannover	schmoor@igth.uni-hannover.de
Sebastian Pfaffel	Fraunhofer IEE	sebastian.pfaffel@iee.fraunhofer.de
Stefan Faulstich	Fraunhofer IEE	stefan.faulstich@iee.fraunhofer.de

**Acknowledgements/Contributions:**

Name	Name	Name

**Document Information**

Version	Date	Description		
1	28/02/2018	Initial Version		
		<b>Name</b>	<b>Prepared by</b>	<b>Reviewed by</b>
			Kim Branner	All
				<b>Approved by</b>
				All

**Definitions**

## Table of Contents

Integrated Research Programme on Wind Energy .....	1
Probabilistic analysis methods for support structures .....	1
Work Package – D7.42.....	1
Executive Summary: .....	1
1. Reliability Assessment of conical grouted joint .....	3
1.1 Introduction .....	3
1.2 Bolted Joints .....	4
1.3 Estimation of stress concentration factors at Welded Joints.....	5
1.3.1. Strength limit state .....	6
1.4 Metocean conditions.....	7
1.5 Finite Element Modeling of the Grouted Joint.....	9
1.6 Limit states for the conical grouted joint design.....	10
1.6.1 Limit states related to extreme events.....	10
1.6.2 Limit states related to fatigue .....	10
1.7 Design for Fatigue of the Grouted Joint.....	11
1.7.1 Vertical settlement.....	13
1.8 Design for Extremes .....	15
1.8.1. Dimensionality reduction and parametrization.....	15
1.8.2 Simulation of Extreme Response of Grouted Joint.....	18
1.8.3 Prediction of the extreme settlement .....	20
2. Reliability assessment of grouted joint with shear keys .....	22
2.1 Target reliability levels .....	22
2.1 Deterministic assessment of concrete grout fatigue resistance .....	23
2.1.1 Deterministic assessment according to DNVGL-ST-C502.....	23
2.1.2 Deterministic assessment according to fib Model Code 2010 .....	24
2.2 Reliability assessment of grouted joint – Concrete grout fatigue .....	27
2.2.1 Stochastic model for concrete grout fatigue.....	28
2.2.2 Results of concrete grout reliability analysis.....	30
2.3 Reliability assessment of grouted joint – fatigue of welded steel details.....	34
2.3.1 Stochastic model for steel fatigue .....	34
2.3.2 Results steel fatigue reliability analysis .....	38
2.4 Concluding remarks on reliability of tubular grouted connection with shear keys	41
3. Reliability of piles and substructures under consideration of soil parameters .....	42
3.1 Reliability of the substructure under consideration of the turbine and soil	
parameters .....	42
3.1.1 Introduction .....	43
3.1.2 Determination of the model error .....	44
3.1.2.1 Design methods .....	44
3.1.2.2 Calculated tension capacity of tested piles .....	45
3.1.2.3 Derivation of the model error .....	46
3.1.3 Assesment of design methods.....	52
3.1.3.1 Pile-Soil System under consideration .....	52
3.1.3.2 Deterministic design .....	53
3.1.3.3 Stochastic soil model.....	55
3.1.3.4 Reliability based design.....	58
3.1.3.5 Comparison of deterministic and reliability based design.....	59
3.1.3.6 Evaluation of design methods.....	60

3.1.4	Summary and Conclusion.....	62
3.2	Reliability of the substructure under consideration of the turbine and soil parameters .....	64
3.2.1	Introduction and concept .....	64
3.2.2	Wind turbine model.....	65
3.2.2.1	Time domain model .....	65
3.2.2.2	Soil model for transient calculations .....	66
3.2.2.3	Assessment of basic soil models with data from WP7.2 .....	76
3.2.3	Statistical distributions of input parameters.....	83
3.2.4	Sensitivity analysis.....	86
3.2.5	Deterministic and probabilistic design .....	89
3.2.6	Damage distribution and failure probabilities .....	91
3.2.7	Summary and conclusion .....	94
4.	Failure statistics and current reliability level (Fraunhofer IEE) .....	95
4.1	Design and System Boundary of Support Structures (Fraunhofer IEE).....	96
4.2	Failure Modes of Support Structures (Fraunhofer IEE) .....	97
5.	References .....	99

## Executive Summary:

This report describes aspects of probabilistic analysis for offshore substructures and the results obtained in various illustrative investigations. This includes probabilistic modeling of model uncertainties using results from WP7.2 and WP7.3 on experimental data and conventional design approaches.

Since no failures / collapses of wind turbine support structures are reported in the literature / available databases statistical analyses have not been performed to assess the reliability level. However, failures of the grouting in a large number of grouted monopiles have been observed. These failures which can be considered as design errors / lack of knowledge seem only to have resulted in local failures without collapse of the substructures, but have required various mitigation efforts incl. extensive inspection and monitoring programs. For new designs the problem with groutings has resulted in changed designs with e.g. shear keys or conical joints. The target reliability level in the design standards for substructures corresponds to an annual probability of failure equal to approximately  $10^{-4}$  –  $5 \cdot 10^{-5}$ .

Reliability analysis of offshore support structures can be performed using structural reliability methods implying formulation of limit state equations for the critical failure modes due to extreme loads and fatigue, and establishment of stochastic models for the uncertain parameters in the limit state equations incl. physical, statistical and model uncertainties. The probability of failure can be estimated by simulation techniques or First/Second Order Reliability Methods.

For the grouted joints a number of limit state equations are formulated related to critical failure modes, including failure of the grout concrete in extreme loading and fatigue, and fatigue failure for the welded steel details. Additionally, stochastic models are established. Reliability analyses are performed using the limit states and illustrated for the 10 MW reference wind turbine substructure for which load effects are obtained for extreme loads, and combined stress ranges and mean stresses are obtained for fatigue analyses using a detailed finite element modelling of the grouted connection.

For extreme loading failure of the concrete in shear and compression is investigated as well as critical vertical settlement. Further, failure of the concrete in fatigue is considered. Among others, the results show that the reliability level is sufficient related to settlement of transition piece keeping the gap between the pile top edge and the jacking brackets below 72 mm.

Fatigue reliability of concrete grout and steel components of grouted connection with shear keys was assessed and found to be satisfactory at this stage of preliminary design. The results show that the concrete grout reliability models are highly sensitive to model errors related to the estimation of the SN curve, especially for the 'compression to tension' case where more test data are required. The reliability analyses of fatigue failure of the welded steel details show a satisfactory reliability level, assuming cathodic protection during the whole lifetime but also high sensitivity to assessment of the load stress ranges

and stress concentration/magnification factor calculations. Additionally, the results show that for welds in both the monopile and transition piece larger initial cracks could be allowed potentially reducing the manufacturing costs of monopiles and transition pieces.

For the geotechnical reliability assessment of foundation piles typical offshore soil and foundation pile properties for offshore wind converters in the North Sea were assumed. Five different design methods for the determination of the axial tensile resistance were considered, and 60 deterministic designs were evaluated within a reliability based design. Typical variability for the assumed soil condition and estimated model uncertainties were applied for a reliability based estimation of failure probabilities in terms of reliability indices. A new calibration approach was developed to determine the global safety factor for a prescribed acceptable failure probability. Further, quality factors were derived for each design method as function of the load, pile diameter, and soil density.

Nest, probabilistic calculations of fully coupled offshore wind turbines were considered in order to assess the reliability of substructures, based on sophisticated, non-linear aero-elastic simulations, and furthermore, to create the basis for safety factor (SF) calibration. It can be concluded that SFs can be reduced if probabilistic calculations are performed implying possible weight saving potentials. The results also include global sensitivity analyses whereby the most influential probabilistic parameters were identified showing that wind and wave, and some soil parameters, have to be modelled by probabilistic models.

# 1. Reliability Assessment of conical grouted joint

## 1.1 Introduction

Offshore wind turbine support structures for wind turbines typically possess welded, bolted, or grouted joints. Most joints in the tower and substructure (monopile, jacket) are usually welded joints. For monopiles, the connection between the cylindrical pile and the tower is conventionally made using a grouted joint (Dallyn, et al., 2015). The tower sections can also have bolted sections, typically ring flange connections that link different sections of the tower together. The grouts at the transition between tower and monopile may often be the weakest link in the overall support structure due to the action of the cyclic loading from the wind turbine on the concrete material in the grout (Schaumann, et al., 2013).

The fatigue design of grouted joints is influenced mainly by crushing and cracking of the concrete grout layer, especially under tensile cyclic stresses common in wind turbine operation. If this joint is instead made into a bolted joint, then several bolts are needed along the circumference of two flanged intersections connecting the tower and monopile (Madsen, et al., 2017). Classically, the grouted joints for monopile substructures are built from the overlap of two cylindrical tubes: a transition piece and a pile, and the resulting annular gap is filled with a high strength concrete. The grouted joints are efficient as they are easily constructible and they serve to correct the pile misalignment due to driving errors (Schaumann, et al., 2013) as presented in Figure 1.

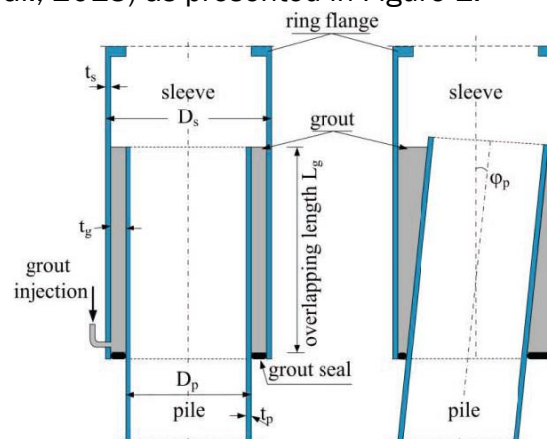


**Figure 1. Grouted joint with plain cylindrical tubes** Error! Reference source not found..

A typical construction process follows few steps: (1) the transition piece is jacked up at the pile top edge using holding brackets; (2) the concrete is poured in the annulus and left for curing; and (3) after the concrete has hardened, the jack-ups are removed and the transition piece holds due to the passive friction resistance at the contact faces between the layers. The passive friction resistance is made of two contributions, which are the chemical adhesive bond between the concrete and the steel and the mechanical interlock between the rough concrete surface and the undulations on the steel surfaces. An additional contribution, Coulomb friction, is generated during the loading operations by the normal-to-the-interface components of the loads transferred from the transition piece to the pile.

After few cycles, gaps open between the grout and the steel walls at the connection top and bottom; the adhesive bond deteriorates and cannot recover. Furthermore, the friction abrades the geometrical imperfections at the adjacent surfaces over the whole

connection length. At very early age of the structure, the two initial contributions depreciate and only the coulomb friction persists, which is only effective when the normal pressure is present. In case of insignificant normal pressure, the shear resistance may not support the structure weight anymore and the transition piece will progressively slide downwards till the jacking brackets touch the pile top edge: the connection fails.

In order to constantly keep the shear resistance, two principal grouted solutions were proposed (Lotsberg, 2013): the conical grouted joint and the shear-keyed grouted joints. Fig. 2 illustrated both proposed solutions.

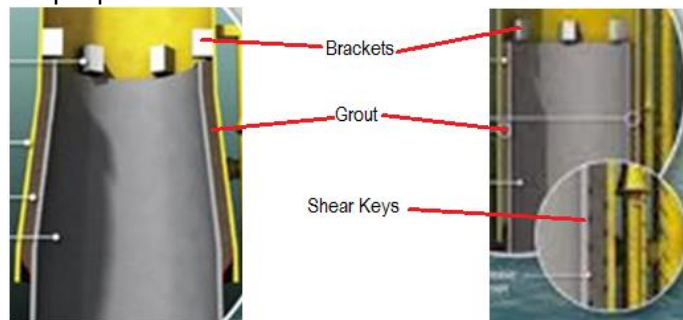


**Figure 2. Conical grouted joint (left) and shear-keyed cylindrical grouted joint**

The conical grouted joint is derived by imposing a small conical angle ( $1^\circ$  to  $3^\circ$ ) to the overlapping tubes. With the conical angle, the effect of the structure weight on the connection decomposes into a shear component along the contact faces and a normal component to the contact faces. The latter component generates a permanent coulomb friction resistance, which prevents the failure described above.

## 1.2 Bolted Joints

Instead of a grouted joint, the bottom of the tower may also be bolted directly to the monopile or to the top of the transition piece (TP) by the use of flanges connected to the tubular shells. The ultimate and fatigue limit states of the bolted-flange connection are governed by different failure modes of the bolted connection, which can be evaluated using available analytical methods given in (IEC 61400-6, 2017). The failure of the bolt is usually a combination of plastic yielding of the shell (plastic hinge) and failure of the bolt in tension. The combined load cycles at the TP joint due to the cyclic loads from the wind turbines are obtained using HAWC2 simulations of the DTU 10 MW turbine mounted on the monopile foundation (Santos, et al., 2017). Rainflow countings of the bending moments and axial force at the bolts are done to obtain the min-max and mean values of each load component.

However, the main limiting factor that prevents the design of the bolts is the lack of validated SN curves for the large diameter bolts needed at a 10 MW scale. The fatigue assessment for bolts under axial dynamic loading can be carried out according to the VDI guideline 2230 (Santos, et al., 2017). Available S-N curves are limited to nominal bolt sizes up to 40 mm. For 10 MW wind turbine, the bolt diameter at the tower base would need to be at least of the order of 80mm and this is twice that is usually analyzed using the VDI guidelines. Such large diameters would usually need to be handled in a conservative way, due to lack of sufficient information on the SN curves, thus leading to reduce fatigue strength or significantly increased monopile/transition piece thickness.

The effects of stress concentration factors/notch factors at the bolts, plastic yielding conditions and the uncertain SN curves leads to a high uncertainty of bolted connections for large offshore monopiles. The SN curve scaling or analysis of fatigue as a function of the component size can be made with advanced FE models along with material tests, but this is not feasible within the scope of this deliverable. Therefore this solution is not considered further herein.

### 1.3 Estimation of stress concentration factors at Welded Joints

The monopile, grout and transition piece have several welded connections between cylindrical sections. The hotspot at the welds stresses are evaluated using stress concentration factors (SCFs) at the weld connections. The weld connections of the appurtenances to the main steel are not studied here. For butt connections with same nominal diameter and thickness, (DNV-RP-C203, 2011) recommends estimating SCFs as in Equation (1):

$$SCF = 1 + \frac{3 \delta_m}{t} e^{-\sqrt{t/D}} \quad (1)$$

where  $D$  and  $t$  are respectively the outer diameter and the wall thickness,  $\delta_m = \sqrt{\delta_t^2 + \delta_r^2}$  is the resultant geometric imperfection measure, whose components are due to out-of-roundness or eccentricity. The actual imperfection measure is project dependent and brings uncertainties to the design procedure as it cannot accurately be predicted in advance. Imperfection levels,  $\lambda$ , can be defined as the ratios between the resultant geometric imperfection measure,  $\delta_m$ , and the admissible tolerance. Figure 3a illustrates the variation of SCF values in dependence of wall thickness and for various levels of imperfection. It is obvious that SCF equal one in case of no imperfection. It can be seen that, for small thicknesses, SCF values are very dispersed depending on the imperfection level. The dispersion reduces for large thicknesses. For a typical thickness of 100 mm, the SCFs vary between 1.0 and 1.8. In this study, a reference imperfection level of 0.50 is considered.

At butt welds where thicknesses change from a larger thickness  $T$  to a smaller thickness  $t$ , SCFs are calculated from Equation (2) (DNV-RP-C203, 2011):

$$SCF = 1 + \frac{6 (0.5(T - t) + \delta_m - \delta_0)}{t(1 + \left(\frac{T}{t}\right)^\beta)} e^{-\alpha} \quad (2)$$

$$\text{where } \alpha = \frac{1.82L}{\sqrt{Dt}} \frac{1}{1 + \left(\frac{T}{t}\right)^\beta}; \quad \beta = 1.5 - \frac{1.0}{\text{Log}\left(\frac{D}{t}\right)} + \frac{3.0}{\left[\text{Log}\left(\frac{D}{t}\right)\right]^2}; \quad \delta_0 = 0.1t$$

As per Figure 3b, SCF values related to thickness change vary by a factor of about 1.8 from zero imperfection till full allowable imperfection. For a given imperfection level, a large difference between the connected thicknesses will give a large SCF, which increases further if the thicknesses are small.

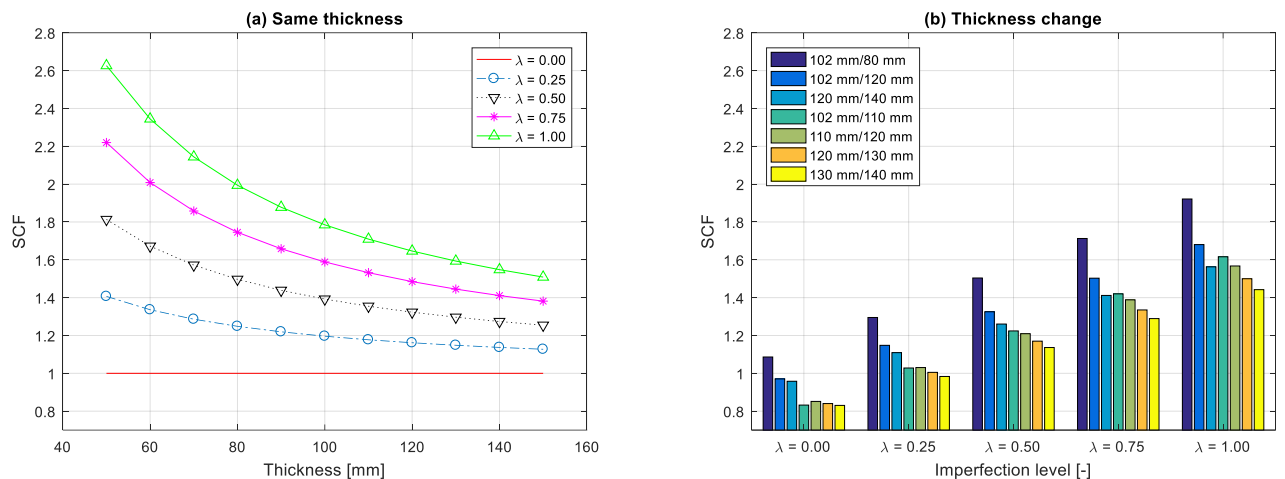


**Figure 3. Effect of the geometry imperfection on stress concentration factors for a) butt welds with same thickness and b) butt welds with varying thickness.**

Thus at the transition piece near the grouted joint, the welded connections can have large thickness thus supporting a large part of the load, but with small change in thickness between successive vertical sections. This will enable a low uncertainty in fatigue damage from stress concentration factors from the welded joints at the grouted connection.

### 1.3.1. Strength limit state

The steel strength and the pile stability are dependent on steel material properties, which are given in *Table 1*.

**Table 1: Steel properties of the monopile's material.**

Properties	References	Values
Steel type	DNV-OS-J101	High strength steel (HS) / NV-32
Minimum yield stress [MPa]	DNV-OS-J101	315
Mass density [ $\text{kg}/\text{m}^3$ ]	Cremer and Heckl	7850
Effective Elastic Modulus [GPa]	Cremer and Heckl	210
Poisson's ratio [-]	Cremer and Heckl	0.3

The main stress components at the transition piece are the longitudinal membrane stress, the shear stress, and the circumferential membrane stress (see Figure 4).

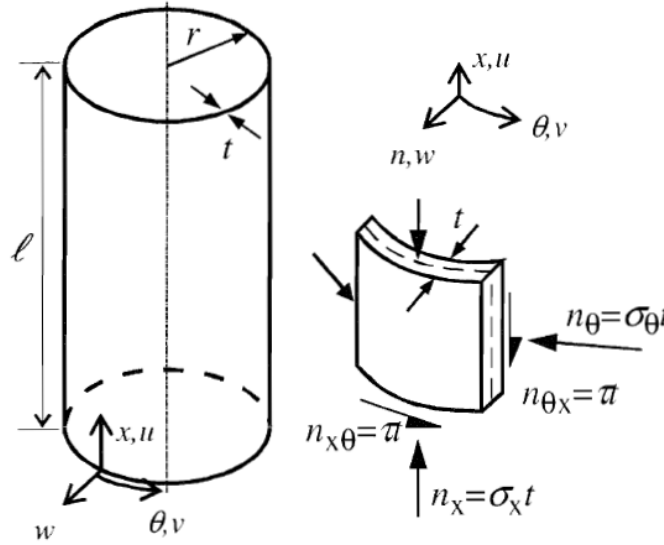


**Figure 4. Primary resulting stresses applied on a monopile shell.**

The longitudinal membrane stress and the shear stress are given by Equations (3) and (4), respectively:

$$\sigma_x = \frac{N}{A} + \frac{M_1}{I/R} \sin \theta - \frac{M_2}{I/R} \cos \theta \quad (3)$$

$$\tau = \left| \frac{T}{2\pi t R^2} - \frac{2Q_1}{A} \sin \theta + \frac{2Q_2}{A} \cos \theta \right| \quad (4)$$

The circumferential membrane stress is expressed as:

$$\sigma_\alpha = \frac{p(y)}{4\pi t} [4 - (\pi - 2\alpha)\sin\alpha] \quad (5)$$

where

- $N$  : axial force
- $M_1, M_2$  : bending moments about axis 1 and 2, respectively
- $T$  : torsional moment
- $Q_1, Q_2$  : shear forces along axis 1 and 2, respectively
- $p(y)$  : lateral force due to soil resistance
- $A$  : section's area
- $I$  : section's second moment of area
- $R$  : outer radius
- $t$  : wall thickness
- $\theta$  : circumferential co-ordinate, measured from axis 1
- $\alpha$  : circumferential co-ordinate, measured from the resultant horizontal force.

#### 1.4 Metocean conditions

Throughout this study, site specific metocean conditions, taken from (De Wries & et.al, 2011) are considered. The operational mean wind speed range varying from 4 m/s to 25 m/s is divided into 11 bins of 2 m/s width. An additional mean wind speed of 42.73 m/s accounts for extreme storms. The distribution of the wind direction is shown on Figure 5.

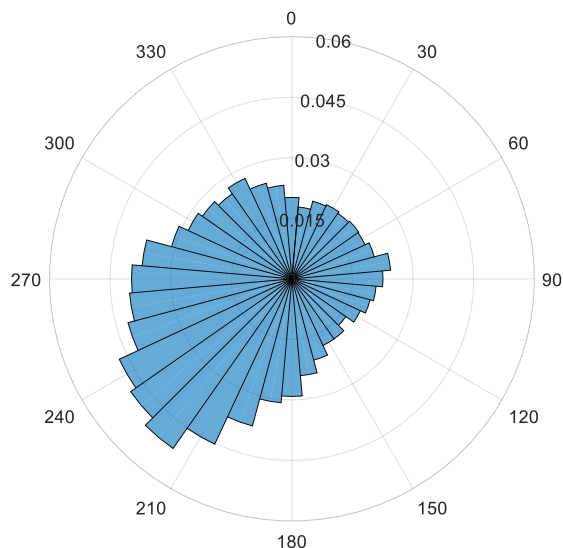


**Figure 5. Distribution of the wind direction (De Wries & et.al, 2011)**

Each mean wind speed bin is associated with expected sea states, i.e. significant wave height ( $H_s$ ) and peak spectral period ( $T_p$ ), and an expected annual frequency as shown in *Table 2* *Table 3* gives the respective characteristic turbulence intensities observed for each wind speed bin during normal turbulence and extreme turbulence together with the turbulence associated with the storm wind speed. The wave height is modelled based on either the JONSWAP spectrum (under extreme turbulence conditions or extreme wind conditions) or the Pierson-Moskowitz spectrum (under normal turbulence) at the expected value of the sea state characteristics conditional on the mean wind speed. The Pierson-Moskowitz type is used for fatigue load case simulations because of its wide-band energy distribution, while the JONSWAP type is suitable for ultimate load cases due to its peaked shape which can promote resonance if the peak coincides with the natural frequencies of the structure.

**Table 2: Environmental Conditions for mean wind speed and wave heights**

Wind speed [m/s]	Expected Significant height, $H_s$ [m]	Peak period, $T_p$ [s]	Expected annual frequency [%]
5	1.140	5.820	10.65
7	1.245	5.715	12.40
9	1.395	5.705	12.88
11	1.590	5.810	12.63
13	1.805	5.975	11.48
15	2.050	6.220	9.36
17	2.330	6.540	7.22
19	2.615	6.850	4.78
21	2.925	7.195	3.57
23	3.255	7.600	2.39

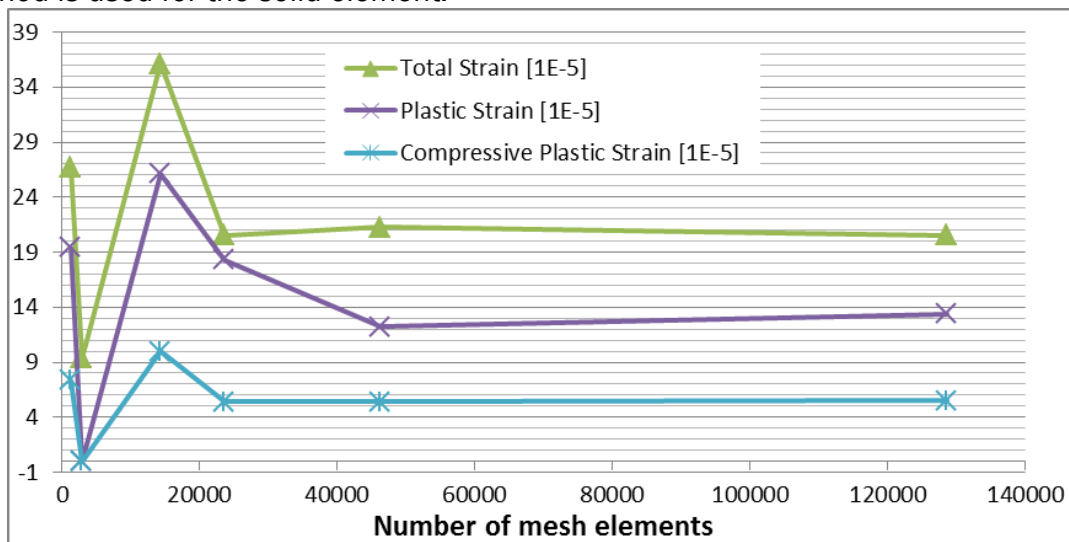
25	3.600	7.950	1.70
42.73 (Storm)	9.400	13.700	

**Table 3: Atmospheric turbulence for normal or extreme model.**

Wind speed [m/s]	5	7	9	11	13	15	17	19	21	23	25	42.73
<b>Normal Turbulence Intensity [%]</b>	18.95	16.75	15.60	14.90	14.40	14.05	13.75	13.50	13.35	13.20	13.00	11.00
<b>Extreme Turbulence Intensity [%]</b>	43.85	33.30	27.43	23.70	21.12	19.23	17.78	16.63	15.71	14.94	14.30	11.00

### 1.5 Finite Element Modeling of the Grouted Joint

A Finite Element model of the Grouted joint is developed in the MSC Abaqus software. (DNVGL-RP-0419, 2016) recommends to use 1<sup>st</sup> order shell elements for steel wall in conjunction with 1<sup>st</sup> order solid elements for the grout. This recommendation has been adopted for the finite element model prepared in this study. An aspect ratio equal to one has been used for all elements. For the steel wall, elements of type S4RS have been selected, which corresponds to 4-node doubly curved shell, reduced integration, hourglass control, small membrane strains. For the grout, elements of type C3D8R are selected, which corresponds to 8-node linear brick, reduced integration, hourglass control. The relax stiffness method is used to control hourglass for the shell element and the stiffness method is used for the solid element.


**Figure 6. Convergence analysis of strain with mesh size.**

With the setup described above, a convergence analysis was conducted in order to find out the appropriate size of a typical mesh element. Across the grout thickness, three finite elements are used in accordance to (DNVGL-RP-0419, 2016). Various analyses have been conducted

with different meshing arrangements. Several structural responses have been monitored at some selected hotspots; the results at one of them are shown in Figure 7. It can be seen that above 46500 mesh elements for the grout part, the structural responses converge; this corresponds to a mesh size of 20 cm x 20 cm for the connection (both grout and steel wall).

## 1.6 Limit states for the conical grouted joint design

### 1.6.1 Limit states related to extreme events

In the case of extreme loading, three failure modes can be distinguished for the grouted connection: failure of the steel-grout contacts, failure of the grout due to compressive stresses, and excessive vertical displacement of the transition piece relative to the pile. The shear stress,  $\tau$ , due to the friction between the steel wall and the grout surfaces should be lower than the shear strength,  $\tau_{max}$ , of the interface to prevent excessive relative motion between the transition piece and the pile (Eq. (6a)). This limit state is evaluated for both sides of the grout. The Tresca stress,  $\sigma_{Tresca}$ , generated in the grout material should be kept lower than the concrete strength,  $f_c$ , as specified by Eq. (6b). Moreover, the relative settlement,  $\Delta$ , of the transition piece with respect to the pile under extreme loading should be moderate and is limited to a vertical settlement  $h$  (See Eq. (7)).

$$g_1 = \tau_{max} - \tau \quad (6)$$

$$g_2 = f_c - \sigma_{Tresca} \quad (7)$$

$$g_3 = h - \Delta \quad (8)$$

The geometry of the grouted joint is considered deterministic. However, it has been varied within realistic bounds for the sensitivity analysis presented in subsequent sections. Table 4 tabulates the bounds used for the sensitivity analysis.

**Table 4: Bounds for the geometric parameters**

Parameters	Lower bounds	Nominal values	Upper bounds
Pile wall thickness, $t_p$ [m]	0.03	0.07	0.12
Transition wall thickness, $t_s$ [m]	0.03	0.06	0.12
Grout thickness, $t_g$ [m]	0.05	0.15	0.25
Length, $L$ [m]	9.00	18.00	25.00
Conical angle, $\alpha$ [deg]	0.10	3.00	5.00
Length of wall ends, $L_e$ [m]	0.10	0.50	1.00
Length of the connection above the msl, $L_t$ [m]	0.00	6.00	25.00

### 1.6.2 Limit states related to fatigue

Over the structure lifetime, failures associated to continual loadings can occur. They include

the wear of the grout surfaces in contact with steel walls, the reduction of the grout elastic modulus due to material degradation, the fatigue of the grout material, and the progressive vertical displacement of the transition piece relative to the pile as observed in some commercial wind systems. The friction at the contact faces abrades the grout surfaces. The wear rate is function of shear stress, which is proportional to the normal pressure exerted from one layer to another. In this paper, the wear phenomenon is not investigated as a more sophisticated finite element model is required for an accurate prediction of the phenomenon.

Two types of deterioration are engendered by continual loadings on grout material, fatigue damage and degradation, which are evaluated independently one to the other. The concrete degradation corresponds to a variation (diminution) of elastic modulus with the possibility of material recovery. As the word ‘grade’ is generally used to characterize grout material strength, the term ‘degradation’ refers to the loss of its elastic modulus. For the fatigue damage, the S-N curves have been calibrated based on samples that have been subjected to loadings till fatigue failure. During the experiments, the sample materials have been deteriorated continually and no full healing has been periodically assumed. So the extrapolation of the fatigue damage includes the progressive degradation of the grout material. Therefore, fatigue analyses do not require the monitoring of the damage parameters related to the degradation. However, it is relevant to monitor the damage parameters to check the crack apparition on the grout.

The reduction of the grout stiffness will be monitored based on the evolution of the material degradation parameters. It is important to keep the severely affected areas marginal in the grout in order to preserve the bending stiffness of the substructure. A change of the substructure bending stiffness can be noticed by following the lateral displacement of the interface for example. Subjected to cyclic loadings, the connection engenders cyclic stresses that induce fatigue in the materials. The accumulated fatigue,  $D_{25}$ , in the grout during the intended lifetime, calculated according to the Palmgren-Miner assumption should be lower than one (See Eq. 8)). The rate of progression of the long term vertical settlement,  $\delta$ , of the transition along the pile should be close to zero so that over years, the initial gap,  $g$ , between the pile top edge and the brackets (See Eq. (9)) does not completely close.

$$g_4 = 1.00 - D_{25} \quad (9)$$

$$g_5 = g - \delta_h \quad (10)$$

### 1.7 Design for Fatigue of the Grouted Joint

The occurrences of plastic strain generate degradation either of compressive ( $d_c$ ) or of tensile ( $d_t$ ) types in the grout material. The equivalent degradation ( $d$ ), which combines the effect of the compressive and of the tensile degradation, alters the elastic stiffness of the concrete:  $\mathbf{D}^{el}|_{t+\Delta t} = (1 - d|_{t+\Delta t})\mathbf{D}^{el}|_t$ , where  $\mathbf{D}^{el}$  is the material stiffness matrix.

The scalar degradation variable,  $d$ , is computed based on the tensile and compressive degradation variables:  $(1 - d) = (1 - s_t d_c)(1 - s_c d_t)$ .  $d_c$  and  $d_t$  are taken as the maxima between their respective previous state values and the present state values obtained by interpolation  $s_t = 1 - w_t r(\hat{\boldsymbol{\sigma}})$  and  $s_c = 1 - w_c(1 - r(\hat{\boldsymbol{\sigma}}))$ .  $w_t$  and  $w_c$  are the recovery factor.  $r(\hat{\boldsymbol{\sigma}}) = \sum_{i=1}^3 \langle \hat{\sigma}_i \rangle / \sum_{i=1}^3 |\hat{\sigma}_i|$  is a stress weight factor, equal to one if all principal stress components  $\hat{\sigma}_i$ , ( $i = 1, 2, 3$ ) are positive, or zero if they are negative.  $\langle \cdot \rangle$  is the Macaulay bracket.

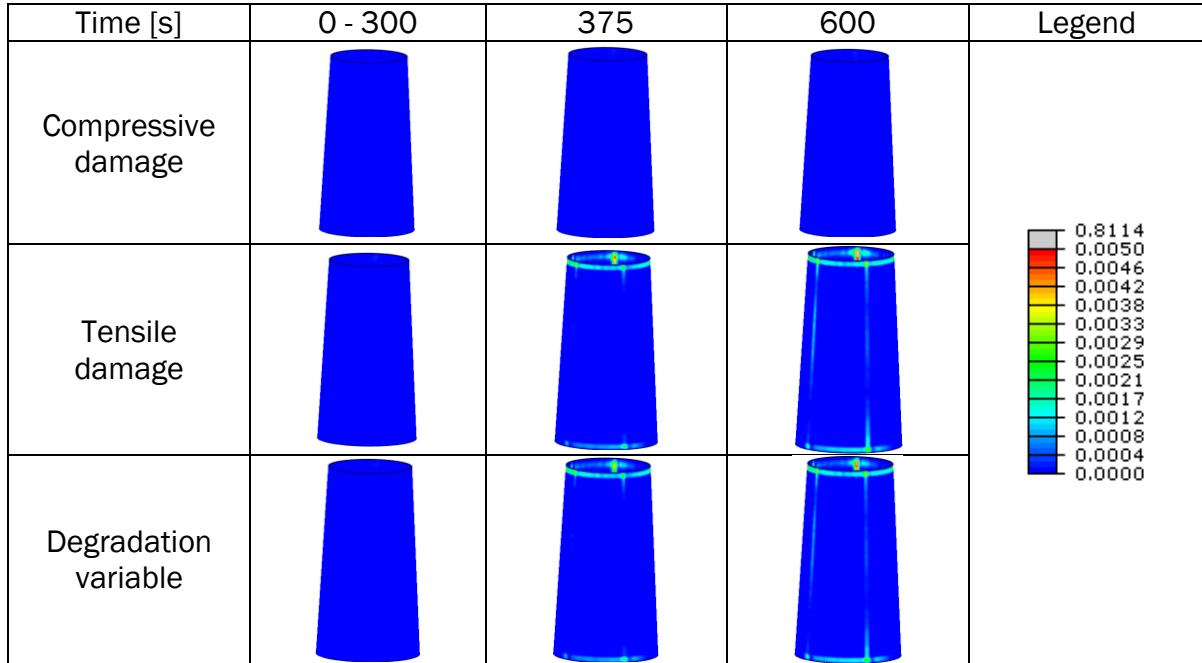


Figure 7. Degradation of the concrete material in the grout over time.

Fatigue damage accumulates over lifetime due to cyclic stresses presented above. (DNVGL-ST-0126, 2016) proposes an algorithm to estimate the total damage. The characteristic number of cycles to failure is calculated from:

$$\log N = \begin{cases} Y, & Y < X \\ Y(1 + 0.2(Y - X)), & Y \geq X \end{cases} \quad (11)$$

$$Y = C_1 \left( 1 - \frac{\sigma_{max}}{0.8f_{cn}/\gamma_m} \right) / \left( 1 - \frac{\sigma_{min}}{0.8f_{cn}/\gamma_m} \right); \quad X = C_1 / \left( 1 - \frac{\sigma_{min}}{0.8f_{cn}} + 0.1C_1 \right); \quad f_{cn} = f_{ck} \left( 1 - \frac{f_{ck}}{600} \right)$$

where

$\sigma_{max}, \sigma_{min}$  = are respectively the largest value of the maximum principal compressive stress during a stress cycle within the stress block and the smallest compressive stress in the same direction during this stress cycle. They are to be individually set to zero if they belong to the tensile range;

$\gamma_m = 1.5$  is the safety factor associated to the grout material;

$f_{ck}$  is the characteristic grout cylinder strength measured in MPa;

$C_1$  = calibration factor. For structures in water,  $C_1 = 10.0$  for compression-compression range and  $C_1 = 8.0$  for compression-tension range.

The damage accumulated over one year is linearly aggregated using Eq. (8); and the lifetime is calculated as  $L_f = D_1^{-1}$  and  $D_{25} = 25D_1$ .

$$D_1 = \gamma_{FF} \sum_i \frac{n_i(\Delta\sigma) t_i(\Delta\sigma)}{N_i(\Delta\sigma)} \quad (12)$$

where  $\gamma_{FF} = 3.0$  is the fatigue reserve factor and  $t_i(\Delta\sigma)$  is the occurrence frequency in one year of stress range  $\Delta\sigma$ , which is counted  $n_i(\Delta\sigma)$  times in the simulation time.

Figure 8 presents the spatial distribution of the fatigue damage accumulated over 25 years on an unrolled grout accounting for the full directionality of the loads. As the grout has been meshed in three layers across its thickness, the respective fatigue damage levels of the different

layers are shown. The maximum fatigue damage level is lower than one. The alignment of the peaks of fatigue damage on the surfaces suggests the nascence of the hairline cracks as indicated by the previous observations. It can also be noticed that fatigue affects the top edge of the grout on the transition face. This was expected as the highest compressive stresses are transferred from the transition piece to the pile through the grout top edge.

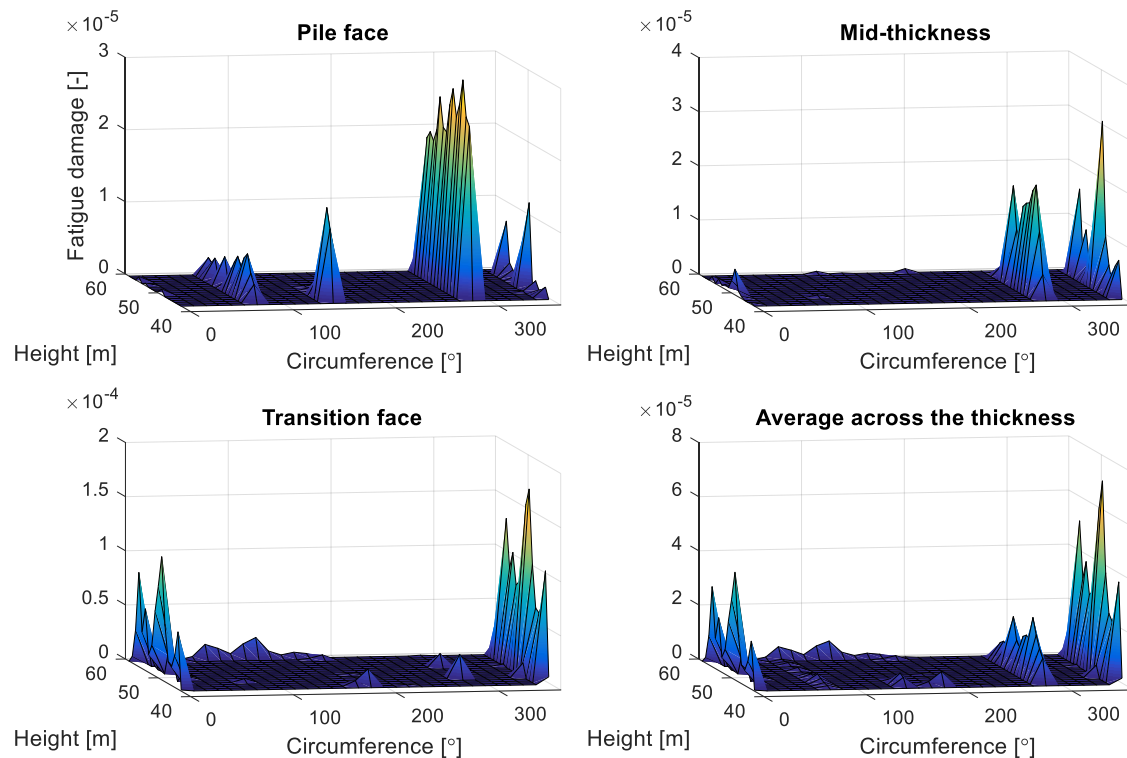


**Figure 8. Fatigue damage on unrolled grout over the lifetime for the reference grouted joint.**

The fatigue damage magnitudes indicate that the proposed design is not optimal with respect to the fatigue limit state. The sensitivities of the model parameters or the model uncertainties over time causing loss of stiffness has been evaluated based on a design of experiment and using analysis of variance. That has revealed that the wall thicknesses of the steel components influence most the fatigue lifetime. The essential conclusions based on this analysis is that amongst all the geometric and material factors affecting the fatigue damage of the grouted joint,

- 1) the wall thickness of the transition piece contributes to fatigue life at 46 % ,
- 2) the wall thickness of the pile contributes at 35 %.
- 3) The other variable contributions were: length of the grout at 10 %; conical angle, 3 %; pile's radius, 1 %; grout's elastic modulus, 1 %; steel's elastic modulus, 1 %; and loads (axial force, torsional moment, maximum bending moment, and minimum bending moment), 1%; grout's thickness, 0 %; contact friction, 0 %.

### 1.7.1 Vertical settlement

With the progressive degradation of the grout, the conical grouted joint could exhibit a gradual failure like the continuous settlement of the transition piece. (Schaumann, et al., 2013)

observed a continuous settlement of the transition piece on a cylindrical connection without shear keys where the passive shear resistance was due to coulomb friction and chemical adhesion. They have explained that the vertical displacement is caused by the reduction of coulomb friction when the transition piece approaches its neutral position, where the operational loads are small.

For the case of the conical grouted connection under the assumption that the shear resistance is only due to coulomb friction, a large amount of shear resistance is permanently due to the structural weight. Therefore, it is expected that with a sufficient conical angle, the settlement due to loss of coulomb friction is significantly reduced. With a conical angle of  $3^\circ$ , simulation results depicted in Fig. 9 show (i) an initial vertical settlement due to the application of the dead load; (ii) a slight gradual settlement due to the deformation of components (steel and grout) and grout degradation. For simulation of 600 s duration, the relationship between the grout degradation and the increase in vertical settlement can be observed in Figure 9 for 5m/s, 9m/s, 13 m/s and 17m/s mean wind speeds. As the degradation onsets in the grout at about 300 s, the vertical settlement increases at that instant but tends to stabilize notwithstanding the apparition of cracks. Furthermore, no trend change is observed during the 600 s simulation on the fore-aft and the side-side displacements, suggesting no significant loss of the support structure global bending stiffness during the simulation period. In case of bending stiffness reduction, the amplitudes of the side-side displacements would have increased and the means of the fore-aft displacements would have shifted.

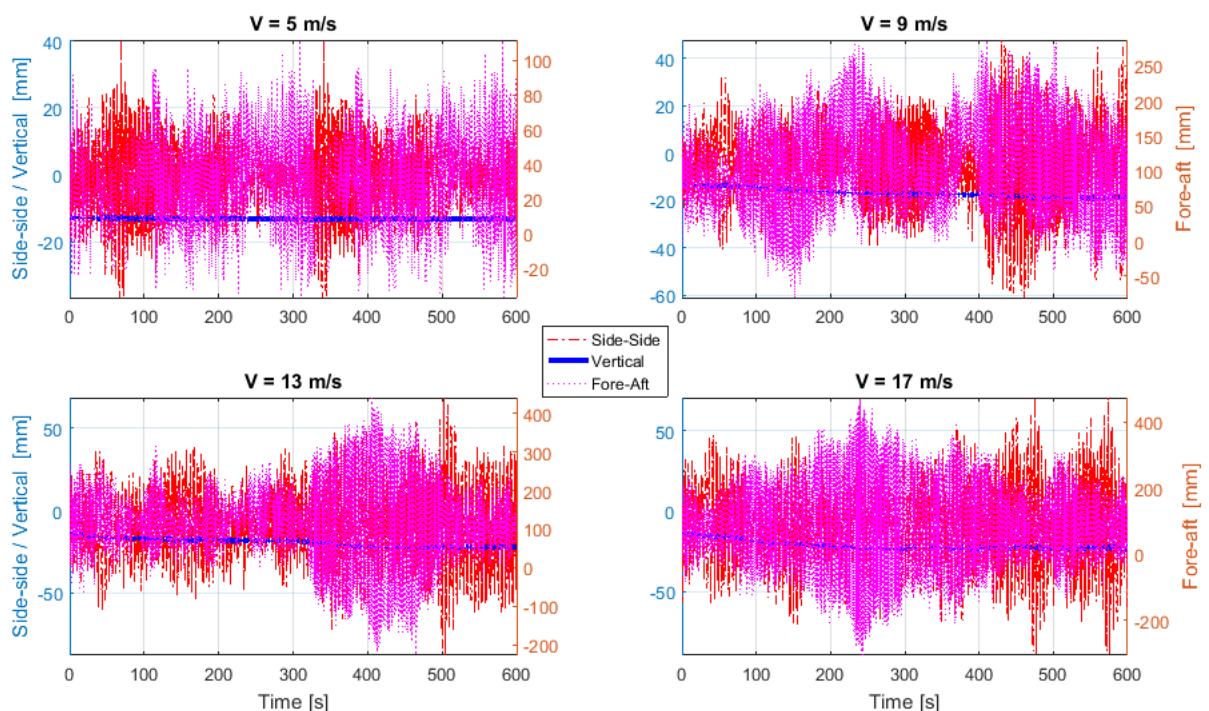


**Figure 9. Displacement history of the interface central node at several mean wind speeds.**

These observations are in line with the assumption that the hairline cracks do not significantly deter load transfer and also do not significantly elongate. Figure 10 shows that the rate of vertical settlement of the interface central node continuously stabilized over time even after 1800 s at rated wind speed.

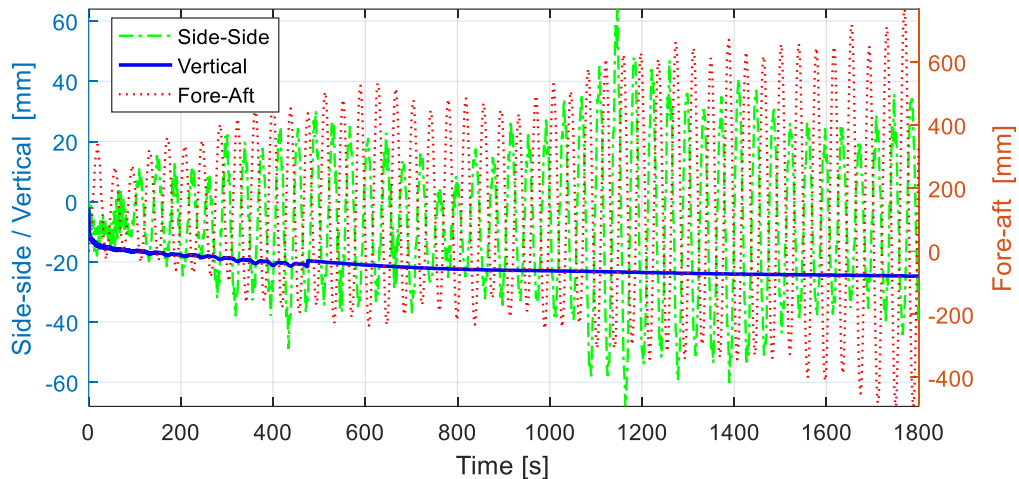


**Figure 10.** Displacement history of the interface central node at 11 m/s mean wind speed during 1800 s.

As the grout conical angle is varied from  $1^{\circ}$  to  $4^{\circ}$ , the loading corresponding to 11 m/s mean wind speed is applied on the structure during 600 s of simulations and the displacement of the interface is monitored. Depicted in Figure 11, the results show that both the initial settlement and the settlement rate reduce as the conical angle increases. For small conical angles, the settlement fails to stabilize during the 600 s, suggesting a continuous vertical displacement till failure. This indicates the necessity to choose a conical angle of at least 3 degs. to guarantee grouted joint stability.

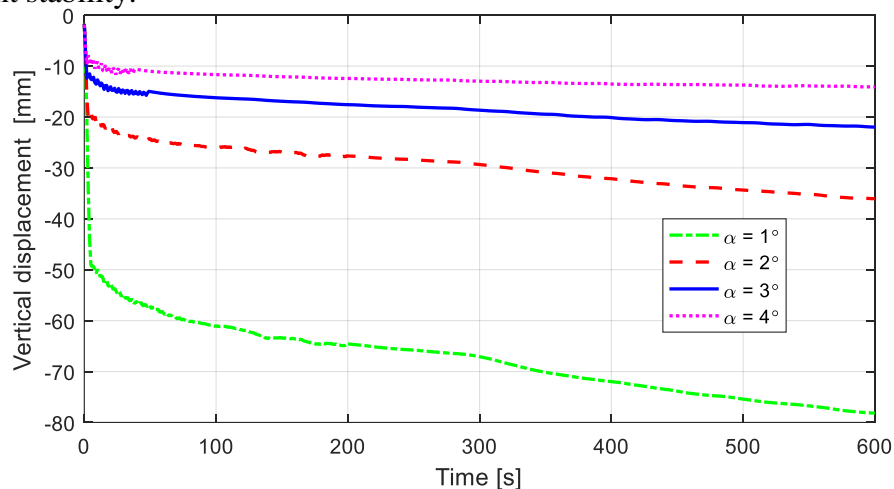


**Figure 11.** Influence of the conical angle on the vertical displacement of the interface for the reference grouted joint.

## 1.8 Design for Extremes

### 1.8.1. Dimensionality reduction and parametrization

Load assessment carried out in HAWC2 under metocean conditions described by Table 2 results in load time series collected at the monopile locations described in Fig.12. The locations are numbered from 1 to 11 from bottom to top (interface). For each location, six load time

series are obtained corresponding to each degree of freedom. Ideally, the ultimate structural responses should be obtained as the “maximum” of the structural response time series generated in the structure subjected to a set of load time series. This requires that the finite element analysis is done for 600 s for a given set of load time series, which is extremely computationally expensive.

In order to reduce the computational cost, it is assumed that the ultimate structural responses occur when loads are maximal i.e., when horizontal force, vertical force, bending moment, or torsional moment measured at the center of the grouted joint is extreme. This corresponds to four load criteria for vertical force, horizontal force, bending moment and torsion as depicted in Figure 12. Given a load criterion, the time instant at which its extreme is attained is identified and the other load components corresponding to this instant are collected to form the set of contemporaneous extreme nodal loads resulting from the load scenarios.

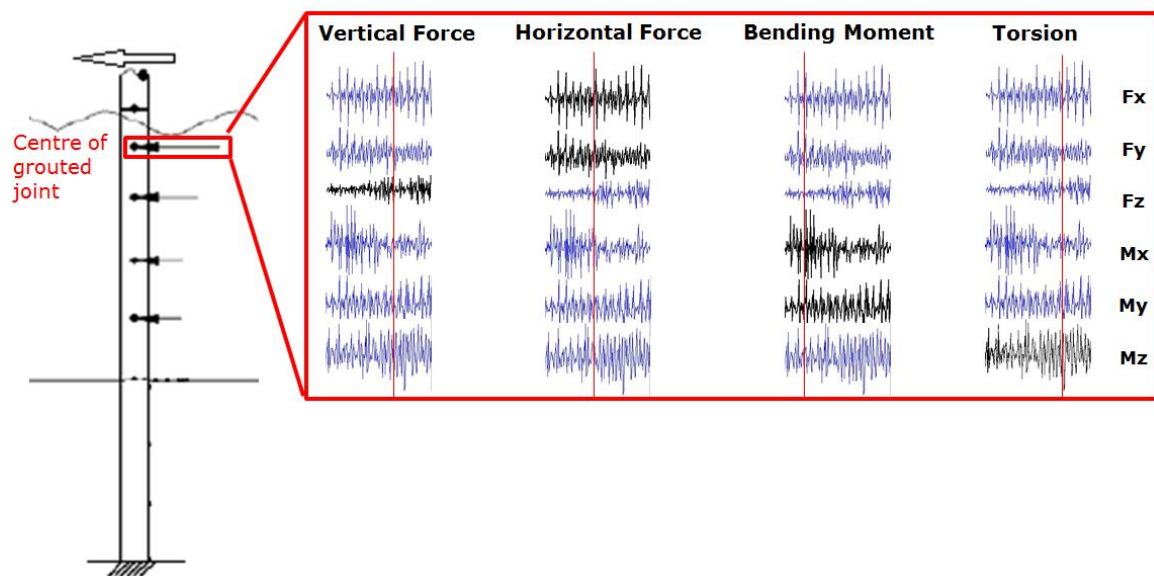


**Figure 12. Selection of nodal loads for finite element analysis.**

The resultant horizontal force is obtained as the Euclidean summation of the forces in x-direction and y-direction. At the time  $t_m$  when the extreme resultant horizontal force at the grouted joint center is attained, the load vector  $\langle F_x(t_m), F_y(t_m), F_z(t_m), M_x(t_m), M_y(t_m), M_z(t_m) \rangle$  is constructed for each of the 11 locations, which gives 66 nodal loads. This operation is repeated for the other three load criteria such that, to every load scenario, are related to four sets of 66 nodal loads.

It can be noted that the nodal loads of interest are not necessarily the extreme values of their time series, but the values that maximize the load criterion. Moreover, as results from HAWC2 are the internal loads at selected hotspots, the distributed external loads at the 10 locations (the interface is exempted) are estimated as the difference between two consecutive hotspots.

For the probabilistic study of the grouted joint, 500 data samples have been drawn from the load simulations and the corresponding nodal extreme loads are obtained from them as described above. Given a load criterion, each of the 66 nodal loads is established as a random variable numbered from 1 to 66: the first 6 variables are associated to location 1, the second 6

variables to location 2, and so forth. Figure 13 illustrates for the vertical force extreme criterion, the marginal distributions of the random variables numbered  $\{1 + 6i, i = 0, \dots, 10\}$ , which correspond to the side-side force  $F_x$  at the 11 locations, together with the correlation structure between the side-side loads at each of those locations. Obviously the correlation matrix in Fig. 13 is symmetric.

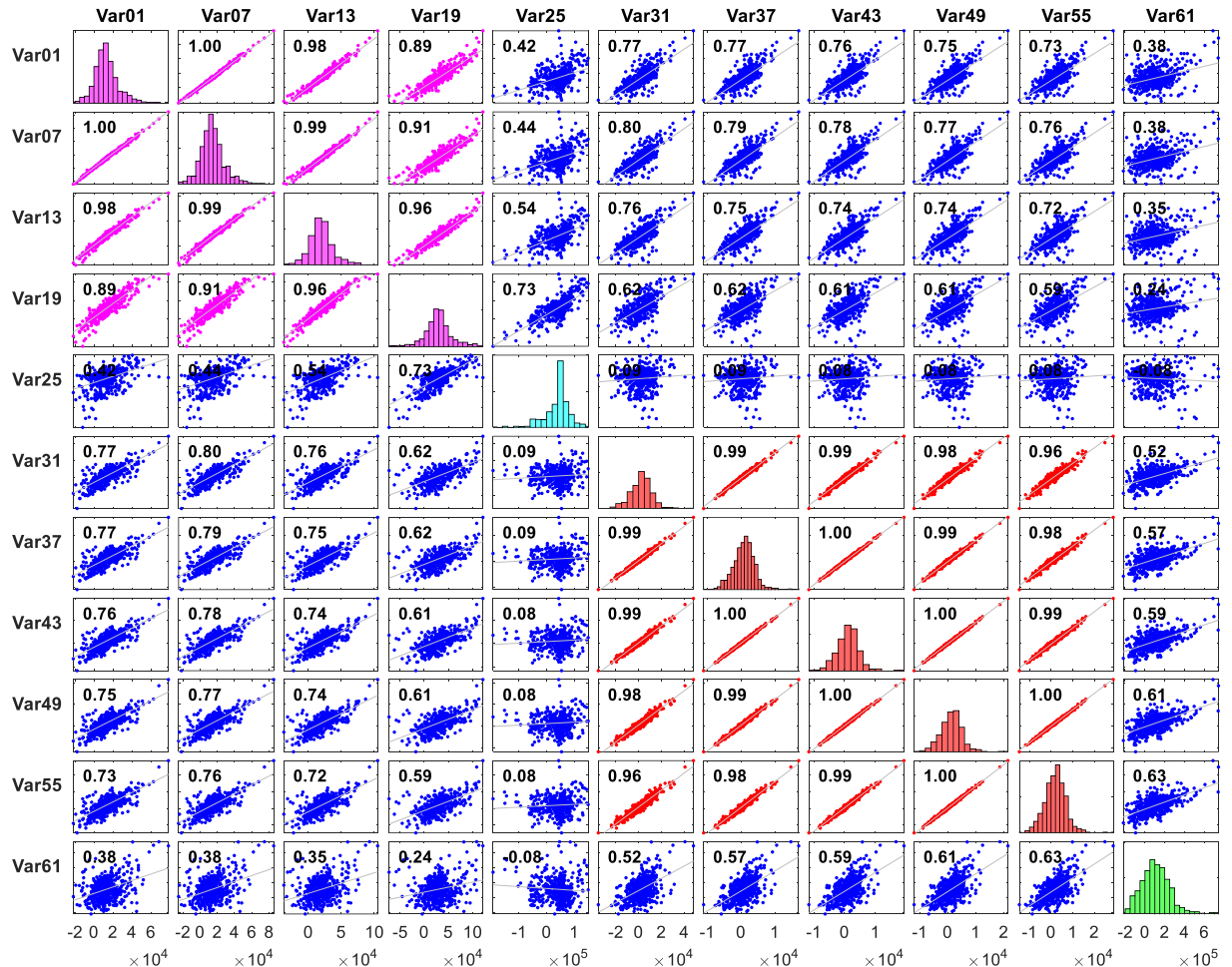


**Figure 13. Cross-correlation of the observed random variables  $F_x$  for the vertical force criterion. Pearson's correlation coefficients are indicated for each scatter plot. Units: Newton. Variables within blocks of same color are considered correlated.**

As it could be expected, some locations are highly correlated as grouped with color in Figure 13. Physically, the magenta-colored variables mainly represent the hydrodynamic load effects, the cyan-colored variable is the monopile section at the sea surface, the red-colored variables are primarily associated to the rotor driven loads, and the green-colored variable is the interface force in the side-side direction. This suggests that each group can be represented by one variable selected as insufficiently-correlated, and the other variables within the group are expressed in function of it. This reduces the set of 11 locations to four variables. The same operation is carried out for all degrees of freedom resulting in the dimension reduction from  $m = 66$  to  $n = 17$  variables for the case of horizontal force criterion and to  $n = 15$  variables for the other criteria.

If  $\mathbf{Z}$  denotes the insufficiently-correlated variables, the dependent variables,  $\mathbf{X}$  can be obtained by:

$$\mathbf{X}_{m \times 1} = \boldsymbol{\alpha}_{m \times n} \mathbf{Z}_{n \times 1} + \boldsymbol{\beta}_{m \times 1} \quad (13)$$

where  $\boldsymbol{\alpha}$  is the matrix of the scale factors obtained as the ratio of  $\mathbf{X}$ 's standard deviation over  $\mathbf{Z}$ 's standard deviation; and  $\boldsymbol{\beta}$  is the vector of the shifts obtained as the difference between the  $\mathbf{X}$ 's average and the  $\boldsymbol{\alpha}\mathbf{Z}$ 's average.

The marginals of the insufficiently-correlated variables are modeled with parametric probability density functions (PDFs). The Gumbel distribution is suitable to model extreme values. The difference of two Gumbel distributed variables follows a Logistic distribution. As nodal loads are obtained as the difference of loads possibly Gumbel-distributed, the Logistic distribution is applicable. The dependence structure within the sets of insufficiently-correlated variables,  $\mathbf{Z}$ , is captured using Gaussian copula, which results in the joint probability distribution of the set of the insufficiently-correlated random variables. Given the correlation matrix  $\mathbf{R}$  of  $\mathbf{Z}$ , the Gaussian copula is defined as  $c(u_1, \dots, u_n) = \Phi_{\mathbf{R}}(\Phi^{-1}(u_1), \dots, \Phi^{-1}(u_n))$ , where  $u_i = F_i(Z_i)$ ;  $F_i$  cumulative distribution function (CDF) of the insufficiently-correlated variable  $Z_i$ ;  $\Phi_{\mathbf{R}}(\cdot)$  is the joint cumulative distribution function of a n-dimension multivariate normal distribution with mean vector zero and covariance matrix equal to  $\mathbf{R}$ ; and  $\Phi^{-1}(\cdot)$  is the inverse cumulative distribution function of a standard normal.

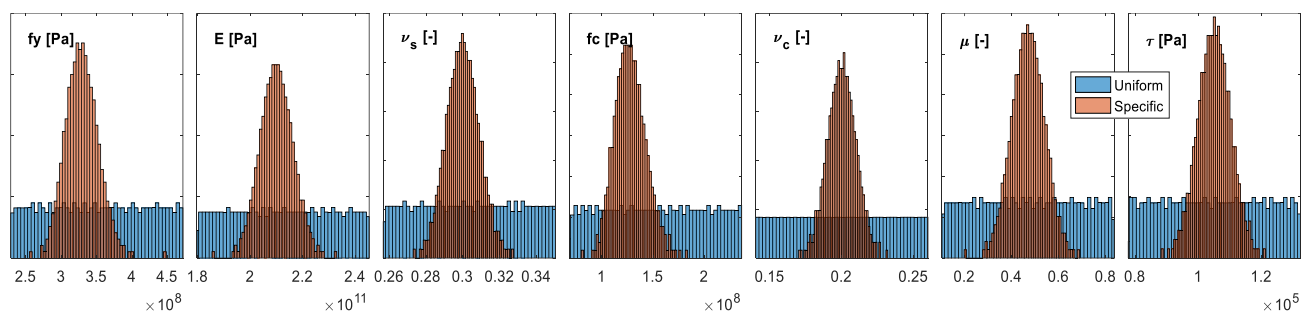
### 1.8.2 Simulation of Extreme Response of Grouted Joint

The accuracy of the constructed dependence structure in Eq. (12) has been evaluated by comparing the correlation matrix from the observed data versus that of synthetic data simulated from the constructed joint probability distribution. The root-mean-square deviations (RMSD) between the correlation matrices of the two data sets are determined to be 1.12 %, 0.85 %, 0.83 %, 0.60 % for the horizontal force, the vertical force, the bending moment, and the torsional moment criteria, respectively. Thus, random simulations of possible extreme load combinations at the grouted joint can be run using Eq. (12) for all the load criteria.

In addition, the variables related to the material properties have been independently and uniformly sampled between the bounds as per Table 5 and as relevant per the load case. The results are shown in Figure 14. The geometry-related variables are also independently and uniformly sampled between the bounds as indicated in The geometry of the grouted joint is considered deterministic. However, it has been varied within realistic bounds for the sensitivity analysis presented in subsequent sections. Table 4 tabulates the bounds used for the sensitivity analysis. With the 500 uniformly sampled variables describing loads, material properties as given in Figure 14, and geometry parameters described in Table 4, a batch of finite element simulations have been run in the Abaqus software.

**Table 5: Statistical description of the steel material**

Parameters	Characteristic value	Bias		
		Mean	Cov	Distribution
Density, $\rho_s$ [kN/m <sup>3</sup> ]	7850	Deterministic		
Yield strength (compr. and tension), $f_y$ [Pa]	$315 \times 10^6$	1.045	0.07	LN
Modulus of elasticity, $E$ [Pa]	$210 \times 10^9$	1.000	0.03	LN
Poisson's ratio, $\nu_s$ [-]	0.30	1.000	0.03	LN


**Figure 14. Uniformly sampled material properties to cover the design space for all the load criteria.**

The absolute maxima of the structural responses pertaining to extreme loading, which are the settlement of the transition piece relative to the pile, the Tresca equivalent stress in the concrete, the shear forces at both sides of the contact grout-steel, have been collected from the FE simulations. Figure 15 depicts the normalized safety margins for each structural response when the variables map the whole design space. The variation of stress and structural response captured in Figure 15 thus quantifies the effects of the model uncertainties and stochastic uncertainties as modeled used Eq. (12) and Table 5.

The safety margins are computed as the difference between the resistance parameters (see Eqs. 6 and 7) and the structural responses, respectively. In preparing Figure 15, the variable  $h$  in Eq. (7) has been set to 100 mm. The difference is then divided by the respective characteristic values of the resistance parameters to obtain the normalized safety margins. As can be seen in Figure 15, except for the vertical settlement, it can be noted that the safety margins of the other structural responses are all greater than zero, indicating that failure will not arise from these failure modes. Therefore, the rest of the analysis under extreme events will only focus on the failure mode respective to vertical displacement.

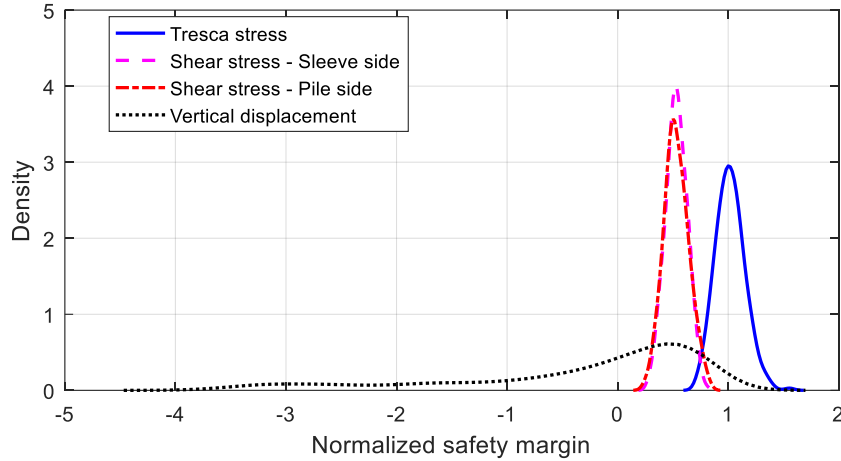


**Figure 15.** Normalized safety margins of the structural responses over the design space.

### 1.8.3 Prediction of the extreme settlement

From each point of the simulation batch of size  $N$  described in the last section, the maximum vertical displacements  $\Delta_i, i = 1, \dots, N$  are collected. Each can be seen as the peak of the time series of vertical displacement related to a given mean wind speed. In this sense, they are reasonably assumed to be independent and identically distributed random variables. With this assumption, the extreme value theory applies and the random variable  $\Delta_i$  follows the cumulative distribution function (CDF):

$$F_s(x|\mu, \sigma, \varepsilon) = \exp[-z(x|\mu, \sigma, \varepsilon)] \quad (14)$$

$\mu, \sigma, \varepsilon$  are the parameters of the CDF  $F_s$ , and  $z$  is a function of the random variable  $x$ . For the traditional extreme value families (Gumbel, Frechet, and Weibull (Natarajan & Holley, 2008),

$$z(x|\mu, \sigma, \varepsilon) = \left(1 + \varepsilon \frac{x-\mu}{\sigma}\right)^{-1/\varepsilon} \text{ with } x \in \begin{cases} [\mu - \frac{\sigma}{\varepsilon} + \infty), & \varepsilon > 0 \\ (-\infty + \infty), & \varepsilon \rightarrow 0 \\ (-\infty \mu - \frac{\sigma}{\varepsilon}], & \varepsilon < 0 \end{cases} \quad (15)$$

As a substitute of Eq. (11), studies (Natarajan & Holley, 2008), have proposed a quadratic shape for  $z$  such that

$$z(x|\mu, \sigma, \varepsilon) = \mu x^2 + \sigma x + \varepsilon \text{ with } x \in (-\infty + \infty) \quad (16)$$

and have shown its appropriateness and its robustness for fitting extreme structural responses of various wind turbine structures. Furthermore, the empirical CDF is generally constructed by sorting the random variables  $\Delta_i$  in ascending order so that each is associated to a rank  $d_i$ . The following expression of the empirical CDF can be written:

$$F_e(\Delta) = \frac{d}{N+1} \quad (17)$$

Equating Eq. (10) and Eq. (13), the parameters  $\mu, \sigma, \varepsilon$  can be obtained by regression. Hence the probability of exceeding a given vertical displacement is calculated as  $G(\Delta) = 1 - F_s(\Delta)$ . As per modern standards, the targeted annual reliability index is about  $\beta_0 = 3.3$ , which corresponds to a targeted failure probability  $Pf_0 = 4.93 \times 10^{-4}$ . This means that in order to be safe, the grouted joint should be able to undergo a vertical displacement up to  $\Delta_0 = G^{-1}(Pf_0)$  without any consequence on its structural integrity. With an allowable settlement

$h \leq \Delta_0$  (see Eq. (4)) failure is not prevented; the design should provide an allowable settlement greater than or equal to  $\Delta_0$ .

The reliability index is determined for a given design, with given material and geometry properties. In order to evaluate the survival distribution function (SDF),  $G$ , the grouted joint design with similar properties have been binned with respect to grout length, which is the primary influencing parameter. Four bins of equal width are constructed over the length range [9 m, 25 m] and the corresponding SDFs are fitted as illustrated in Figure 16. For each bin, the settlement threshold required to achieve the targeted annual reliability index is obtained by graphical projection.

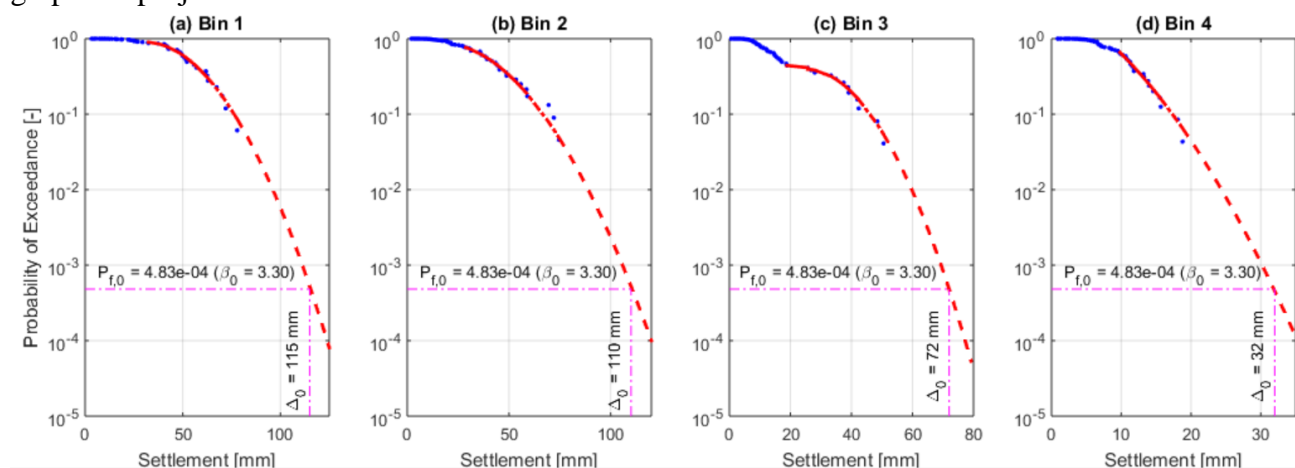


**Figure 16. Sensitivity coefficients of the structural responses with respect to the geometry and material variables. The fitted curves are in red and the data point are in blue.**

For each bin range, Table 6 gives the settlement thresholds. Thus for the reference grouted joint, which has 18 m grout length, provisions for 72 mm of vertical displacement should be made. Further, the gap between the pile top edge and the jacking brackets should be at least 72 mm to ensure that it possesses sufficient reliability. The settlement of the transition piece will then not create any consequence on the overall joint structural integrity. Within this framework of this study, allowing a settlement of 72 mm is possible as the other failure modes associated to extreme events are proven improbable. In general, if a high settlement cannot be afforded, a longer grout length should be used to achieve the required reliability.

**Table 6: Settlement thresholds for each grout length bin**

Bin No	Bin 1	Bin 2	Bin 3	Bin 4
Bin range	[9 m, 13 m)	[13 m, 17 m)	[17 m, 21 m)	[21 m, 25 m]
Settlement threshold	115 mm	110 mm	72 mm	32 mm

The major conclusions from this study are summarized in (Wandji, et al., 2018).

## 2. Reliability assessment of grouted joint with shear keys

The cylindrical grouted connection with shear keys for 10MW reference wind turbine was developed and detailed in (Santos, et al., 2017). The deterministic design and stochastic reliability analysis in the following sections are performed based on the initial design detailed in (Santos, et al., 2017), with environmental input given in *Table 2* and *Table 3*. The present report mostly focuses on further development of the stochastic concrete fatigue reliability model using (CEB-fip, 2013) as basis for the model formulation. Furthermore, an updated steel fatigue reliability model, based on fracture mechanics, is described and improvements over the simplified model from (Santos, et al., 2017) are discussed.

The cylindrical grouted joint with shear keys is initially evaluated deterministically for concrete grout fatigue resistance. The evaluation is done using two methodologies, based namely on (DNVGL-ST-C502, 2017) and (CEB-fip, 2013). Such evaluation is necessary for comparison purposes between the two methodologies and in order to identify the most critical locations in the concrete for further reliability assessment.

### 2.1 Target reliability levels

This section describes the required target reliability levels for design of structural wind turbine components, see also D7.4.1. The basis for the description is the requirements in the CDW/FDIS version of the IEC 61400-1 ed. 4 (IEC61400-1, 2017) wind turbine standard which are also described in the background document (Sørensen, 2014). The target reliability level can generally be given in terms of a maximum annual probability of failures (i.e. reference time equal to 1 year) or a maximum lifetime probability of failure (i.e. for wind turbines a reference time equal to 20 – 25 years). For civil and structural engineering standards / codes of practice where failure can imply risk of loss of human lives target reliabilities are generally given based on annual probabilities. Examples of reliability levels required (implicitly) in some relevant standards / codes (for normal consequence / reliability class) are:

- For fixed steel offshore structures, see e.g. ISO 19902 (ISO 19902, 2007) an indicated annual probability of failure for manned structures is  $P_F \sim 3 \cdot 10^{-5}$  or  $\beta = 4.0$ . For structures that are unmanned or evacuated in severe storms and where other consequences of failure are not very significant the indicated annual probability of failure  $P_F \sim 5 \cdot 10^{-4}$  or  $\beta = 3.3$ .
- (DNV-OS-J101, 2014) states: ‘The target safety level for structural design of support structures and foundations for wind turbines to the normal safety class according to this standard is a nominal annual probability of failure of  $10^{-4}$ . This target safety is the level aimed at for structures, whose failures are ductile, and which have some reserve capacity. The target safety level of  $10^{-4}$  is compatible with the safety level implied by DNV-OS-C101 for unmanned structures’. It is noted that (DNVGL-ST-0126, 2016) does not contain a target reliability level, but opens for the use of reliability-based design.
- (JCSS, 2002) and (ISO 2394, 2015) recommend reliability requirements based on annual failure probabilities for structural systems for ultimate limit states These are based on optimization procedures and on the assumption that for almost all

engineering facilities the only reasonable reconstruction policy is systematic rebuilding or repair.

It should be noted that the  $\beta$ -values (and the corresponding failure probabilities) are formal / notional numbers, intended primarily as a tool for developing consistent design rules, rather than giving a description of the structural failure frequency. E.g. the effect of human errors is not included. Human errors in design and execution are assumed to be detected by quality control.

For wind turbines the risk of loss of human lives in case of failure of a structural element is generally very small. Further, it can be assumed that wind turbines are systematically reconstructed in case of collapse or end of lifetime. In that case also target reliabilities based on annual probabilities should be used, see JCSS, (JCSS, 2002). The optimal reliability level can be found by considering representative cost-benefit based optimization problems where the life-cycle expected cost of energy is minimized. Also, the following assumptions are made in (IEC61400-1, 2017) and (Sørensen, 2014):

- A systematic reconstruction policy is used (a new wind turbine is erected in case of failure or expiry of lifetime).
- Consequences of a failure are only economic (no fatalities and no pollution).
- Cost of energy is important which implies that the relative cost of safety measures can be considered large (material cost savings are important).
- Wind turbines are designed to a certain wind turbine class, i.e. not all wind turbines are 'designed to the limit'.

Based on these considerations the target reliability level corresponding to a minimum annual probability of failure is recommended to be  $P_f = 5 \cdot 10^{-4}$  corresponding to an annual reliability index equal to 3.3. This reliability level corresponds to minor / moderate consequences of failure and moderate / high cost of safety measure.

## 2.1 Deterministic assessment of concrete grout fatigue resistance

### 2.1.1 Deterministic assessment according to DNVGL-ST-C502

(DNVGL-ST-C502, 2017) recommends the following procedure to estimate the fatigue damage within the concrete grouted connection:

$$\log_{10} N_1 = C_1 \left( \frac{1 - \frac{\sigma_{\max}}{C_5 \cdot f_{rd}}}{1 - \frac{\sigma_{\min}}{C_5 \cdot f_{rd}}} \right) \quad (18)$$

$$\log_{10} N = \log_{10} N_1 \cdot C_2 \quad \text{for} \quad \log_{10} N_1 > X \quad (19)$$

$$X = \frac{C_1}{1 - \frac{\sigma_{\min}}{C_5 \cdot f_{rd}} + 0.1 \cdot C_1} \quad (20)$$

$$C_2 = (1 + 0.2(\log_{10} N_1 - X)) > 1.0 \quad (21)$$

$$f_{rd} = \frac{f_{cn}}{\gamma_{c,fat}} \quad (22)$$

$$f_{cn} = f_{ck} \cdot \left(1 - \frac{f_{ck}}{600}\right) \quad (23)$$

$$D = \sum_{i=1}^k \frac{t_i \cdot n_i}{N_i} \leq \eta \quad (24)$$

here  $N$  is the design life in terms of number of cycles;  $\sigma_{max}$ ,  $\sigma_{min}$  are the numerically largest and smallest compressive stresses;  $f_{rd}$  is the design compressive fatigue strength of concrete;  $C_5$  is fatigue strength parameter, for grout = 0.8 in the absence of fatigue tests;  $C_1$  factor is taken = 12 for concrete structures in air, = 10 for structures in water with stress variation in compression-compression range and = 8 for stress variation in compression-tension range;  $f_{ck}$  is the characteristic compressive concrete strength;  $f_{cn}$  is normalized compressive strength of concrete;  $\gamma_{c,fat}$  is the partial safety factor for concrete in fatigue = 1.5;  $t_i$  is the service life;  $n_i$  is the expected annual number of particular stress cycles;  $\eta$  is cumulative damage ratio, = 0.33 for structures with no access for inspection.

It should be noted that following the methodology from (DNVGL-ST-C502, 2017), all tensile stress ranges are individually set to 0 and the effect of grout fatigue due to tension is only accounted for through the use of a lowered  $C_1$  factor in eq.(18). The following Figure 17 shows the resulting accumulated damage throughout the analyzed section of the cylindrical grouted connection.

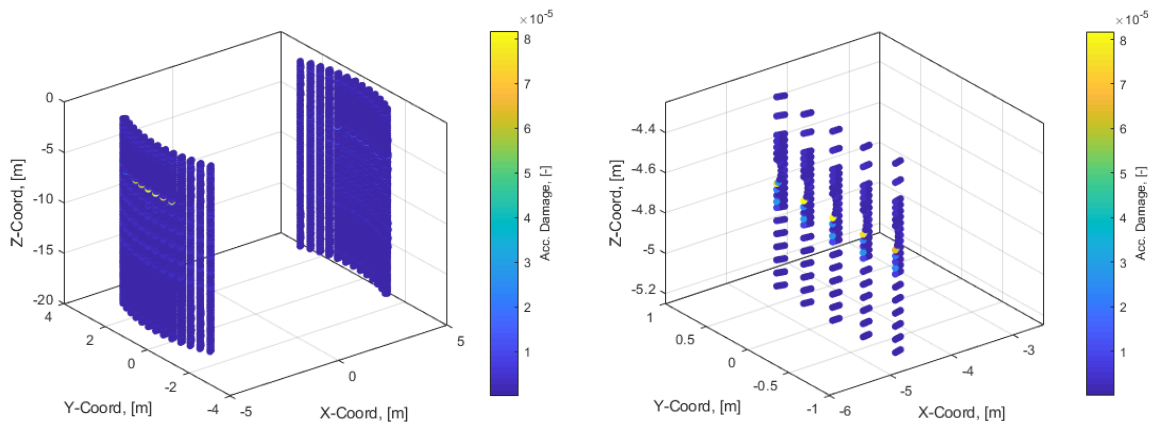


**Figure 17: Accumulated damage (left) and a zoom of most critical location (right).**

It is clear that the most critical cross-section of the grout is located just below the first level of shear keys with significantly lower fatigue damage in subsequent lower levels of shear keys. Using grout with 100MPa characteristic compressive strength the design of the connection seems sub-optimal, accumulated damage over 25-year lifetime is orders of magnitude lower than  $\eta=0.33$ , thus implying that further optimization of the design would be necessary – possibly through reduction of grout strength or changes in shear key geometry/placement. However, it is important to further evaluate the most critically loaded location in terms of expected reliability - this is done in the following sections.

### 2.1.2 Deterministic assessment according to fib Model Code 2010

(DNVGL-ST-0126, 2016) allows the use of Model Code 2010 (CEB-fip, 2013) for concrete/grout fatigue evaluation with certain modifications to the concrete fatigue strength - eq.(25-26). Furthermore, a design fatigue factor  $DFF=1$  should be used, instead of 3, giving allowable cumulative damage ratio  $\eta=1.0$  in contrast with  $\eta=0.33$  used by (DNVGL-ST-C502, 2017).

$$f_{ck,fat} = \beta_{sus} \cdot \beta_{red} \cdot \beta_{cc}(t) \cdot f_{ck} \cdot \left(1 - \frac{f_{ck}}{400}\right) \quad (25)$$

$$f_{cd,fat} = \frac{f_{ck,fat}}{\gamma_{C,fat}} \quad (26)$$

$$f_{td,fat} = \beta_{red} \cdot \beta_{cc} \cdot 2.12 \cdot \ln(1 + 0.1 f_{cm}) / \gamma_{C,fat} \quad (27)$$

Here  $\beta_{red}$  – strength reduction due to specific interaction between concrete grout and steel = 0.8;  $\beta_{sus}$  – strength reduction coefficient due to sustained load (mismatch between testing and real load frequencies) = 0.85;  $\beta_{cc}$  – coefficient for considering time dependent load (=1.0 after 28 days for this case);  $\gamma_c$  is the partial safety factor for concrete grout in fatigue =1.5.

According to (CEB-fip, 2013) the following procedure for fatigue evaluation of concrete grout should be followed:

$$D = \sum_{i=1}^n \frac{t \cdot n_i}{10^{\log N_{Ri}}} \geq \eta = 1 \quad (28)$$

$$\log N_R = \frac{8}{Y-1} \cdot (S_{cd,max} - 1) \quad \text{for } \log N \leq 8 \quad \text{compression only} \quad (29)$$

$$\log N_R = 8 + \frac{8 \cdot \ln(10)}{Y-1} \cdot (Y - S_{cs,min}) \cdot \log\left(\frac{S_{cd,max} - S_{cd,min}}{Y - S_{cd,min}}\right) \quad \text{for } \log N > 8 \quad \text{compression only} \quad (30)$$

$$\log N_R = 9 \cdot (1 - S_{cd,max}) \quad \text{for } \sigma_{ct,max} \leq 0.026 |\sigma_{c,max}| \quad \text{compression-tension} \quad (31)$$

$$\log N_R = 12 \cdot (1 - S_{td,max}) \quad \text{for } \sigma_{ct,max} > 0.026 |\sigma_{c,max}| \quad \text{compression-pure tension} \quad (32)$$

$$Y = \frac{0.45 + 1.8 \cdot S_{cd,min}}{1 + 1.8 \cdot S_{cd,min} - 0.3 \cdot S_{cd,min}^2} \quad (33)$$

$$S_{c,min} = \frac{\gamma_{Ed} \cdot C_{LOAD} \cdot |\sigma_{c,min}|}{f_{cd,fat}} \quad S_{c,max} = \frac{\gamma_{Ed} \cdot C_{LOAD} \cdot |\sigma_{c,max}|}{f_{cd,fat}} \quad S_{ct,max} = \frac{\gamma_{Ed} \cdot C_{LOAD} \cdot |\sigma_{ct,max}|}{f_{td,fat}} \quad (34)$$

Here  $t$  – service time in years;  $n_i$  – number of stress range/mean stress combinations in a given year (from Markov Matrix);  $S_{cd,min}$ ,  $S_{cd,max}$  – normalized design minimum and maximum compressive stress levels, respectively;  $\sigma_{c,min}$ ,  $\sigma_{c,max}$  – minimum and maximum compressive stresses in MPa;  $\sigma_{ct,max}$  – maximum tensile stress in MPa;  $\gamma_{Ed}$  – partial safety factor for fatigue loading =1.1, according to (CEB-fip, 2013).

A significant difference between (CEB-fip, 2013) and (DNVGL-ST-C502, 2017) methodologies for concrete fatigue assessment is that (CEB-fip, 2013), instead of setting tensile stresses to 0 (together with proposing a more conservative SN curve), proposes SN curves (eq.(31-32)) for concrete in compression-tension and compression-pure tension fatigue loading. For comparison purposes between (CEB-fip, 2013) and (DNVGL-ST-C502, 2017), initially only compression-compression loading is considered and only eq.(29-30) are used. The following Figure 18 shows the resulting accumulated damage of the grouted connection.

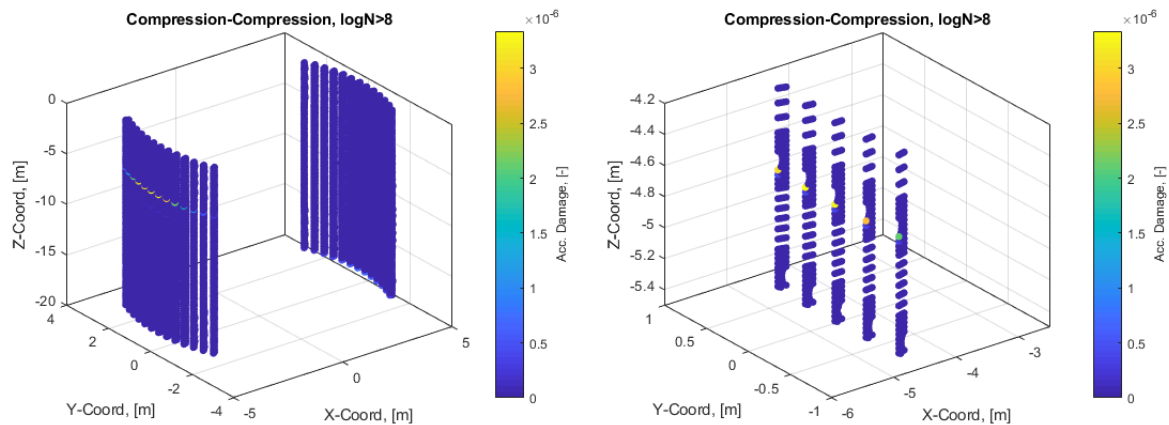


**Figure 18: Accumulated damage (left) and a zoom of most critical location (right), Compression - Compression SN curve (CEB-fip, 2013).**

While the location of the most critically loaded concrete nodes remains the same (upper-most level of shear keys with decreasing accumulated damage for lower shear key levels), (CEB-fip, 2013) gives lower accumulated damage results. The design still seems sub-optimal using concrete with 100MPa compressive strength - accumulated damage is orders of magnitude lower than  $\eta=1.0$ . It should also be noted that due to magnitude of stresses in the concrete, the joint operates in  $\log N > 8$  region thus eq.(30) contributes most to the damage accumulation. Further, compression-tension and compression-pure tension fatigue loading is included in the accumulated damage calculation. Figure 19 below shows the resulting accumulated damage of compression-tension stress components.

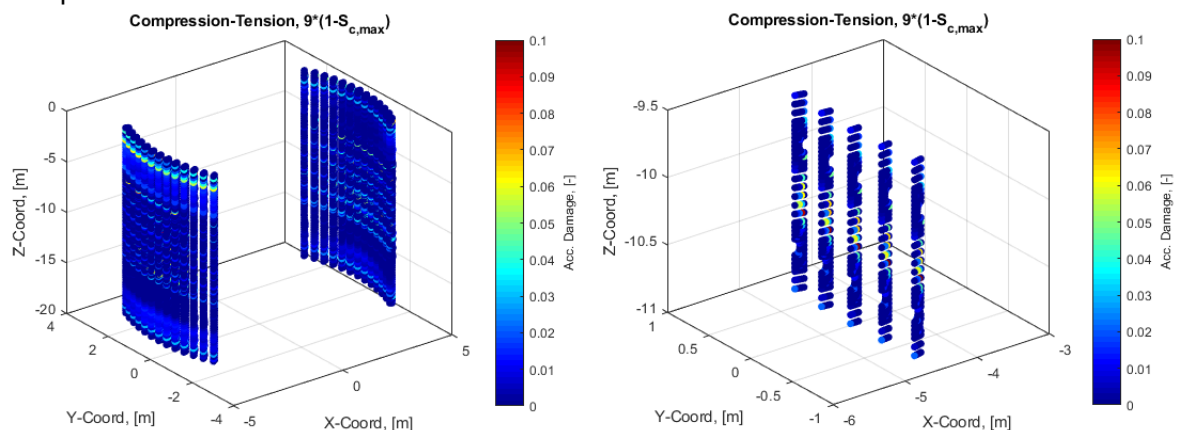


**Figure 19: Accumulated damage (left) and a zoom of most critical location (right), Compression - Tension SN curve (CEB-fip, 2013).**

Most critical nodes when compression-tension stress components are included in the analysis appears to be roughly in the middle of the grouted joint ( $z = -10.43\text{m}$ ), in between shear keys on the opposing sides of the concrete grout. It is also clear that the accumulated damage due to tensile fatigue stresses is significantly higher, while still being acceptably below  $\eta=1.0$ , than in the case where only compressive stresses were considered. This implies that a thorough tensile fatigue analysis is necessary when designing cylindrical grouted connections with shear keys. Figure 20 shows the accumulated damage of compression-pure tension stress components.

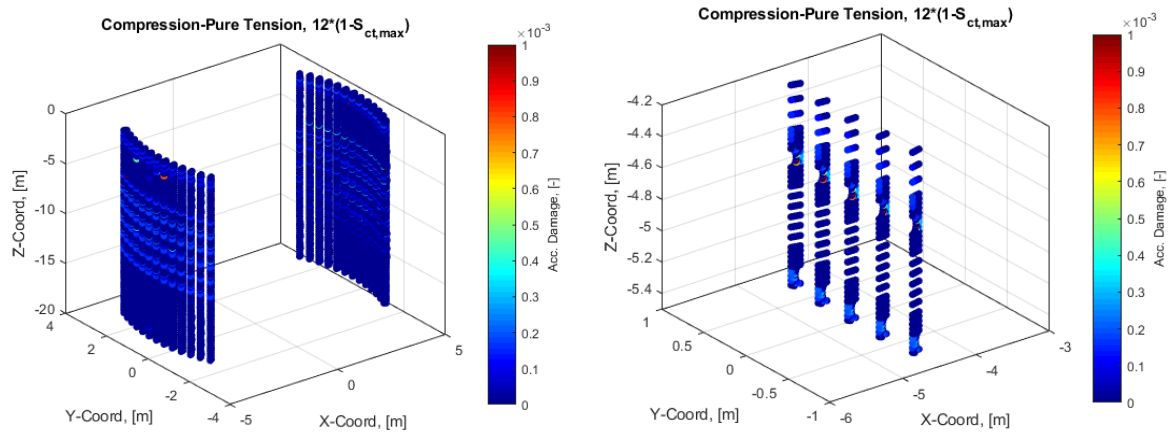


**Figure 20: Accumulated damage (left) and a zoom of most critical location (right). Compression – Pure Tension SN curve (CEB-fip, 2013).**

It is seen from the figure above that there are significant tensile regions around shear keys where compression-pure tensions stress states produce notable, while lower than compression-tension stress states, contributions to accumulated damage. This again implies that it is important not to disregard tensile fatigue stresses when assessing grouted connection fatigue resistance/life.

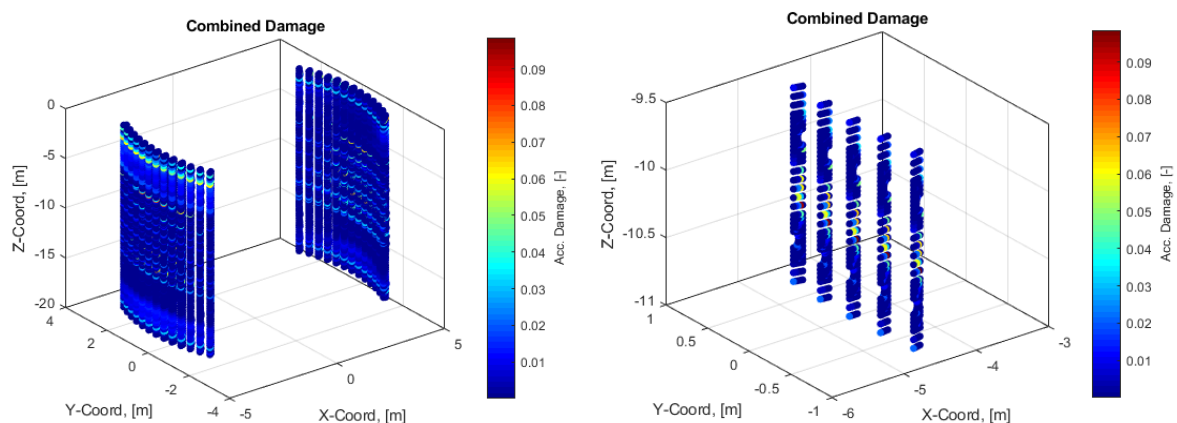


**Figure 21: Accumulated damage (left) and a zoom of most critical location (right). Combined loading.**

As the largest contribution to accumulated damage is coming from compression-tension stress ranges/states, results in Figure 21 are quite similar to Figure 20. The most critical nodes are selected from results in Figure 21 and used in further sections for concrete fatigue reliability evaluation.

## 2.2 Reliability assessment of grouted joint – Concrete grout fatigue

Fatigue reliability is assessed using SN curves proposed in (CEB-fip, 2013), modified to accommodate stochastic parameters, together with Miner's rule for damage accumulation. The limit state equation is defined by the following equations:

$$g(X, t) = D_{cr} - D(t) \geq 0 \quad (35)$$

$$g = \Delta - \sum_{i=1}^n \frac{t N_i}{10^{\log N_{Ri}}} \geq 0 \quad (36)$$

$$\log N_R = \frac{A_1}{Y-1} \cdot (S_{c,max} - 1) + \varepsilon_1 \quad \text{for } \log N \leq (A_1 + \varepsilon_1) \quad (37)$$

$$\log N_R = A_1 + \frac{A_1 \cdot \ln(10)}{Y-1} \cdot (Y - S_{c,min}) \cdot \log \left( \frac{S_{c,max} - S_{c,min}}{Y - S_{c,min}} \right) + \varepsilon_1 \quad \text{for } \log N > (A_1 + \varepsilon_1) \quad (38)$$

$$\log N_R = A_2 \cdot (1 - S_{c,max}) + \varepsilon_2 \quad \text{for } \sigma_{ct,max} \leq 0.026 |\sigma_{c,max}| \quad (39)$$

$$\log N_R = A_3 \cdot (1 - S_{ct,max}) + \varepsilon_3 \quad \text{for } \sigma_{ct,max} > 0.026 |\sigma_{c,max}| \quad (40)$$

$$Y = \frac{0.45 + 1.8 \cdot S_{c,min}}{1 + 1.8 \cdot S_{c,min} - 0.3 \cdot S_{c,min}^2} \quad (41)$$

$$S_{c,min} = \frac{C_{LOAD} |\sigma_{c,min}|}{f_{c,fat}} \quad S_{c,max} = \frac{C_{LOAD} |\sigma_{c,max}|}{f_{c,fat}} \quad S_{ct,max} = \frac{C_{LOAD} |\sigma_{ct,max}|}{f_{tm}} \quad (42)$$

$$f_{c,fat} = \beta_{red} \beta_{sus} \beta_{cc} f_{cm} (1 - f_{cm} / 400) \quad (43)$$

$$f_{t,fat} = \beta_{red} \cdot \beta_{cc} \cdot 2.12 \cdot \ln(1 + 0.1 f_{cm}) \quad (44)$$

$t$  – service time in years;  $N_i$  – number of stress range/mean stress combinations in a given year (from Markov Matrix);  $S_{c,min}$ ,  $S_{c,max}$  – normalized minimum and maximum compressive stress levels, respectively;  $\sigma_{c,min}$ ,  $\sigma_{c,max}$  – minimum and maximum compressive stresses in MPa;  $f_{c,fat}$  – compressive concrete fatigue strength in MPa;  $f_{cm}$  – mean compressive concrete strength in MPa;  $\beta_{red}$  – strength reduction due to specific interaction between concrete grout and steel;  $\beta_{sus}$  – strength reduction coefficient due to sustained load (mismatch between testing and real load frequencies);  $\beta_{cc}$  – coefficient for considering time dependent load (=1.0 after 28 days for this case).

### 2.2.1 Stochastic model for concrete grout fatigue

Stochastic model parameters for SN curves are estimated from data available in the literature, namely the compression-compression SN curve parameters ( $A_1$  and  $\varepsilon_1$ ) are estimated from (Lantsoght, 2014) and (Slot & Andersen, 2014) as detailed in (Santos, et al., 2017) and (Rodriguez, et al., 2018), whereas SN curve parameters for compression-tension and compression-pure tension ( $A_1$ ,  $A_2$ ,  $\varepsilon_1$  and  $\varepsilon_2$ ) are estimated from (Cornelissen, 1984). The statistical parameters ( $A_k$  and  $\sigma_{\varepsilon k}$ ) are estimated using the Maximum Likelihood Method for data sets available of ( $N_i$ ,  $S_{c,max,i}$ ). The likelihood function for compression-tension and compression- pure tension is in general written:

$$L(A_k, \sigma_{\varepsilon i}) = \prod_{i=1}^{n_F} P \left[ A_k \cdot (1 - S_{c(t),max,i}) + \varepsilon_k = \log N_i \right] \times \prod_{i=1}^{n_R} P \left[ A_k \cdot (1 - S_{c(t),max,i}) + \varepsilon_k > \log N_i \right] \quad (45)$$

where  $n_F$  is the number of tests where failure occurs, and  $n_R$  is the number of tests where failure did not occur (run-outs). The total number of tests is  $n = n_F + n_R$ .  $A_i$  and  $\sigma_{\varepsilon k}$  are obtained from the optimization problem

$$\max_{A_k, \sigma_{\varepsilon k}} L(A_k, \sigma_{\varepsilon k}) \quad (46)$$

or using the log-likelihood function

$$\max_{A_k, \sigma_{\varepsilon k}} \ln L(A_k, \sigma_{\varepsilon k}) \quad (47)$$

which can be solved using a standard nonlinear optimizer (e.g. NLPQL algorithm, see (Schittkowski, 1986)). Because the parameters  $A_k$ , and  $\sigma_{\varepsilon k}$  are determined using a limited amount of data; they are subject to statistical uncertainty. Since the parameters are estimated by the maximum-likelihood method, they become asymptotically (number of data should be  $> 25 - 30$ ) normally distributed stochastic variables with expected values equal to the maximum-likelihood estimators and covariance matrix equal to, see e.g. (Lindley, 1976).

$$C_{A_k, \sigma_{\varepsilon k}} = \left[ -H_{A_k, \sigma_{\varepsilon k}} \right]^{-1} = \begin{bmatrix} \sigma_{A_k}^2 & \rho_{A_k, \sigma_{\varepsilon k}} \sigma_{A_k} \sigma_{\sigma_{\varepsilon k}} \\ \rho_{A_k, \sigma_{\varepsilon k}} \sigma_{A_k} \sigma_{\sigma_{\varepsilon k}} & \sigma_{\sigma_{\varepsilon k}}^2 \end{bmatrix} \quad (48)$$

$H_{A_k, \sigma_{\varepsilon k}}$  is the Hessian matrix with second-order derivatives of the log-likelihood function.  $\sigma_{A_k}$  and  $\sigma_{\sigma_{\varepsilon k}}$  denote the standard deviations of  $A_k$  and  $\sigma_{\varepsilon k}$ , respectively, and  $\rho_{A_k, \sigma_{\varepsilon k}}$  is the correlation coefficient between  $A_k$  and  $\sigma_{\varepsilon k}$ . Table 7 shows a summary of the estimated SN curve parameters together with other parameters necessary to fully define the stochastic model for concrete fatigue reliability assessment. Furthermore, Figure 22 shows the stochastic SN curves based on equations from (CEB-fip, 2013) and stochastic parameters from Table 7.

**Table 7: Parameters for probabilistic concrete fatigue damage model.**

Variable	Distribution	Expected value	Standard deviation / COV	Comment
<b>Compression-Compression</b>				
$A_1$	N	8.91	SD=0.16	SN curve parameter
$\varepsilon_1$	N	0	SD=1.17	Model error
<b>Compression-Tension</b>				
$A_2$	N	8.64	SD=0.37	SN curve parameter
$\varepsilon_2$	N	0	SD=0.66	Model error
<b>Compression-Pure Tension</b>				
$A_3$	N	19.11	SD=1.28	SN curve parameter
$\varepsilon_3$	N	0	SD=0.80	Model error
<b>Common parameters</b>				
$f_{cm}$	LN	123	COV= 0.12	Mean concrete comp. str.
<b>Model uncertainties</b>				
$\Delta$	LN	1	COV = 0.30	Model uncertainty Miner's rule
$C_{LOAD}$	LN	1	COV= 0.08	Model uncertainty fatigue load

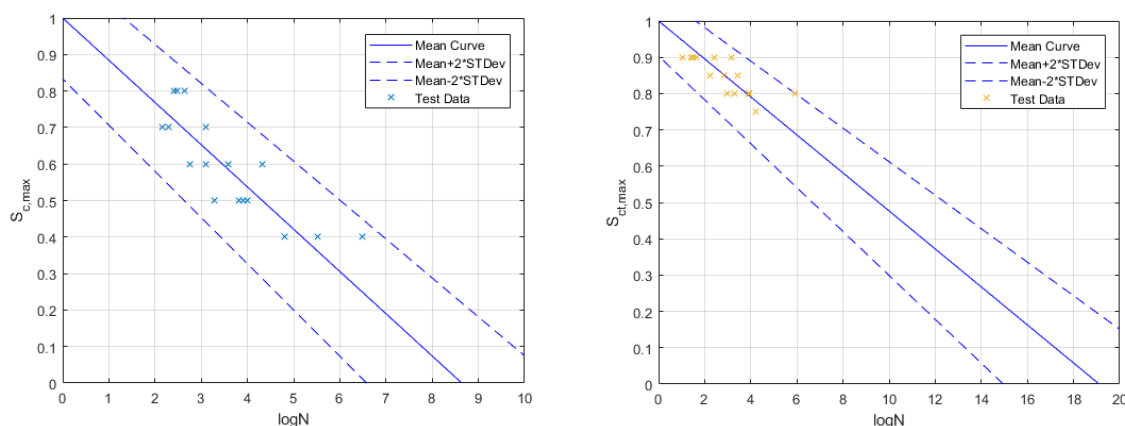


Figure 22. SN curves from (CEB-fip, 2013) using stochastic parameters from Table 7. Compression-Tension (right), Compression- Pure Tension (left). Compression-compression SN curve parameter estimation is detailed in (Santos, et al., 2017).

### 2.2.2 Results of concrete grout reliability analysis

As it was for the deterministic case, the initial reliability analysis is performed tanking only compression-compression stress ranges into consideration. Figure 23 shows the resulting accumulated and annual reliability indexes for the most critical node in compression-compression loading.

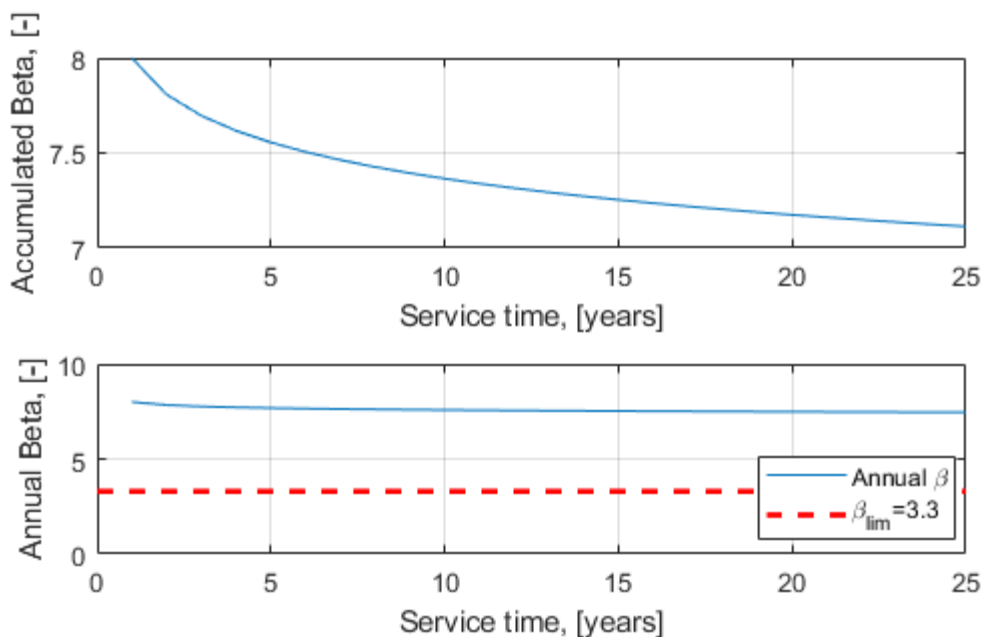


Figure 23. Accumulated and annual reliability indexes, most critical compression-compression node (node No #21250).

The annual reliability level is satisfactory with significant margin – annual reliability index is  $\beta_{ann}=7,45$  at 25<sup>th</sup> year of service and is significantly higher than the required  $\beta_{lim}=3.3$ . Figure 24 shows the relative influence of model parameters related to compression-compression case (eq.(37-38)).

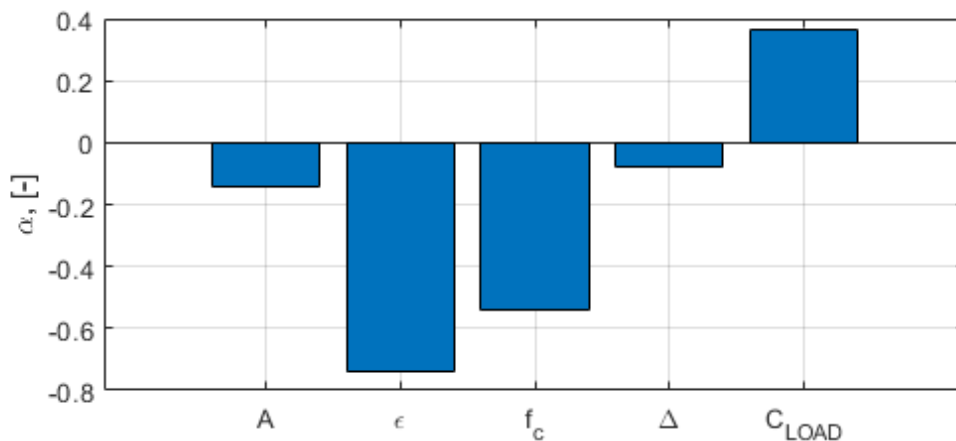


Figure 24. Compression-Compression model sensitivities.

It can be concluded that the most influential parameter is the model error  $\epsilon$ , indicating that having more fatigue test data for SN curve parameter estimation would be very beneficial towards increasing the fatigue reliability of concrete grout, see also Figure 25 for more details. Also, reduction in concrete compressive strength variability would also benefit the annual reliability estimates, since concrete compressive strength is the second most influential parameter.

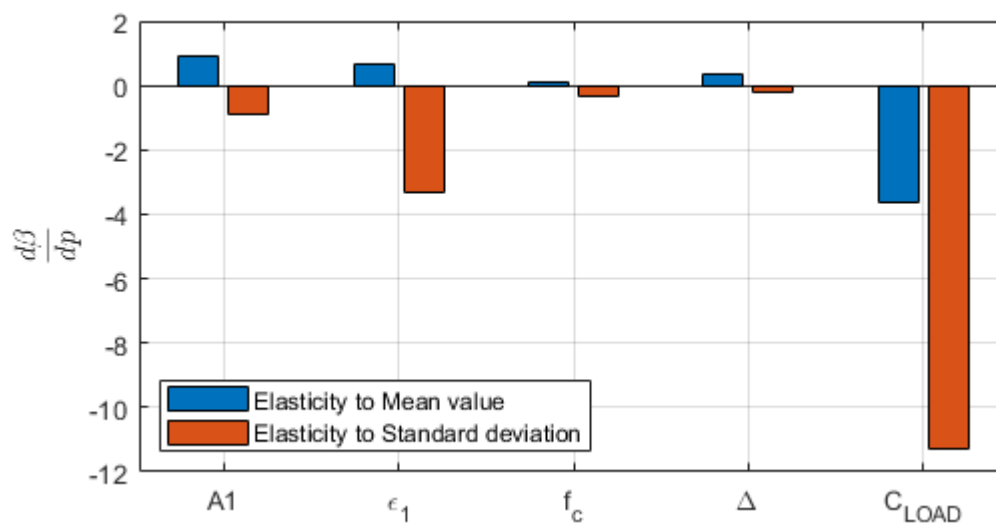


Figure 25. Compression-Compression model reliability elasticity coefficients.

When a stochastic model is extended to include compression-tension (pure tension) stress states, the annual reliability level decreases significantly but still remains satisfactory (above  $\beta_{lim}=3.3$ ), see Figure 26.

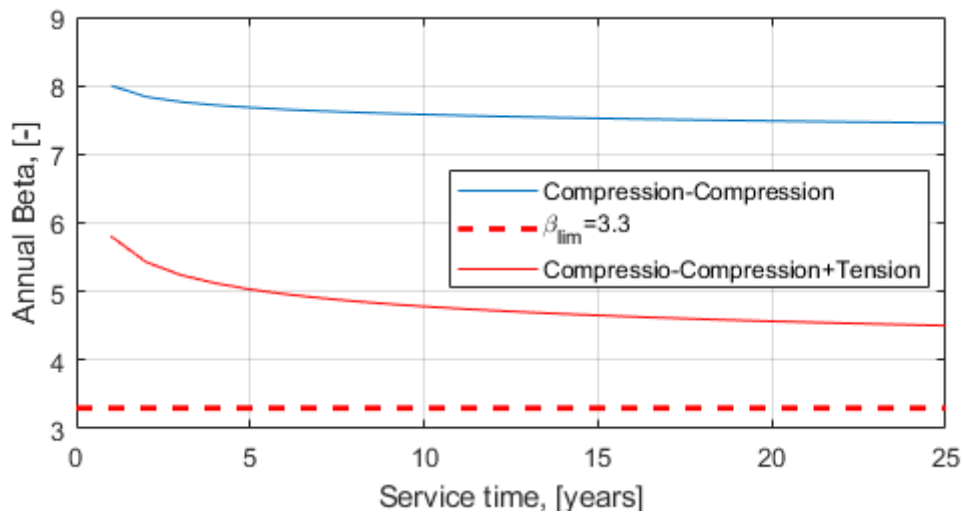


Figure 26. Effect of stochastic model extension to include tension stress states, (node No #21250).

Looking at extended model sensitivities in Figure 27, it is seen that the most influential parameters are  $A_2$  and  $\epsilon_2$  indicating that vast majority of accumulated damage (and reduction of annual reliability index) stems from compression-tension stress states, this also corresponds to the findings of deterministic analysis according to Model Code 2010 (see Figure 19) implying consistency between proposed deterministic and probabilistic models.

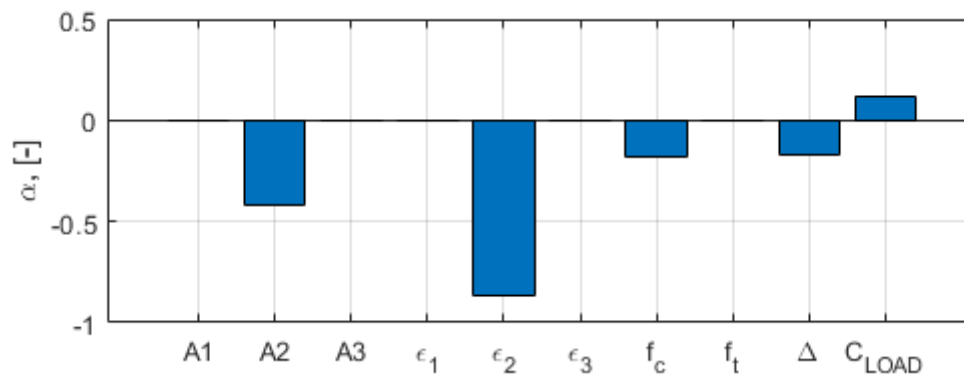
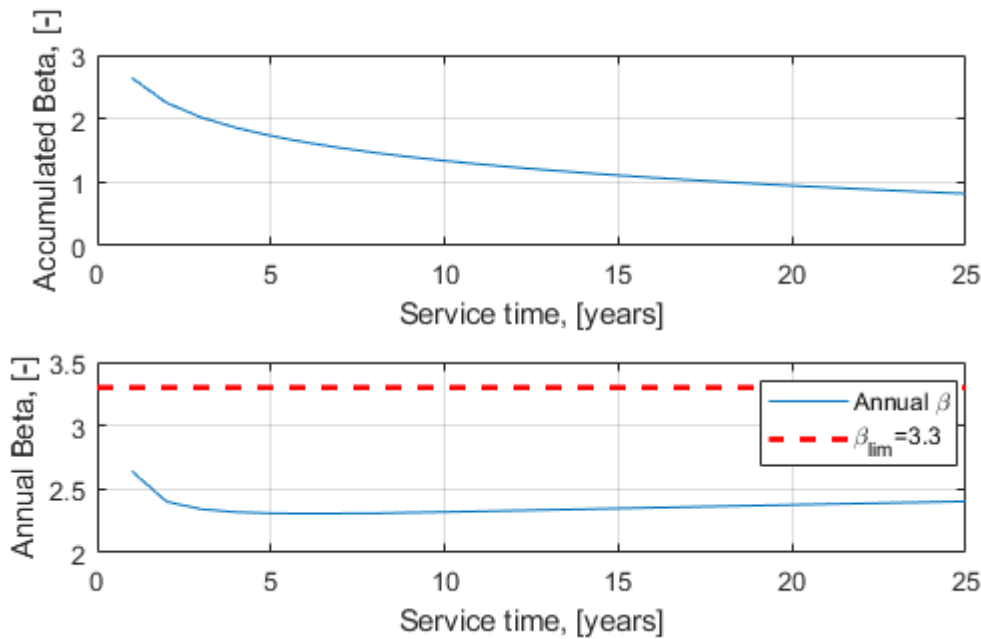


Figure 27. Sensitivities of the extended stochastic model.

Relative absence of  $A_1$ ,  $A_3$ ,  $\epsilon_1$  and  $\epsilon_3$  parameter influence also supports the premise that most of the accumulated damage comes from compression-tension stress states. Here it should also be noted that having more fatigue test data to estimate compression-tension SN curve parameters would be beneficial towards increasing reliability levels of concrete grout due to very high relative importance of model error  $\epsilon_2$ .

Deterministic evaluation of the grouted joint revealed that locations of the most critical nodes loaded in compression-compression and compression-tension are not identical, see Figure 18 and Figure 19. Thus, it is important to estimate the expected annual reliability level for the most critical node loaded in compression-tension, see Figure 29.



**Figure 28. Accumulated and annual reliability indexes, most critical compression-compression node (node No #37845).**

It is evident that the annual reliability level requirement is not satisfied throughout the lifetime of the structure ( $\beta_{ann} < \beta_{lim}=3.3$ ). It should be noted that  $\beta_{lim}=3.3$  requirement implies immediate collapse of the structure when  $\beta_{ann} < \beta_{lim}$ . However, it could be argued that local failure of concrete grout would not result in sudden failure of the structure – due to redundancy implying load transfer to other locations / shear keys and eventually by condition monitoring it would be possible to detect such local failure before it causes irreversible damage to the wind turbine structure and/or commence repairs. As it was mentioned above, reducing model errors ( $\epsilon_k$ ) related to Model Code SN curves could benefit reliability levels of the grouted connection. Figure 29 shows the effect of reduced variance of model errors towards annual reliability levels of the most critical node in the grouted connection. An increase in annual reliability in the early years of service life can be expected, however at the end of service life only very limited benefits are observed (curves converge to  $\beta_{ann} \sim 2.5$ ). This reliability level can be considered acceptable due to the above effects related to redundancy and condition monitoring / inspections implying damage tolerance, see also (Sørensen & Toft, 2014) and (IEC 61400-1, 2017).

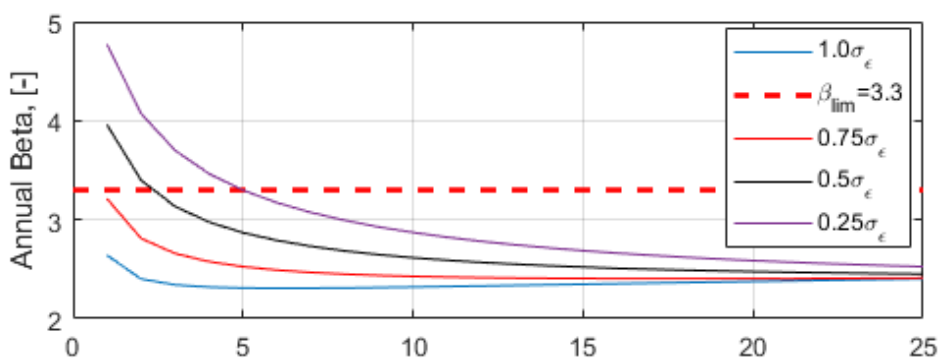


**Figure 29. Effect of different model error standard deviations ( $\sigma_{\epsilon k}$ ), model from Table 7.**

Additionally, Figure 30 and Figure 31 below show the reliability elasticity coefficients related to cases shown in in Figure 29.

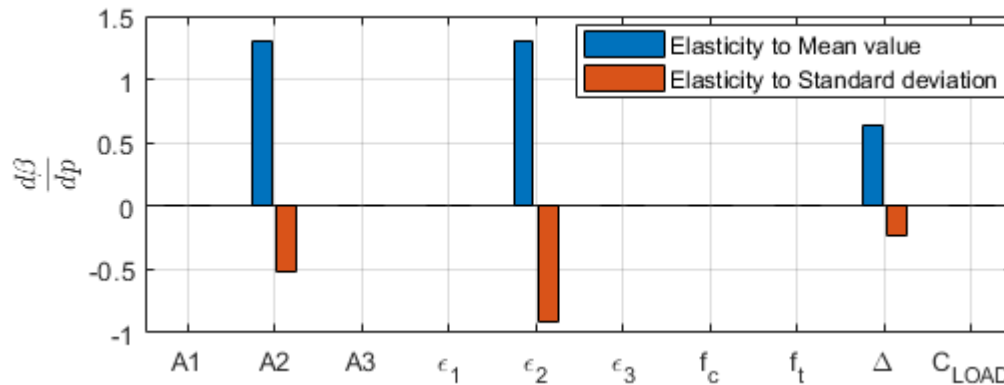


Figure 30. Reliability elasticity coefficients for 1.0  $\sigma_\epsilon$  case in Figure 29.

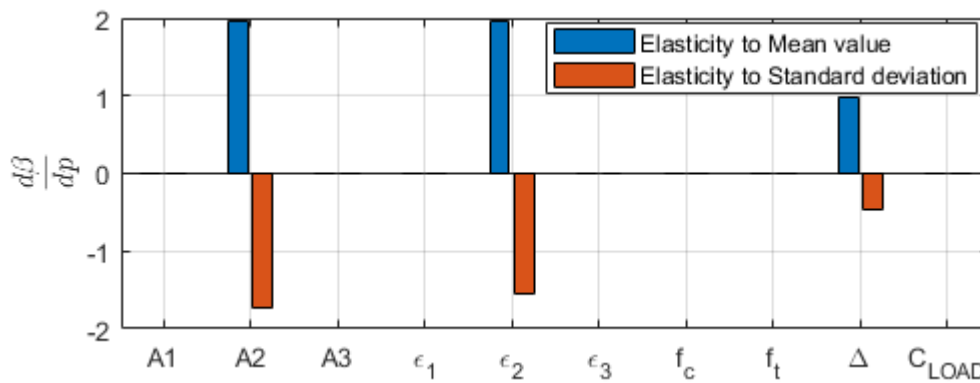


Figure 31. Reliability elasticity coefficients for 0.5  $\sigma_\epsilon$  case in Figure 29.

It is clear that reliability indexes are quite sensitive to changes in mean values and standard deviations of model parameters. Obviously increasing the intercept of SN curve and X axis (mean value of parameter  $A_2$ ) or total allowable accumulated damage (mean value of parameter  $\Delta$ ) would increase the reliability index, as would also an increase in mean value of the model error  $\epsilon_2$ , as is evident from positive mean value elasticity coefficients. Conversely, increase of standard deviation of any of these stochastic variables would result in significant reduction of grouted joint reliability indexes.

### 2.3 Reliability assessment of grouted joint – fatigue of welded steel details

A deterministic analysis of the steel part of the grouted connection is performed and detailed in (Santos, et al., 2017). (Santos, et al., 2017) also contains the initial reliability assessment of the steel components of the grouted connection – a simplified fracture mechanics based steel fatigue model is calibrated to give the same (or as close as possible) annual reliability levels throughout the lifetime. In the following section a more advanced fracture mechanics model is used to investigate whether such more complex model would be beneficial. This section uses SN curve based probabilistic model results as basis to calibrate the updated fracture mechanics based fatigue crack growth model.

#### 2.3.1 Stochastic model for steel fatigue

The fatigue crack growth model (based on fracture mechanics) is bi-linear and crack growth is considered in both ‘c’ and ‘a’ (depth and width) directions, see Figure 32, right side. The model is generally based on (JCSS , 2012) with crack growth parameters adopted from (BS 7910, 2013) where necessary. The crack growth is typically described by the following coupled differential equations:

$$\frac{da}{dN} = A_a (\Delta K_a)^m \quad a(N_0) = a_0 \quad (49)$$

$$\frac{dc}{dN} = A_c (\Delta K_c)^m \quad c(N_0) = c_0 \quad (50)$$

here  $A_a$ ,  $A_c$  and  $m$  are material parameters,  $a_0$  and  $c_0$  describe the crack depth  $a$  and crack length  $c$ , respectively, after  $N_1$  cycles and where the stress intensity ranges are  $\Delta K_a(\Delta\sigma)$  and  $\Delta K_c(\Delta\sigma)$ .

Failure is considered when a crack grows through the thickness of the monopile/transition piece steel and can be summarized in the following limit state function:

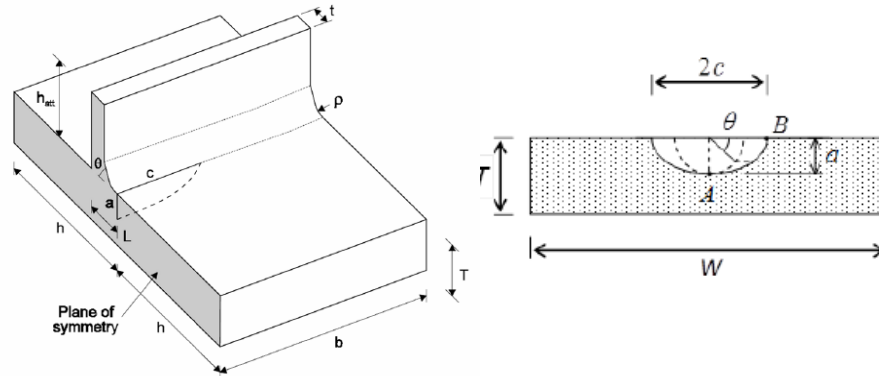


**Figure 32: Weld geometry parameters for crack growth model, [64].**

$$g(X, t) = a_{cr} - a(t) \geq 0 \quad (51)$$

where  $t$  is time (in years) in the time interval between 0 and service life  $T_L$ . Crack dimensions at any given time within turbines service life can be calculated using following equations:

$$a(t) = \sum_{i,1} N_{i,1} A_1 (C_{SIF} \Delta K_{a,i,1})^{m_1} + \sum_{j,2} N_{j,2} A_2 (C_{SIF} \Delta K_{a,j,2})^{m_2} \quad (52)$$

$$c(t) = \sum_{i,1} N_{i,1} A_1 (C_{SIF} \Delta K_{c,i,1})^{m_1} + \sum_{j,2} N_{j,2} A_2 (C_{SIF} \Delta K_{c,j,2})^{m_2} \quad (53)$$

Equations (52) and (53) are a discretized version of (49) and (50), representing crack growth in two directions (depth ‘a’ and width ‘c’), hence the summations. Also, use of sets of two A and K parameters comes from the use of bi-linear crack growth model ( $A_1, K_1$  for Stage A and  $A_2, K_2$  for Stage B in Figure 2.33). Here the model differs from the one presented in (Santos, et al., 2017) –  $\alpha$  coefficient is added to take into account the fact that different loading conditions (bending and membrane stresses) cause different crack growth behaviour.

$$\Delta K_{i,a} = (M_{kma} M_{ma} \alpha + M_{kba} M_{ba} (1-\alpha)) C_{Load} C_{SCF} \Delta \sigma_i \sqrt{\pi a_i} \quad (54)$$

$$\Delta K_{i,c} = (M_{kmc} M_{mc} \alpha + M_{kbc} M_{bc} (1-\alpha)) C_{Load} C_{SCF} \Delta \sigma_i \sqrt{\pi a_i} \quad (55)$$

$$M_{km(b)a} = f_1\left(\frac{a}{T}, \frac{a}{c}\right) + f_2\left(\frac{a}{T}, \theta\right) + f_3\left(\frac{a}{T}, \theta, \frac{L}{T}\right) \quad (56)$$

$$M_{km(b)c} = f_1\left(\frac{a}{T}, \frac{c}{a}, \frac{L}{T}\right) f_2\left(\frac{a}{T}, \frac{a}{c}, \theta\right) f_3\left(\frac{a}{T}, \frac{a}{c}, \theta, \frac{L}{T}\right) \quad (57)$$

$$M_{ma(c)} = \left[ M_1 + M_2 \left(\frac{a}{c}\right)^2 + M_3 \left(\frac{a}{c}\right)^4 \right] g \cdot f_{\theta} / \Phi \quad (58)$$

$$M_{ba(c)} = M_{ma(c)} \cdot H \quad (59)$$

$$H = H_1 + (H_2 - H_1) \sin^q(\theta) \quad (60)$$

$$\alpha = \frac{\sigma_{membrane}}{\sigma_{total}} \quad (61)$$

Here  $N_i$  is number of stress ranges  $\Delta \sigma_i$  within considered lifetime window;  $A_1$ ,  $A_2$ ,  $m_1$  and  $m_2$  are material parameters based on crack growth environment for bi-linear crack growth curves;  $C_{SIF}$  is model uncertainty related to stress intensity magnification factors ( $M_{km(b)a(c)}$  and  $M_{m(b)a(c)}$ );  $C_{LOAD}$  models uncertainty related to load (stress) modelling and  $C_{SCF}$  models uncertainty related to stress concentration factor calculation;  $\alpha$  is membrane ( $\sigma_m$ ) to total ( $\sigma_{tot}$ ) stress ratio.

Stress intensity magnification factors based on weld and crack geometry (Figure 32) are calculated based on (DNV GL, 2015), (BS 7910, 2013) and (BOWNESS & M.M.K., 2002) using  $f_1$ ,  $f_2$ ,  $f_3$ ,  $M_1$ ,  $M_2$ ,  $g$ ,  $f_{\theta}$  geometrical coefficients.  $\theta$  is weld angle in on the left and  $\Theta$  is the crack growth direction angle in 68 on the right (90 for growth in depth direction “a” and 0 for growth in width direction “c”). It should be noted here that membrane and bending loading was considered for the tubular joints, and the interaction between these two types of loading is represented by  $\alpha$  coefficient, as recommended by (DNV GL, 2015) section 6.7. The following Table 8 summarizes all the parameters used for this analysis.

**Table 8: Parameters for Crack growth (Fracture mechanics) probabilistic model**

Variable	Distribution	Expected value	Standard deviation / COV	Comment
$a_0$	LN	Fitted to match SN results	COV= 0.66	Initial crack depth
$c_0$	LN	$a_0/0.62$	COV= 0.40	Initial crack width
$a_{cr}$	D	80 mm (97 mm)	-	Critical crack depth, thickness of the steel.
<b>In marine environment with Cathodic protection at -850mV (Ag/AgCl)</b>				
$\log(A_1)$	N	-17.32	SD= 0.32	FM curve parameter
$\log(A_2)$	N	-11.22	SD= 0.264	FM curve parameter
$m_1$	D	5.1	-	Slope FM curve
$m_2$	D	2.67	-	Slope FM curve

<b>In marine environment with Cathodic protection at -1100mV (Ag/AgCl)</b>				
log(A <sub>1</sub> )	N	-17.32	SD= 0.32	FM curve parameter
log(A <sub>2</sub> )	N	-11.28	SD= 0.144	FM curve parameter
m <sub>1</sub>	D	5.1	-	Slope FM curve
m <sub>2</sub>	D	2.67	-	Slope FM curve
<b>In Air</b>				
log(A <sub>1</sub> )	N	-17.32	SD= 0.32	FM curve parameter
log(A <sub>2</sub> )	N	-12.23	SD= 0.171	FM curve parameter
m <sub>1</sub>	D	5.1	-	Slope FM curve
m <sub>2</sub>	D	2.88	-	Slope FM curve
<b>Model uncertainties</b>				
C <sub>LOAD</sub>	LN	1	COV= 0.22 (0.17)	Global stress analysis/load uncertainty
C <sub>SCF</sub>	LN	1	COV= 0.1 (0.05)	Stress concentration
C <sub>SIF</sub>	LN	1	COV= 0.07	Stress intensity factors
Bracketed values are for monopile nodes (if different from transition piece), e.g. (97mm steel thickness for monopile).				

General procedure of crack growth modelling using differential equations given in the beginning of this section is summarized in Figure 34. The transition (“knee”) point between stages A and B in Figure 34 is calculated based on realizations of log(A<sub>1</sub>), log(A<sub>2</sub>), m<sub>1</sub> and m<sub>2</sub> using the following equation:

$$\log(\Delta K_{trans}) = \frac{\log(A_1) - \log(A_2)}{m_2 - m_1} \quad (62)$$

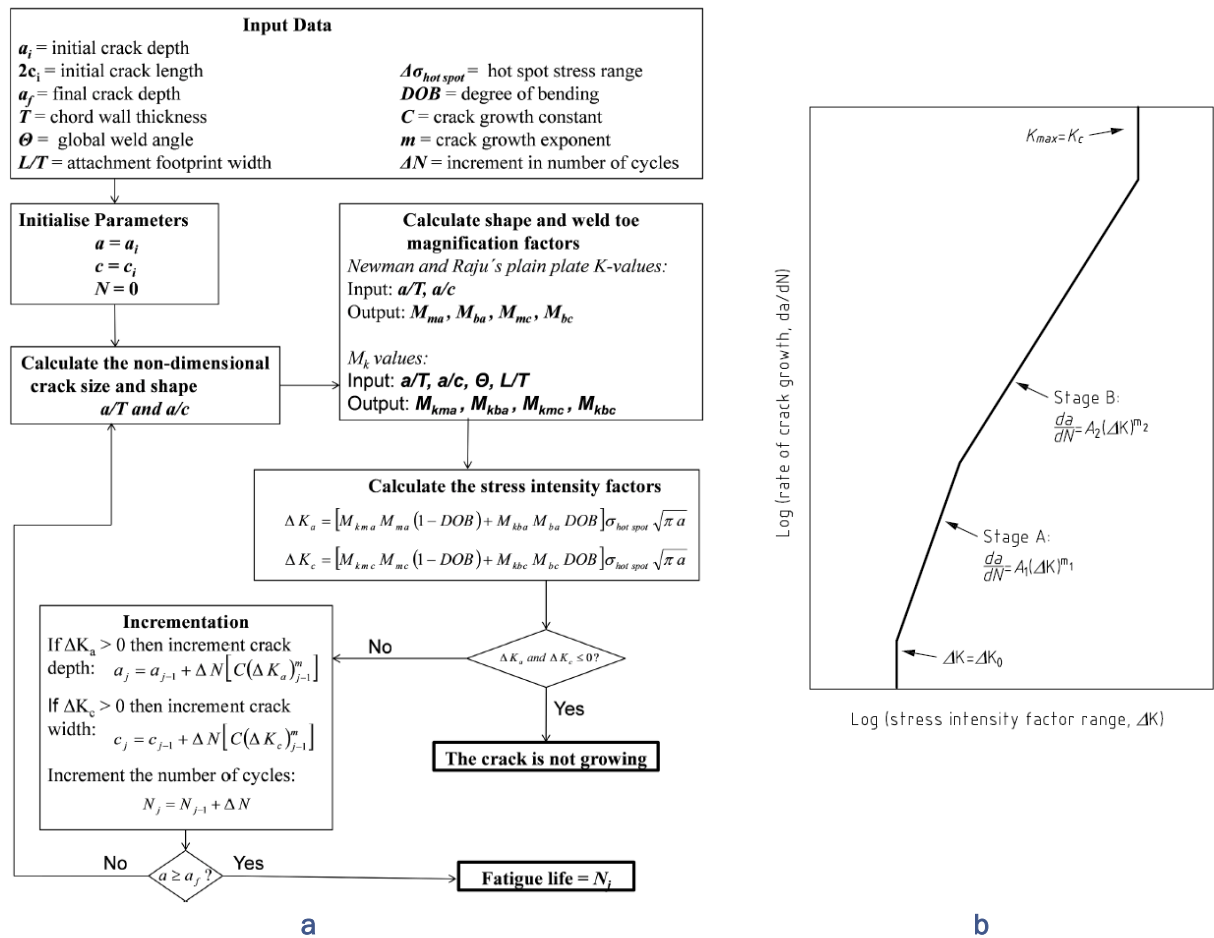


Figure 34.: Procedure for crack growth calculation (a) (DNV GL, 2015) and Paris law sketch (b) (JCSS, 2012)

As recommended in (DNV GL, 2015) the following additional geometrical parameters for monopile and transition piece are used:

$$L_{TPweld} = 1.5 \cdot T_{shearkey} = 1.5 \cdot 60 = 90mm$$

$$\theta_{TPweld} = 45^0$$

$$L_{PILEweld} = 0.5 \cdot T_{TP} = 0.5 \cdot 97 = 48.5mm$$

$$\theta_{PILEweld} = 15^0$$

$$L_{Weld} = 1.17 \cdot T_{TP}$$

$$\alpha = 0.12$$

### 2.3.2 Results steel fatigue reliability analysis

The following Figure 35 shows the results using calibrated fracture mechanics based model, as mentioned in Table 8, the calibration parameter is initial crack depth  $a_0$ .

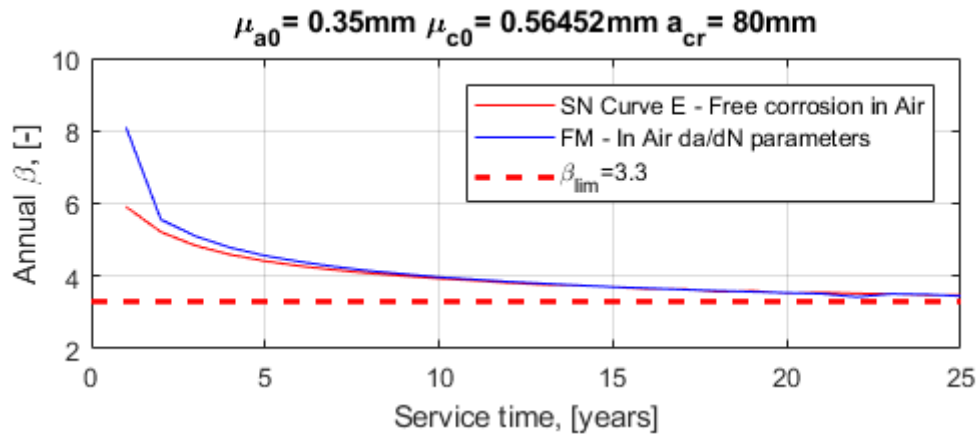


**Figure 35: Results of FM model calibration for most critical Transition Piece node.**

Similarly good match between SN and FM models can be observed, as it was when using a simplified FM model in (Santos, et al., 2017), thus it can be stated that models are compatible among each other. It should be noted that taking into consideration the difference in crack growth due to membrane and bending loading through the  $\alpha$  coefficient allows for bigger initial crack depths – identical case in (Santos, et al., 2017) allows for  $\sim 0.02\text{mm}$  initial crack sized, conversely the present model allows for  $0.35\text{mm}$  average initial crack depths. Such increase would be beneficial during manufacturing, where less strict quality requirements would need to be implemented, ultimately resulting in possible lowering of cost of production. Figure 36 shows sensitivity measures of the FM model, when considering transition piece nodes (In Air environment).

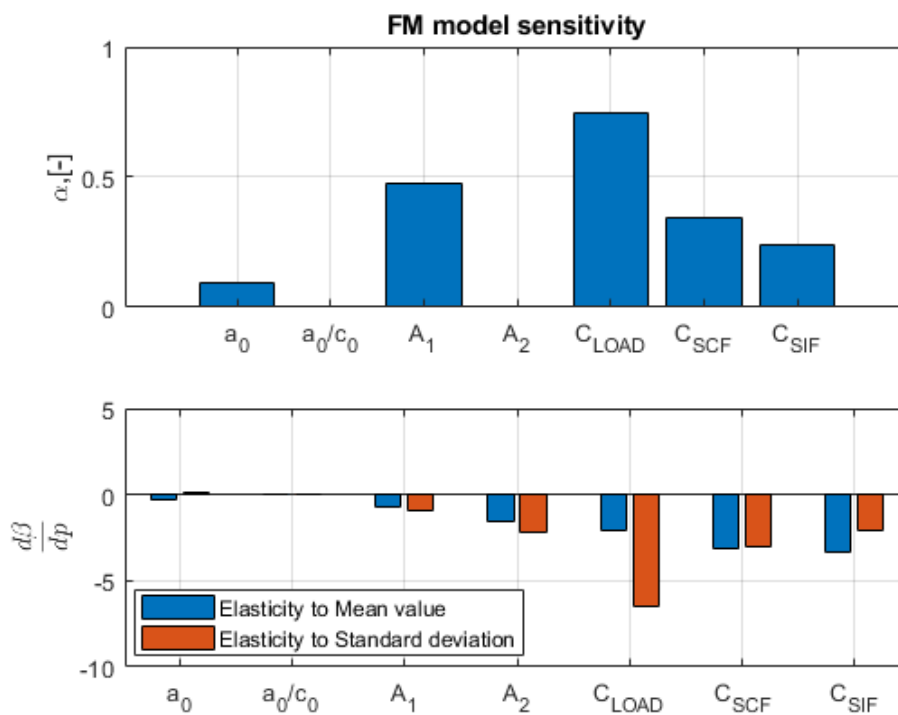


**Figure 36: FM model sensitivity for Transition Piece.**

The model is quite sensitive to uncertainties related to stress concentration, stress magnification factor and especially the load calculation – high  $C_{LOAD}$   $\alpha$  coefficient, both

mean value and standard deviation have significant influence (elasticity coefficient  $d\beta/dp$ ).

Based on the findings in (Santos, et al., 2017) that freely corroding monopile fails to satisfy the annual reliability requirement of  $\beta_{ann} \geq 3.3$  at 16<sup>th</sup> service year, cathodic protection is necessary throughout the lifetime of the structure. If monopile has cathodic protection (active throughout the lifetime) the allowable initial crack depth is also higher than estimated in (Santos, et al., 2017), see Figure 37. Simplified model in (Santos, et al., 2017) allowed only  $\sim 0.64\text{mm}$  initial cracks, while the updated model almost doubles the average allowable initial crack size to  $\sim 1\text{mm}$ . This again implies lower manufacturing costs of the monopile.

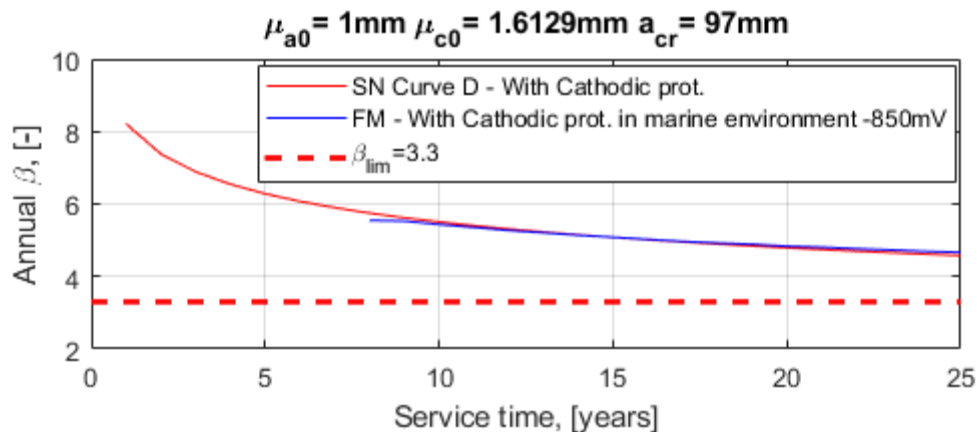
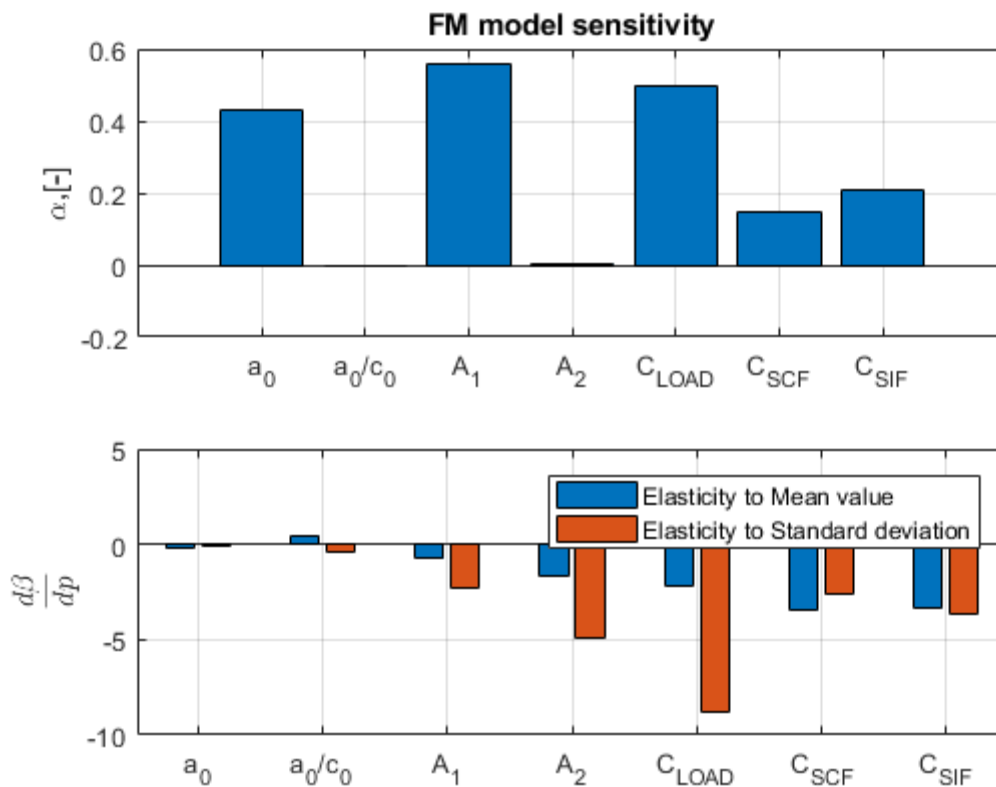


Figure 37: Results of FM model calibration for most critical Transition Piece node.



### Figure 38: Results of FM model calibration for most critical Transition Piece node.

As it was for the transition piece, the model sensitivities are similar – high influence of uncertainties related to load calculation and stress concentration/magnification factor can be observed in Figure 38. However, when cathodic protection is used, initial crack size is significantly more important parameter (higher  $\alpha$  factor in Figure 36 than in Figure 38). Higher relative importance of initial crack depth implies that monopiles (especially monopile welds) should be more thoroughly quality controlled during manufacturing than transition pieces.

## 2.4 Concluding remarks on reliability of tubular grouted connection with shear keys

Fatigue reliability of concrete grout and steel components of grouted connection with shear keys was assessed and found to be satisfactory at this stage of preliminary design. It is noted that when it comes to concrete grout reliability, it is important to assess both compression-compression and compression-tension stress states, as significant portion of damage accumulation appears to be induced by stresses varying from compression to tension. The concrete grout reliability models are highly sensitive to model errors arising from SN curve parameter estimation. Such model errors are a direct consequence of statistical uncertainties related to limited (and highly variable) fatigue test data of high strength concrete/grout and thus could be reduced by performing more fatigue tests as well as compiling and using bigger databases of fatigue test data, especially more data for 'compression to tension' is needed. An updated steel fatigue reliability model (based on fracture mechanics) shows high sensitivity uncertainties related to load (stress range), stress concentration/magnification factor calculations. Initial crack size at/around welds are significantly more important for monopile welds than it is for transition piece nodes, as suggested by sensitivity analyses. This implies higher quality requirements for monopile welds than for welds around shear keys. However, for welds in both - monopile and transition piece - larger initial cracks could be allowed, based on the results obtained using updated fracture mechanics model when compared to simplified model in (Santos, et al., 2017). Larger allowable initial cracks would potentially reduce the manufacturing costs of monopiles and transition pieces.

### 3. Reliability of piles and substructures under consideration of soil parameters

Within Work Package WP7.4 and the corresponding Deliverables D74.2 reliability based assessment of the foundation piles and the support structure should be conducted. These analyses are closely linked to Work Package WP7.2 and the corresponding Deliverables D72.2, since the executed analysis strongly based on the measured data from the performed foundation pile tests in Work Package WP7.2.

Section 3.1 deals with two major topics, which are focused on the reliability assessment of the foundation pile with respect to geotechnical ULS design requirements, where Section 3.2 focusses on the reliability of the substructure while taking the turbine and soil parameters into account.

#### 3.1 Reliability of the substructure under consideration of the turbine and soil parameters

Within Section 3.1 first, a new model error for the design methods of the axial tension bearing capacity is derived on basis of the additional incorporated pile load tests performed in WP7.2. Second, a reliability based study for typical offshore foundation piles in the North Sea is conducted, where the new derived model error is included. Using the calculated reliability based results, a new calibration approach regarding a more robust deterministic design was conducted. Thereby quality factors for the considered deterministic design methods were derived. These quality factors indicate on basis of the performed reliability based calculations the reliability regarding the axial tension bearing capacity within a deterministic design.

Altogether the executed tasks in Section 3.1 can be summarized as follows:

- Determination of a new model error for the tension capacity of offshore piles
  - Description of the applied design methods
  - Determination of the theoretical tension capacity for the performed pile load tests in WP7.2
  - Derivation of a model error from the calculated and measured data
- Assessment of design methods with respect to deterministic ULS design
  - Determination of the reliability index for typical pile dimensions and soil conditions in the North Sea
  - Comparison between the deterministic and reliability based design results
  - Derivation of quality factors for the deterministic design methods

### 3.1.1 Introduction

In the near future, several offshore wind farms are planned to be built in the North Sea to satisfy the demand for a high amount of renewable energy in Germany. As most shallow depth sea areas have already been exploited, a number of projects will be located in sea areas with relatively high water depths (exceeding 40 m). For such water depths, jacket and tripod support structures with mainly axially loaded foundation piles will probably be employed in most cases.

The axial bearing resistance of such piles is normally estimated according to the recommendation of API (American Petroleum Institute, 2014) by applying the so termed “Main Text” method. However, several investigations (e.g. (Lehane, et al., 2005) or (Cathie, 2012)) have shown that the application of the Main Text method, at least for foundation piles of wind energy converters, is not reliable and may lead to a significant deviation compared to the real in situ bearing capacity.

To enhance the reliability of design methods, 4 additional CPT-based design methods, namely ICP, UWA, Fugro and NGI, were recommended within API (American Petroleum Institute, 2014). These methods were calibrated on pile field tests, where basically the skin friction of a pile and the end bearing are estimated on basis of the cone resistance  $q_c$  measured in a CPT. It is believed that the proposed CPT-based design methods are more reliable than the API Main Text method. However, it is emphasized within the API (American Petroleum Institute, 2014) that care should be taken in the application of these methods, since experience is limited. Indeed, the application of the CPT-based methods leads in practice to a high deviation in the required pile length within a design. In this work package (WP7.4), two major issues are investigated:

First, a new derived model error for the axial tension bearing capacity is obtained from the model tests performed within WP7.2. These model tests were aligned with the corresponding boundary conditions for offshore foundation piles in the North Sea as well as with already available pile load tests in literature. An overview of the performed complementary pile load tests and already published pile load tests was given in the report for WP7.2.

Second, a comprehensive study is performed in which different deterministically designed pile-soil systems are investigated regarding the failure probability with reliability based approaches. Thereby, a new calibration approach is applied, where quality factors for each design method are derived. Based on these quality factors, an enhanced evaluation of a certain design method in question regarding the reliability of the predicted tensile bearing capacity can be done. Moreover, a more reliable as well as more robust deterministic design can be achieved by taking the proposed quality factors into. In this work package, only the tension bearing resistance of offshore foundation piles is investigated.

### 3.1.2 Determination of the model error

#### 3.1.2.1 Design methods

Within the ultimate limit state design for foundation piles of offshore support structures, it has to be ensured that the environmental induced loads are safely transferred into the subsoil. In this work package only tension loading is investigated.

The tension bearing capacity of an axially loaded pile consists basically of the mobilized friction between the pile outer shaft area and the surrounding subsoil. In case of an open-ended pile, two different conditions of the soil within a pile, namely “plugged” or “unplugged”, must be considered. In the unplugged case, resistance due to friction between the pile outer shaft area and the inner soil is assumed. In contrast to that, for the plugged case, only the resistances due to friction between the outer shaft area and the soil as well as the weight of the inner soil plug is taken into account. In both cases, also the weight of the pile is taken into account. The resulting pile resistance for the two mentioned conditions is given in Eq. (63). The calculation of the skin friction and the end bearing for all design methods was done according to API (American Petroleum Institute, 2014), besides minor adjustments for the API “Main Text” method which is described below.

$$R_c = \begin{cases} A_o \int f_t(z) dz + G_{plug} + G_{pile} & \text{plugged} \\ A_o \int f_t(z) dz + A_i \int \psi_i f_i(z) dz + G_{pile} & \text{unplugged} \end{cases} \quad (63)$$

where  $A_o$  = outer pile shaft area;  $f_t(z)$  = skin friction for tensile loading;  $A_i$  = inner pile shaft area;  $\psi_i$  = factor for adjusting the inner friction resistance;  $G_{plug}$  = effective weight of the inner soil plug;  $G_{pile}$  = effective weight of the pile

According to the API “Main Text” method, in this work package also referred to as API, the minimum of both conditions with respect to Eq. (63) is decisive and should be considered as the tension capacity. Regarding the pile capacity, it is stated in API (American Petroleum Institute, 2014) that the tensile capacity should be equal or less than the compressive capacity, since the friction resistance in tension is smaller due to the poisson’s ratio contraction of the pile shaft and the reduced vertical stresses around the pile compared to the friction resistance in compression. Hence, a reduction of the skin friction to 2/3 is taken into account for the API-method, since this factor is recommended by certification companies like the Germanischer Lloyd (Germanischer Lloyd, 2005). It is not clear if this factor also should be applied to the limited skin friction. However, for the analysis and calculations within this work package. The limit skin friction is also reduced according to Eq. (64). By doing so the relation of the friction for tension and compression of the CPT-based design methods is more matched. In case of the usage of a driving shoe the resistance of the inner soil friction is reduced to  $\psi_i = 0.8$  in practice for the API-method. This reduction is also applied within this work package.

$$f_t(z) = 2/3 \beta \sigma'_v \leq 2/3 f_{t,max} \quad (64)$$

where  $\beta_{API}$  = shaft friction factor from Table 1;  $\sigma'_v$  = effective vertical stress; and  $f_{t,max}$  = limit skin friction from Table 9.

Table 9: Design parameters for the API Main Text method

Relative Density $D_r$ [-]	$\beta_{API}$ [-]	$f_{t,max}$ [kPa]
0.35 - 0.65	0.37	81
0.65 - 0.85	0.46	96
0.85 - 1.00	0.56	115

The estimation of the relative density from a CPT should be done according to the proposed approach by (Jamiołkowski, et al., 1988) according to Eq. (65):

$$D_r = \frac{1}{2.96} \ln \left[ \frac{q_c/p_a}{24.94 \left( \frac{p'_m}{p_a} \right)^{0.46}} \right] \quad (65)$$

where  $q_c$  = measured cone tip resistance in kPa; and  $p'_m$  = effective mean in-situ soil stress in kPa.

In case of the CPT-based design methods, always a plugged condition for the tensile bearing capacity is assumed. Thereby the weight of the soil plug is indirectly considered in the outer friction resistance. In contrast to the API Main Text method, the outer skin friction of the CPT-based design methods was correlated directly with CPT measurements. The skin friction for the ICP-05, UWA-05 and Fugro-05 method can be calculated according to Eq. (66). The friction for the NGI-05 method is given by Eq. (67).

$$f_t(z) = u \cdot q_c \left( \frac{\sigma'_v}{p_a} \right)^a A_r^b \left( \max \left[ \frac{L-z}{D_o}; \nu \right] \right)^{-c} (\tan \delta_{cv})^d \quad (66)$$

where  $\sigma'_v$  = vertical effective stress in kPa;  $p_a$  = atmospheric stress 100 kPa;  $A_r = 1 - (D_i/D_o)^2$  pile displacement ratio;  $L$  = embedded pile length in m;  $z$  = current depth in m;  $D_o$  = pile outer diameter;  $\delta_{cv}$  = interface friction angle;  $a, b, c, d, u, \nu$  = Parameters according to Table 10.

$$f_t(z) = \frac{z}{p_a} \left( \frac{\sigma'_v}{p_a} \right)^{0.25} 2.1(D_r - 0.1)^{1.7} > 0.1\sigma'_v \quad (67)$$

In Eq. (68) the relative density is defined as

$$D_r = 0.4 \ln \left( q_c / 22 \sqrt{\sigma'_v \cdot p_a} \right) > 0.1 \quad (68)$$

Table 10: Design parameters for the ICP-05, UWA-05 and Fugro-05 method (American Petroleum Institute, 2014)

Method	Parameters					
	a	b	c	d	u	v
ICP	0.1	0.2	0.4	1	0.016	$A_r^{0.25}$
UWA	0.0	0.3	0.5	1	0.022	2
Fugro	0.15	0.42	0.85	0	0.025	$A_r^{0.5}$

### 3.1.2.2 Calculated tension capacity of tested piles

In the test facilities of the Leibniz University Hannover, 6 static axial pile pullout tests were performed by Fraunhofer IWES within work package WP7.2. Thereby the tension capacity of the tested piles was determined on basis of a deformation criterion for the pile head displacement.

All information regarding the execution of the pile test, like the preparation of the sand in the test pit, the evaluation of the soil conditions, the pile properties, the installation of the foundation piles, the execution of the pullout test as well as the measured load-displacement curves, are provided within the report for WP7.2.

Table 11 summarizes the measured pile capacities from WP7.2 and calculated pile capacities according to the applied design methods described in Section 3.1.2.1 for the 6 tested piles. In addition, the pile properties in terms of the slenderness ratio ( $L/D$ ) and the ratio of the outer pile diameter and the pile wall thickness ( $D/t$ ) are provided.

Table 11: Comparison of measured and calculated pile bearing capacities for the performed pile load tests in WP7.2

	Measured pile capacity [kN]	Calculated pile capacity [kN]					Pile properties [1]	
		API	ICP	UWA	Fugro	NGI	L/D	D/t
Pile 1	157.2	65.5	131.9	122.9	151.1	299.7	20.9	54.60
Pile 2	123.6	86.0	150.0	138.9	143.3	353.2	24.5	54.60
Pile 3	187.1	87.2	186.4	174.6	230.7	391.0	16.0	56.44
Pile 4	252.2	114.2	213.8	199.7	223.9	460.6	18.8	56.44
Pile 5	152.8	76.7	164.0	155.8	199.1	348.5	14.9	56.44
Pile 6	219.3	114.2	213.8	199.7	223.9	460.6	18.8	56.44

### 3.1.2.3 Derivation of the model error

The accuracy of a design method regarding the axial bearing capacity can be described by a model error, which is usually defined as the ratio of the calculated bearing capacity and the measured or real in situ bearing capacity of a pile according to Eq. (69).

$$\varepsilon_R = Q_c / Q_m \quad (69)$$

where  $Q_c$  = calculated bearing capacity;  $Q_m$  = measured bearing capacity

Taking into account several results of measurements and predictions a distribution of the model error can be obtained. A model error with a mean value close to unity in combination with a low coefficient of variation (COV) indicates a suitable design method. Several model error approaches regarding the reliability of design methods for axially loaded piles are available in the literature, like Achmus and Müller (Achmus & Müller, 2010), Jardine et al. (Jardine, et al., 2005), Lehane et al. (Lehane, et al., 2005), and Schneider et al. (Schneider, et al., 2008). Among them, different limitations regarding soil conditions, installation methods and pile specifications are used.

A relatively new evaluation of the design methods is presented by Yang et al. (Yang, et al., 2015), which is based on a new assessed database with 80 pile load tests in total. The limitations and the corresponding statistical data in terms of the mean and the COV are presented in Table 12. The design methods yield relatively high COVs in between 34 - 55 %. Also the mean values deviate from unity to approximately 10 - 30 %. It should be noticed that only the statistic values of the simplified methods are presented, since these methods are investigated here. According to (Yang, et al., 2015), the full design approaches of the ICP and UWA method yield a smaller standard deviation compared to the simplified approaches ICP-05 and UWA-05.

The model error strongly depends on the chosen soil, the installation and loading conditions, and the pile material and geometry. By choosing project specified boundaries, a more reliable performance behavior of a certain design method can be obtained. By restricting the database only to tension loaded open-ended steel piles which were impact-driven, statistical values for the model error by Jardine et al. (Jardine, et al., 2005), Lehane et al. (Lehane, et al., 2005), and Schneider et al. (Schneider, et al., 2008) are also presented in Table 12. For these model errors, less deviation in combination with a mean value closer to unity compared to the overall model error by Yang et al. (Yang, et al., 2015) can be noticed.

To cover the usual soil conditions and typically used pile dimensions for wind energy converters in the North Sea, Achmus and Müller (Achmus & Müller, 2010) added

additional restrictions regarding the density of the soil and the slenderness ratio of a pile. By considering these restrictions, only 6 pile load tests remain relevant. The mean and the standard deviation of the model error are also shown in Table 12. In comparison to the model errors presented before, the deviation of the model error by Achmus and Müller (Achmus & Müller, 2010) are slightly reduced for all methods. The mean value for the API, ICP-05 and UWA-05 clearly reduced, whereas the mean value for the Fugro-05 and NGL-05 method increased.

In addition, Table 4 presents the statistics regarding the model error for the API method reported by Bea et al. (Bea, et al., 1999), Chen et al. (Chen, et al., 2009) and Chen & Gilbert (Chen & Gilbert, 2014). These statistics were derived from examination of different storm events in the Gulf of Mexico. Due to the knowledge of the storm impact on the foundation piles and the corresponding failure rate of the foundation piles, a back-calculation of the in situ resistance, and therefore, the mean value and the COV of the model error was possible. As it can be seen, a mean value for the model error between 0.33 and 0.50 was obtained, indicating that the API design method is highly conservative. Regarding the variability, a COV of 30 % was determined, which is in range with the observation by Achmus and Müller (Achmus & Müller, 2010).

**Table 12: Model errors for the axial tension capacity of piles in literature**

Literature	Bias [-]	Variability [-]	Distribution type [-]	Test Number [-]	Pile Number [-]	Limitations [-]
Bea et al. (1999)	$\mu_{(Q_c/Q_m)}$ API: 0,33- 0,50	--	--	>250 platforms (4-8 pile at each platform)		
Chen et al. (2009)	$\mu_{(Q_c/Q_m)}$ API: 0.5	--	--	2 platforms (14 piles)		Foundation piles for offshore platforms (L/D>40)
Chen & Gilbert (2014)	API	$COV_{(Q_c/Q_m)}$ 0,30	--	13 platforms (67 piles)		
Yang et al. (2015)	$\mu_{(Q_c/Q_m)}$ API: 0,90 ICP: 0,70 UWA: 0,90 Fugro: 1,21 NGI: 1,23	$COV_{(Q_c/Q_m)}$ 0,55 0,34 0,40 0,45 0,47	--	80		Open- and close- ended, steel and concrete piles, circular and square pile shape, tension and compression loading
Jardine et al. (2005)	$\mu_{(Q_c/Q_m)}$ API: 0,89 ICP: 1,05	$COV_{(Q_c/Q_m)}$ 0,68 0,28	--	API: ICP:17	19	Open-ended, steel piles, tension loading
Lehane et al. (2005)	$\mu_{(Q_c/Q_m)}$ API: 0,72 ICP: 0,90 UWA: 0,91 Fugro: 0,90 NGI: 1,01	$COV_{(Q_c/Q_m)}$ 0,75 0,25 0,23 0,31 0,36	Lognormal	15		Open-ended, steel piles, tension loading
Schneider et al. (2008)	$\mu_{g(Q_c/Q_m)}$ * API: 0,73 ICP: 0,96 UWA: 0,97 Fugro: 0,92 NGI: 1,04	$\sigma_{\log(Q_c/Q_m)}$ ** 0,64 0,16 0,19 0,32 0,29	Lognormal	16		Open-ended, steel piles, tension loading
Achmus & Müller (2010)	$\mu_{(Q_c/Q_m)}$ API: 0.60 ICP: 0.88 UWA: 0.82 Fugro: 1.03 NGI: 1.15	$COV_{(Q_c/Q_m)}$ 0.29 0.15 0.14 0.28 0.21	--	6		Open-ended, steel piles, tension loading, dense to very dense sand, L/D = 15 - 40, D/t = 21 - 34

\* $\mu_{g(Q_c/Q_m)}$  Geometric mean; \*\* $\sigma_{\log(Q_c/Q_m)}$  Standard deviation of  $\log(Q_c/Q_c)$

The related pile capacities  $Q_c/Q_m$  and therefore the model errors in terms of the mean value, standard deviation (SD), and the COV for the performed pile load tests in WP7.2 are presented in Table 13. Corresponding to the chosen pile lengths and diameters, the slenderness ratios lie between  $L/D = 15 - 25$ . The range of the wall thickness  $D/t = 55 - 57$  is comparable to the offshore piles used in the North Sea. Regarding the mean value, it can be noticed that the ICP-05, UWA-05 and Fugro-05 are close to unity, especially the ICP-05 method. In contrast, the API method underestimates the axial bearing capacity almost by half, where the NGI-05 method over predicts the capacity by a factor of 2.18. Compared to the model error presented by Achmus and Müller (Achmus & Müller, 2010), the deviation has been slightly reduced for the CPT-based methods, where the deviation for the API Main Text method has been reduced almost by half. Regarding the API method, it has been stated above that this method is very conservative. The relative high overestimation of the capacity by the NGI-05 method is somewhat surprising. This may be caused by the fact that the NGI-05 method was calibrated on pile load tests with a relatively small  $D/t$  ratios and does not take into account the pile wall thickness within the design calculation.

**Table 13: Derived model errors on basis the performed pile load tests in WP7.2**

Pile load tests	Related pile capacity $Q_c/Q_m$ [kN]					Limitations [-]
	API	ICP	UWA	Fugro	NGI	
Pile 1	0.42	0.84	0.78	0.96	1.91	Open-ended, steel piles, tension loading, dense to very dense sand, $L/D=15-25$ , $D/t=55-57$
Pile 2	0.70	1.21	1.12	1.16	2.86	
Pile 3	0.47	1.00	0.93	1.23	2.09	
Pile 4	0.45	0.85	0.79	0.89	1.83	
Pile 5	0.50	1.07	1.02	1.30	2.28	
Pile 6	0.52	0.98	0.91	1.02	2.10	
Mean	0.51	0.99	0.93	1.09	2.18	
SD	0.10	0.14	0.13	0.16	0.37	
COV	0.19	0.14	0.14	0.15	0.17	

To expand the database of these 6 pile load tests, another 6 additional pile load tests mentioned in Achmus & Müller (Achmus & Müller, 2010) were reassessed and included within the estimation of the model error. Table 14 summarizes the measured in situ pile capacities, the calculated bearing capacities according to the applied design methods stated above, the slenderness ratio, and the  $D/t$  ratio for the reassessed pile load tests.

Table 14: Comparison of measured and calculated pile bearing capacities for reassessed pile load tests from the literature

Pile load tests	Measured pile capacity [kN]	Calculated pile capacity [kN]					Pile properties [1]	
		API	ICP	UWA	Fugro	NGI	L/D	D/t
EURIPIDES I	2900	2710	3834	3519	5061	4087	40.0	21.19
CLAROM CS	396	270.3	370.3	345.3	400.3	605.3	34.0	25.51
CLAROM CL	459	270.3	370.3	345.3	400.3	605.3	34.0	25.51
GOPAL R1	1450	1046	1007	848.7	845.7	1730	42.2	33.85
HOOGZAND I	830	129.1	648.1	671.1	732.1	808.1	19.7	22.25
HOOGZAND III	550	75.2	425.2	458.2	604.2	517.2	14.9	22.25

Table 15 provides all related pile capacities  $Q_c/Q_m$  of the considered pile load tests from WP7.2 and the reassessed pile load tests given in Table 14. In addition, the statistics for the so obtained model errors are specified. The slenderness ratio and the D/t ratio differ considerably. Nevertheless, these ratios are relevant to industry practice. Since the NGI-05 method obviously does not capture the capacity of the tested piles as described above, only the reassessed pile load tests were considered.

Table 15: Model errors on basis performed pile load tests in WP7.2 and reassessed pile load tests

Pile load tests	Related pile capacity $Q_c/Q_m$ [kN]					Limitations [-]
	API	ICP	UWA	Fugro	NGI*	
Pile 1	0.42	0.84	0.78	0.96	-	
Pile 2	0.70	1.21	1.12	1.16	-	
Pile 3	0.47	1.00	0.93	1.23	-	
Pile 4	0.45	0.85	0.79	0.89	-	Open-ended, steel piles, tension loading, dense to very dense sand, L/D=15-40, D/t=21-57
Pile 5	0.50	1.07	1.02	1.30	-	
Pile 6	0.52	0.98	0.91	1.02	-	
EURIPIDES I	0.93	1.32	1.21	1.75	1.41	
CLAROM CS	0.68	0.94	0.87	1.01	1.53	
CLAROM CL	0.59	0.81	0.75	0.87	1.32	
GOPAL R1	0.72	0.69	0.59	0.58	1.19	
HOOGZAND I	0.16	0.78	0.81	0.88	0.97	
HOOGZAND III	0.14	0.77	0.83	1.10	0.94	
Mean	0.52	0.94	0.89	1.06	1.23	
SD	0.23	0.19	0.17	0.29	0.24	
COV	0.44	0.20	0.19	0.27	0.19	

\* Only reassessed pile load tests from Achmus & Müller (2010) are considered

As it can be seen, the mean value has been slightly reduced for the ICP-05, UWA-05, and Fugro-05 method compared to the model error related to the tested piles. The mean value for the API method has not been significantly changed. Regarding the deviation, an increase can be noticed in all cases. For the reassessed NGI-05 method, only the mean value has been increased, whereas the deviation is almost the same. Altogether, the ICP-

05 and UWA-05 methods seem to be more suitable for the determination of the tensile capacity compared to the other investigated design methods.

For a complete description of a model error, the distribution type is required as well. Therefore, all derived model errors of all design methods specified in Table 15 were tested for a normal and lognormal distribution by applying a Kolmogorov-Smirnov (KS) and Anderson-Darling (AD) test with a significance level of  $\alpha = 5\%$ . Table 16 shows the statistics and the adjusted critical value for the performed tests. By observing Table 16, it appears that the API method does not follow a lognormal distribution, where a normal distribution may be possible. For the CPT-based methods, no tested distribution type can be rejected. However, too few load tests are available for a reliable conclusion. Since negative values can be excluded for the model error using a lognormal distribution, this type of distribution seems to be more suitable for all design methods. In addition, Figure 39 depicts a Q-Q plot for a lognormal distribution of the model error for the API method in comparison to the ICP-05 method. Within a Q-Q plot, the observed (or tested) values are rearranged in an ascending order. Thereafter, the corresponding quantile values of the observations are compared to quantile values of a theoretical (or assumed) distribution with specified mean and standard deviation. As it can be seen from Figure 39, the deviations are more or less representative.

Table 16: Test statistics of the KS and AD test for the derived model errors with  $\alpha = 0.05$

Test Statistics		API	ICP	UWA	Fugro	NGI	
Adjusted critical value		0.242*				0.321**	
KS-Test	D <sub>n</sub>	N	0.154	0.183	0.140	0.170	0.191
		LN	0.265	0.167	0.143	0.184	0.195
Adjusted critical value		0.648*				0.773**	
AD-Test	A <sup>2</sup>	N	0.297	0.376	0.293	0.412	0.234
		LN	0.900	0.246	0.241	0.317	0.271
*n=12; **n=6							

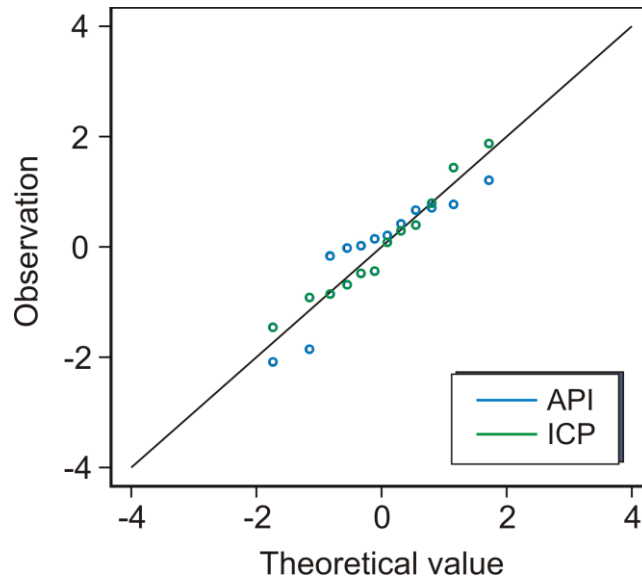


Figure 39: Q-Q plot for a lognormal distribution of the model error for the API method and the ICP-05 method

### 3.1.3 Assessment of design methods

#### 3.1.3.1 Pile-Soil System under consideration

For the performed study, typical site conditions for the North Sea and typical ranges for the foundation pile properties are assumed.

Since the subsoil in the German North Sea mostly consists of dense sands with only limited intermediate cohesive layers, two idealized CPT profiles for homogeneous dense ( $D_r = 0.75$ ) and very dense ( $D_r = 0.90$ ) sands were considered, where the mean value of the grain size at 50 % of the grain size distribution was chosen to  $\mu_{D50} = 0.4$  mm. The mean value of the effective unit weight was assumed to be  $\mu_\gamma = 10$  kN/m<sup>3</sup> in both cases, since this value represents a reasonable estimate for both soil densities.

The choice of pile properties depends on the type of support structure for the wind turbine, the water depth, and the subsoil condition at the desired location. In general, it can be said that pile slenderness ratios between  $L/D = 15$  and  $L/D = 40$  are used for jacket support structures of offshore wind turbines. Thereby, the pile outer diameter is varying between  $D = 1$  m and  $D = 3$  m, where the pile embedded length is commonly chosen to be between  $L = 20$  m and  $L = 60$  m. The regular pile wall thickness which is mostly used can approximately be determined by  $t = D/50$ . Figure 40 shows the considered pile properties and soil conditions.

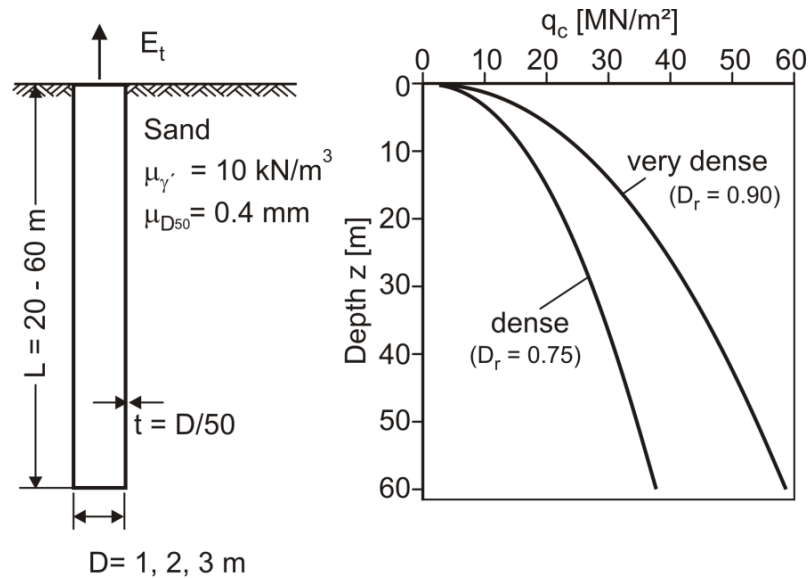


Figure 40: Pile-soil systems under consideration

### 3.1.3.2 Deterministic design

Within a deterministic design, the choice of characteristic soil parameters is not a straight forward task. According to Ref. (Simpson, 2012) characteristic values are chosen 0.5 times the standard deviation below the mean value or above, if this is unfavorable, on the safe side. In the USA, characteristic values 0.5 to 0.75 times the standard deviation below the mean value are typically chosen. Taking into account an overall COV of 10 % for the unit weight as well as a COV of 10 % for the grain size at 50 % of the grain size distribution a characteristic value of  $\gamma' = 9.5 \text{ kN/m}^3$  and  $D_{50} = 0.42 \text{ mm}$  were chosen for the deterministic design. Hence, the chosen characteristic values correspond to the values 0.5 times the standard deviation separated from the mean on the corresponding safe side. Therewith 30 % quantile values were chosen as characteristic design parameter. In contrast, in practice, the cone tip resistance  $q_c$  is usually taken directly into account without a safety margin. Thus, the  $q_c$ -profiles according to Figure 40 were considered without reduction in the deterministic design. The internal friction angle was determined by the approach proposed by Kulhawy and Mayne (Kulhawy & Mayne, 1990) considering the characteristic value for  $\gamma'$  and the  $q_c$ -profiles. Hence, due to consideration of a reduced  $\gamma'$ -value, a certain quantile value on the safe side is considered for the internal friction angle. Characteristic tension loads of  $E_c = 3, 6, 9, \text{ and } 12 \text{ MN}$  were considered for the pile foundation. According to Holicky et al. (Holicky, et al., 2007), a characteristic load corresponding to the 95 % quantile value is representative for a 50 year extreme event. In contrast to onshore pile design, where the load is distinguished in dead and live load, special design load cases are considered for offshore structures. Within these design load cases, a combined load is determined for a certain event. Hence, only one harmonized partial safety factor has to be applied for the load. According to the German standard DIN EN 61400-3 (DIN EN 61400-3, 2010) a partial safety factor of  $\gamma_E = 1.35$  has to be applied for the load due to the design load case 6.1, which considers the ultimate limit state proof of the pile foundation. According to DIN 1054 (DIN 1054, 2010) a partial safety factor of  $\gamma_R = 1.50$  should be applied for the resistance of a tension pile, if no pile capacity load test has been executed. Thus, a global safety factor of approximately  $\text{GSF} = 2.03$  is prescribed by application of the appropriate German standards. In this work package, the

determined results are referred to the GSF. In this way, an easier comparison to deviating partial safety factors, and therefore, GSFs of other standards is possible.

On basis of the assumed soil conditions, the considered embedded pile length range and slenderness ratio range in Section 3.1.3.1 as well as the chosen characteristic values for the resistance and load parameters and the prescribed GSF above, Table 17 summarises the considered design cases by specifying suitable corresponding pile diameters for the assumed characteristic loads. For each design method and relative density, six deterministic designs were performed. Thus, in total 60 deterministic design cases were investigated and assessed on basis of reliability based analyses.

Figure 41 and Figure 42 depict the development of the GSF with the embedded pile length for both considered soil conditions in terms of the relative density  $D_r$ . For the prescribed GSF of 2.03, a strong deviation in the required embedded pile lengths can be noticed for both densities. This deviation between the design methods is also illustrated in Figure 43 for all considered design cases. In general, almost the same deviation can be noticed for both densities. For  $D_r = 0.75$ , the deviation varies from  $\Delta L = 15 - 29$  m, where for  $D_r = 0.90$ , the deviation is in between  $\Delta L = 16 - 23$  m. Hence, the estimation of the required pile length may result in a difficult task for engineers in practice.

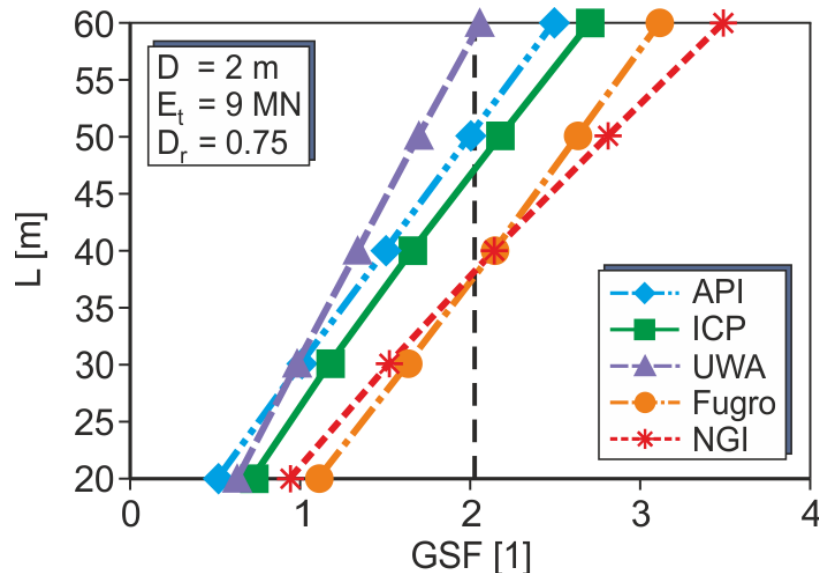


Figure 41: Development of the GSF with the embedded pile length for the considered design methods for the dense soil state of design case 3

Table 17: Assumed characteristic loads and corresponding pile diameters in question

Design Case	1	2	3	4	5	6
D [m]	1	2	2	3	2	3
$E_t$ [MN]	3	6	9	9	12	12

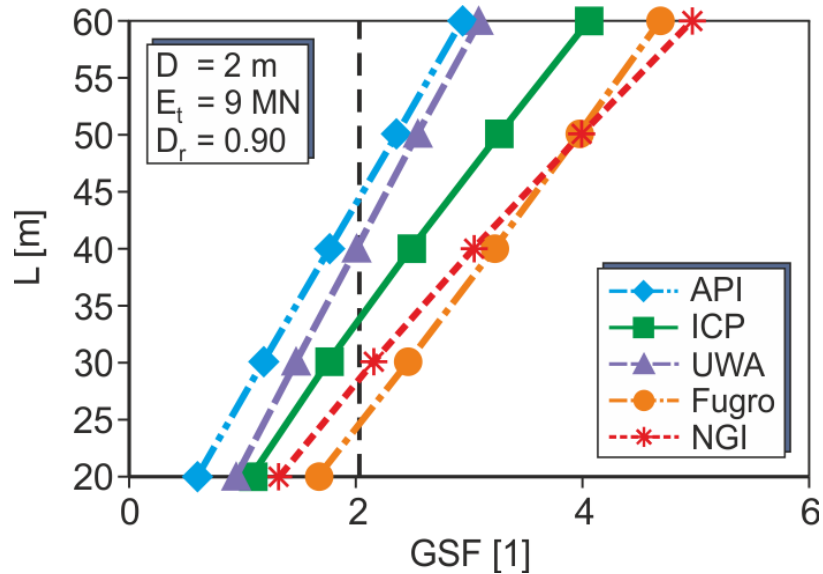


Figure 42: Development of the GSF with the embedded pile length for the considered design methods for the very dense soil state of design case 3

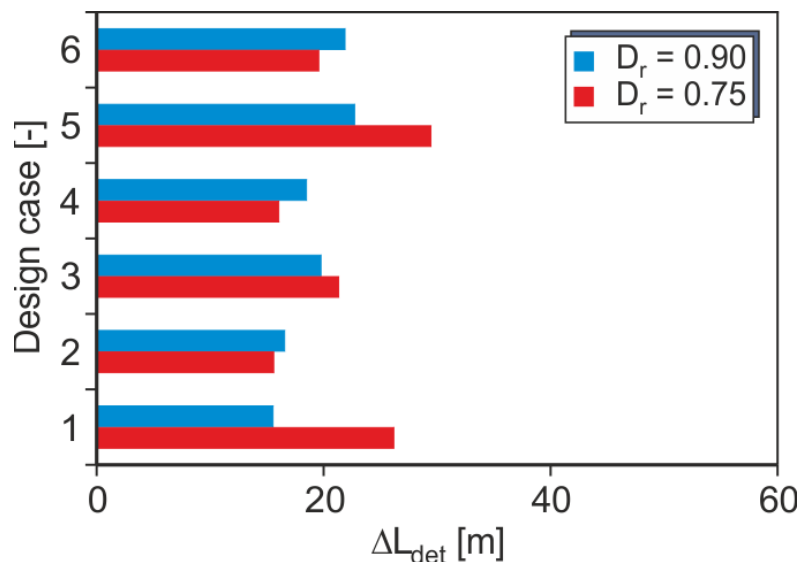


Figure 43: Deviation of the required embedded pile lengths due to deterministic design within the considered design methods

### 3.1.3.3 Stochastic soil model

The estimation of a stochastic axial pile bearing resistance is carried out by the application of a stochastic subsoil model according to the recommendations given by Schmoor (Schmoor, 2017). This model consists of five input variables, namely the cone tip resistance  $q_c$ , the unit buoyant weight of the soil  $\gamma'$ , the grain size at 50 % of the grain size distribution  $D_{50}$ , a transformation error for the estimation of the internal friction angle from a CPT  $\varepsilon_{t,\varphi}$ , and the model error  $\varepsilon_R$  for the design method in question specified in Table 15. Figure 44 depicts an overview of the applied subsoil model and the estimation of the stochastic resistance.

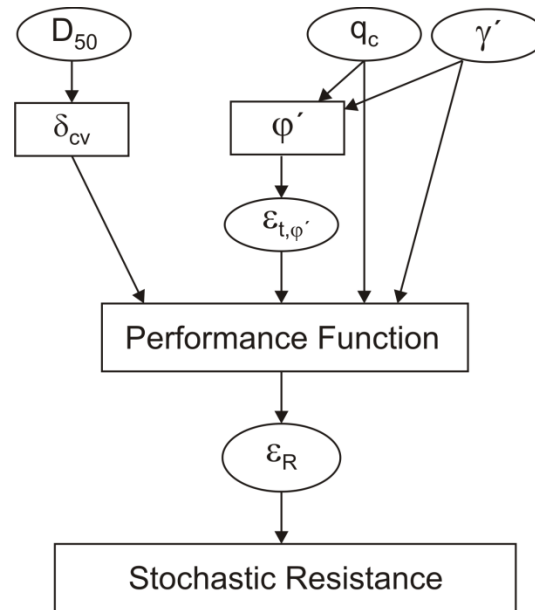


Figure 44: Overview of the stochastic subsoil model

The cone tip resistance and the unit weight were simulated over depth by the application of a 1-D autocorrelated field with an exponential autocorrelation function according to Eq. (70). Thereby, an autocorrelation length of 0.05 m for  $q_c$  and 2.5 m for  $\gamma'$  are applied, respectively. Hence, for the friction angle, a profile over depth was calculated. Thereby, the corresponding transformation uncertainty proposed by Phoon and Kulhawy (Phoon & Kulhawy, 1999) is taken into account. The geotechnical input variable  $D_{50}$  was modeled as single variable.

$$\rho(\tau/\theta) = \exp(-\tau/\theta) \quad (70)$$

where  $\rho$  is the autocorrelation between two points,  $\tau$  = separation distance, and  $\theta$  = autocorrelation length.

Since the model error is directly applied to the performance function,  $\varepsilon_R$  was modeled as a single variable. The stochastic load  $E$  is also modeled directly by a single variable. The applied statistical values regarding the mean, the COV, and the distribution type are chosen in accordance with the recommendation by Holicky et al. (Holicky, et al., 2007).

To ensure that physically reasonable values were realized and used within the stochastic calculations, physical lower and upper boundaries were specified for the geotechnical input variables. Table 18 summarizes the stochastic values used for the considered input parameters and the corresponding physical boundaries.

**Table 18: Assumed stochastic values for the input variables and physical boundaries**

Variable	Char. Value	Mean	COV	Type*	Dimension*	Physical Boundaries
$q_c$	According to Figure 40		94.01 %**	B	1-D field	0.1 - 100 MPa
$\gamma'$	9.5 kN/m <sup>3</sup>	10 kN/m <sup>3</sup>	23.25 %**	B	1-D field	7 - 13 kN/m <sup>3</sup>
$D_{50}$	0.42 mm	0.40 mm	10 %	B	SV	0.06 - 2 mm
$\varepsilon_{t,\varphi'}$	-	0 °	$\sigma = 2.8$ °	N	1-D field	30 - 45 °
$\varepsilon_{R,API}$	-	0.52	44 %	LN	SV	-
$\varepsilon_{R,ICP}$	-	0.94	20 %	LN	SV	-
$\varepsilon_{R,UWA}$	-	0.89	19 %	LN	SV	-
$\varepsilon_{R,Fugro}$	-	1.06	27 %	LN	SV	-
$\varepsilon_{R,NGI}$	-	1.23	19 %	LN	SV	-
E	3, 6, 9, 12 MN	0.6 $E_t$	35 %	G	SV	-

\* B = Beta, N = Normal, LN = Lognormal, G = Gumbel, SV = Single Variable

\*\* Point COV; for L = 20 - 60 m corresponding COV is in range of  $COV_{q_c} = 6.64\% - 3.84\%$  and  $COV_{\gamma'} = 10.87\% - 6.57\%$

Based on the assumed stochastic values for the input variables, global sensitivity values (also called “ $\alpha$ -values”) can be determined by comparing the impact on the resistance for input values one standard deviation under and above the mean value in comparison to the mean value. In this way, the influence of each variable on the resistance is characterized in a comparable way. Figure 45 depicts normalized  $\alpha$ -values for each design method. Compared to uncertainties arising from subsoil conditions, it can be seen that the model error represents the most dominant source of uncertainty. This is also in agreement with the previous observations ( Dithinde, et al., 2011) and (Gilbert & Tang, 1995)). Within the uncertainties from the subsoil, it can be seen that for the CPT-based methods the cone tip resistance has the most impact on the resistance.

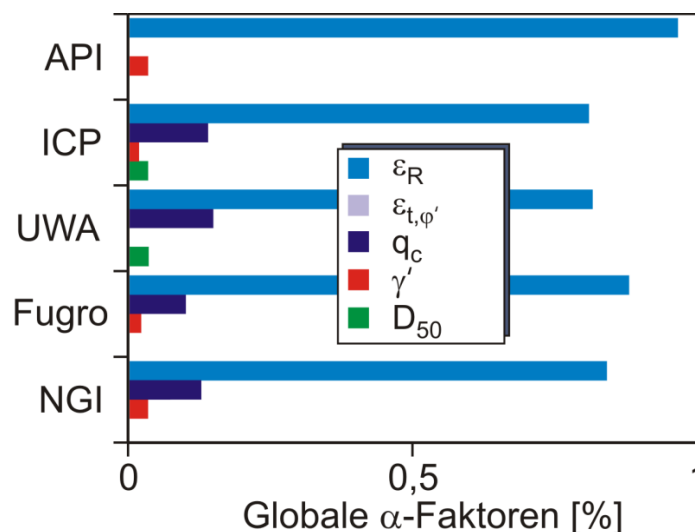


Figure 45: Sensitivity values for the basic variables (cf. Table 18)

### 3.1.3.4 Reliability based design

On basis of the described stochastic subsoil model and loading condition in Section 3.1.3.3, a Monte Carlo Simulation with 6 Million realizations for each of the 60 design cases was executed. Thereby, the pile embedded length was varied and the pile length corresponding to the reliability index  $\beta = 3.8$  required for a ULS design according to Eurocode 0 (Eurocode 0, 2010) was sought. Figure 46 and Figure 47 depict the calculated reliability index over the embedded pile length for both densities, where design case 3 is shown for all considered design methods. For both densities, still, a deviation regarding the required embedded pile length can be noticed with respect to the deterministic design. For the same reliability index of  $\beta = 3.8$ , it can be seen that the API-method leads to a required pile length of 53 m, where the ICP-method leads to a pile length of 33 m in case of  $D_r = 0.90$ . However, it is obvious that a longer pile has a higher bearing resistance, and therefore, a lower failure probability. Since the real bearing capacity and the variation for the subsoil parameters, and therefore, the real curve of the reliability index over depth is unknown, Figure 46 and Figure 47 should be interpreted that in case of  $D_r = 0.90$  for  $\beta = 3.8$  the embedded pile length should be in a range between approximately 33 – 53 m. However, since the model error for the API-method indicates a much higher COV in comparison to the CPT-based design methods, the results of the API-method are not taken into account for further evaluation. In this way, the API-method is considered as not reliable as the CPT-based methods.

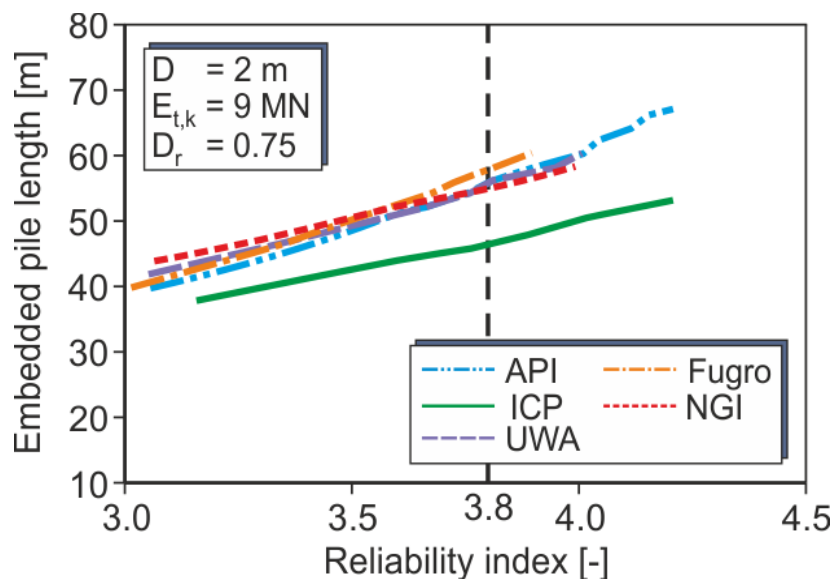


Figure 46: Calculated reliability Index over the embedded pile length with  $D_r = 0.75$  for design case 3

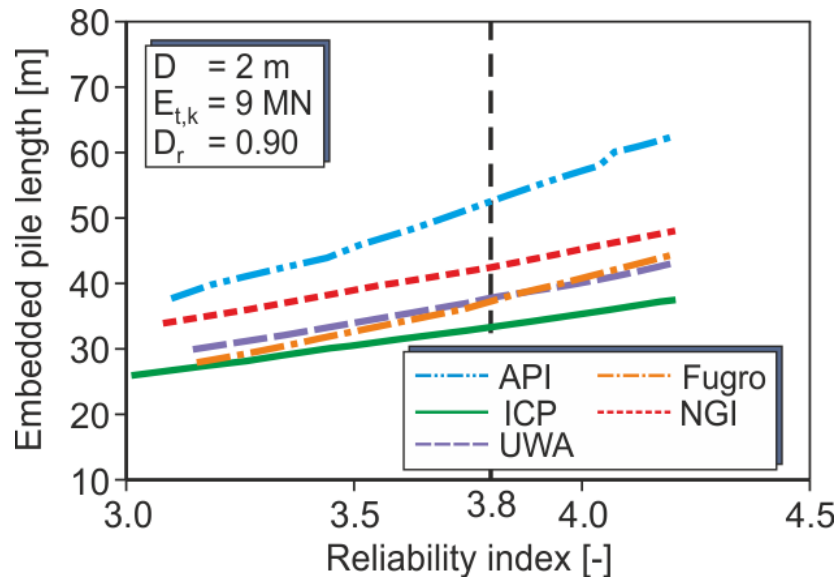


Figure 47: Calculated reliability Index over the embedded pile length with  $D_r = 0.90$  for design case 3

### 3.1.3.5 Comparison of deterministic and reliability based design

Figure 48 elucidates the deviation within the different design methods in the required embedded pile length of the reliability based results only for the CPT-based design methods in relation to the deterministic based results for the 6 considered design cases. For the design cases 2 to 6, almost half the deviation with respect to the deterministic design can be seen for the reliability based design, where for design case 1, a lower deviation can be noticed. However, it should be emphasized that the deviations for the embedded pile length due to the deterministic design result from 5 design methods, where the deviations due to reliability based design result only from the 4 CPT-based design methods. In the same way, Figure 49 shows the mean required embedded pile length of all design methods due to a reliability based design in relation to the deterministic design. Hence, for both densities a slightly increase of the piles embedded length is required in comparison to the deterministic approach.

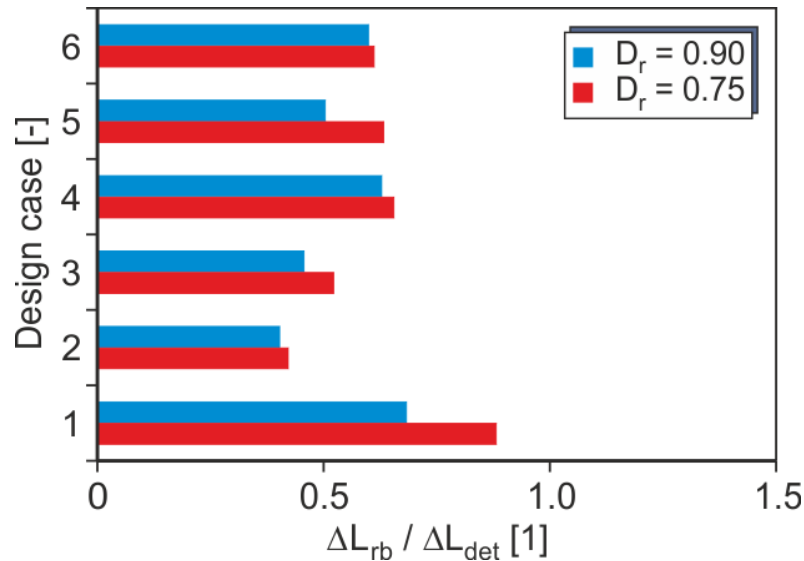


Figure 48: Deviation in the required embedded pile length for the reliability based designs only of the CPT-based methods in comparison to deterministic designs

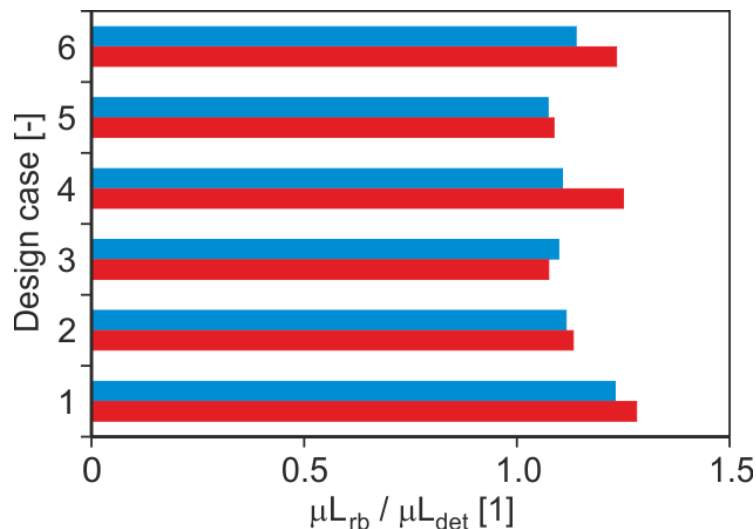


Figure 49: Comparison of the mean required embedded pile length  $\mu L$  due to reliability based designs only of the CPT-based methods and deterministic designs

### 3.1.3.6 Evaluation of design methods

A new calibration approach, where the minimum and maximum embedded pile lengths of all design methods, except the API-method, are considered as the upper and lower boundaries for a corresponding reliability index is investigated. Within this assumption, the mean value of the required embedded pile length is assumed as the most likely outcome within this range for all design cases. Thus, an integration of all CPT-based design methods and model errors is executed. In that way, an indirect increase of the assumed database for the model error is done. From the relationship between the deterministic design and the embedded pile length (see Figure 46 and Figure 47) the corresponding GSF can be obtained for the assumed lower and upper bound as well as for the mean required embedded pile length. Table 19 summarizes the required GSFs for each design method according to the new introduced approach. By dividing the GSF by the partial safety factor for the load, again the corresponding partial safety factor for the resistance

can be obtained. As it can be seen, a strong deviation within the investigated range of the pile diameters and loads occur. For a more detailed evaluation of the design methods, quality factors are introduced in the next Section.

**Table 19: Required GSF according to the new calibration approach**

	$D_r = 0.75$					$D_r = 0.90$				
	API	ICP	UWA	Fugro	NGI	API	ICP	UWA	Fugro	NGI
$GSF_{min}$	1.93	2.25	1.77	2.53	2.70	1.39	2.31	1.81	2.67	2.59
$GSF_{max}$	2.95	2.63	1.97	3.59	4.34	2.07	2.48	2.04	3.94	3.83
$GSF_{mean}$	2.20	2.38	1.88	2.98	3.11	1.64	2.38	1.95	3.28	2.93

For each design method and soil's relative density, quality factors  $\eta$  are obtained according to Eq. (71). Thereby, the calculated GSFs for the mean value of the required embedded pile length due to the new calibration approach were related to the current prescribed GSF of 2.03. By doing so, an evaluation of the deterministic design in terms of  $\eta$  with respect to the reliability based result due to the introduced calibration approach is achieved. For  $\eta = 1$ , no adaption if the GSF or partial safety factor is required. The distance from unity for  $\eta$  indicates the rate for a required adaption of a certain design method by the  $\eta$ -value regarding the assumed most likely outcome. Thereby  $\eta$  higher than unity indicates an overestimation of capacity by the design method and vice versa.

$$\eta = GSF/2.03 \quad (71)$$

Figure 50 depicts the regression lines of the quality factors for each design method, pile diameter and soil relative density as a function of the load. As it can be seen, the UWA and the ICP-method are the most robust ones regarding the pile diameter, soil density and the load. Thereby, the ICP-method is more robust regarding the soil density, where the UWA-method is more robust regarding the overall behavior. A strong deviation can be noticed for the API-, Fugro- and NGI-methods. Especially for the Fugro-method, a strong deviation regarding the pile diameter can be seen, where for the API-method a strong deviation regarding the density can be noticed.

Altogether it can be stated that on basis of the investigated pile-soil systems and the assumed model error the UWA-method and the ICP-method are the most robust ones. However, for the UWA-method a quality factor of approximately  $\eta_{UWA} = 0.94$  is suggested to be applied to the GSF or partial safety factor of the resistance with respect to the prescribed GSF of 2.03 ( $\gamma_E = 1.35$  and  $\gamma_R = 1.50$ ). In case of the ICP-method, a quality factor of  $\eta_{ICP} = 1.17$  should be considered within a deterministic design, since the ICP-method tends to overestimate the capacity. However, it should be emphasized that for all design methods the application of the corresponding quality factor for an equal deterministic design case leads to the same embedded pile length, since the quality factors compensate an overestimation or underestimation of the pile capacity within the design methods. It should also be emphasized that with the application of the API-method with the corresponding quality factors the same reliability regarding the design method is assumed as for the CPT-design methods. However, as mentioned before, the model error of the API-method indicates a lower reliability compared to the CPT-design methods.

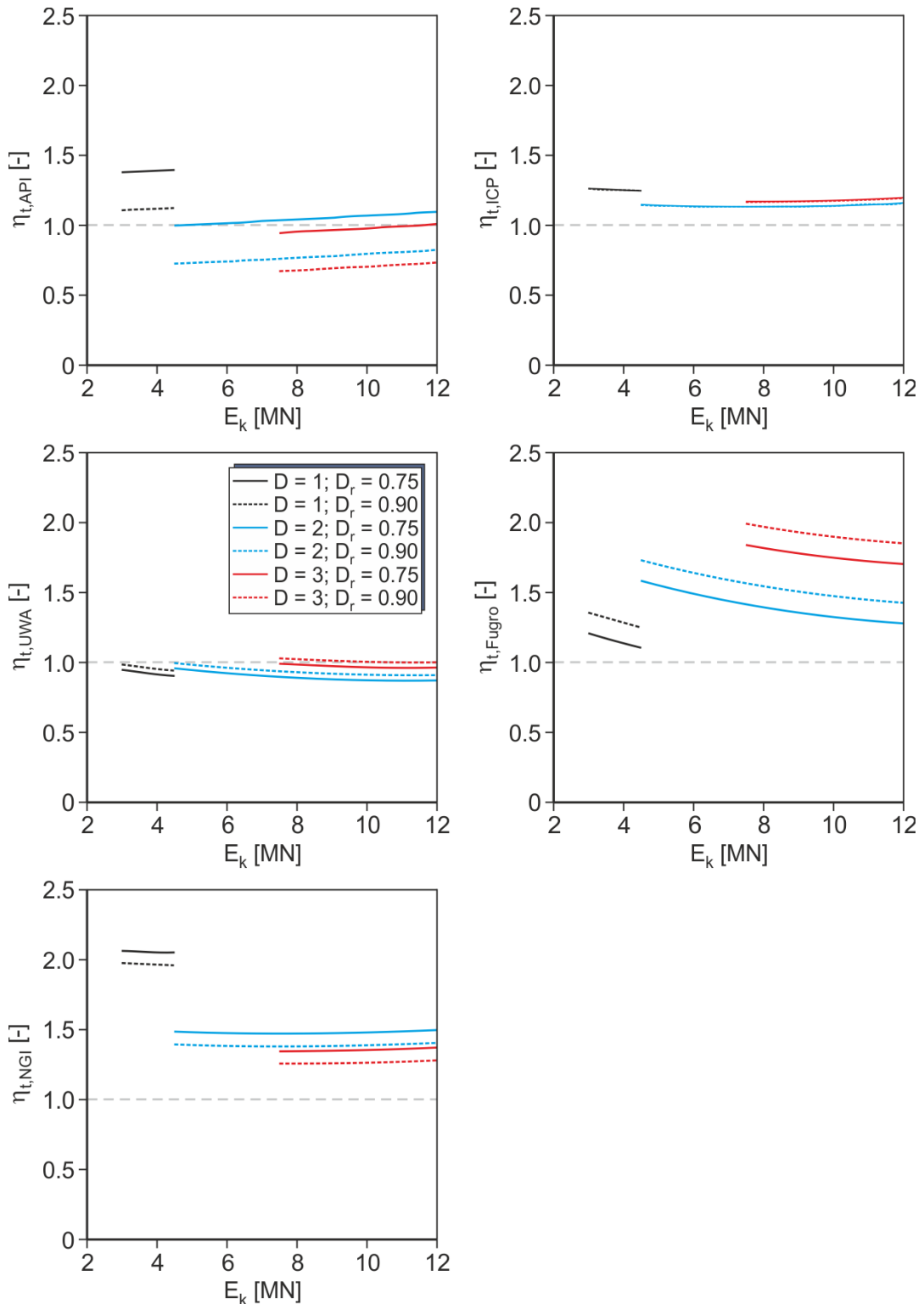


Figure 50: Overview of the quality factors for each design method, assumed density and pile diameter as a function of the load

### 3.1.4 Summary and Conclusion

In the analysis performed in WP7.4 regarding the geotechnical reliability assessment of foundation piles, typical offshore soil and foundation pile properties for offshore wind converters in the North Sea were assumed. Applying five design methods for the

determination of the axial tensile resistance, namely the API-, ICP-, UWA-, Fugro- and NGL-methods, in total 60 deterministic valid designs were evaluated within a reliability based design. By taking into account typical variability for the assumed soil condition as well as the determined model error for the investigated design methods, a reliability based determination of the failure probability in terms of the reliability index was executed. Further, a new calibration approach regarding the required GSF for the prescribed failure probability was introduced. Thereby, the results due to the reliability based calculations of all design methods were taken into account. Furthermore, quality factors were derived for each design method as function of the load, pile diameter, and soil density. On basis of these quality factors, a more sophisticated evaluation of both, the considered design method as well as the safety level in terms of the required GSF (or partial safety factor) is possible. By applying the quality factors, a more robust result within a deterministic design regarding the embedded pile length is achieved. Based on the investigated pile-soil systems and the assumed model error the calculated quality factors indicate that the UWA- and ICP-method are the most robust design methods in comparison to the other investigated offshore design methods. By applying the UWA-method, a decrease in the GSF or the resistance partial safety factor of approximately 0.94 with respect to the prescribed GSF of 2.03 should be considered, where for the ICP-method an increase of 1.17 of the GSF should be taken into account within a deterministic design.

### 3.2 Reliability of the substructure under consideration of the turbine and soil parameters

The second part of the work on reliability of piles and substructures under consideration of soil parameters in WP7.4, described in this section, concentrates on the probabilistic design of offshore substructures. However, due to the complex interaction between turbine, substructure, and foundation, it is presumed that a decoupled consideration is not sufficient for a sophisticated reliability analysis. Therefore, in this section, fully coupled aero-elastic simulations using the simulation code FASTv8 (Jonkman, 2013) are conducted taking into account the substructure, the turbine, and an adequate soil model. In this context, the consideration of the soil is regarded to be essential - although nowadays the soil-structure interaction is frequently neglected (e.g. (Jonkman, et al., 2012) or (Zwick & Muskulus, 2015)) - as soil parameters exhibit a high amount of uncertainty. Furthermore, in D72.2 of the IRPWind project, new data concerning soil-structure interaction was gained, which is in the current context.

Therefore, the general idea of this part of the project is to conduct probabilistic simulations of offshore wind turbines using a fully coupled aero-elastic model to evaluate the reliability of offshore wind turbine support structures. This approach gives a first insight in the difference of probabilistic and deterministic designs, demonstrates the potential of probabilistic simulations and creates a basis for further studies focusing on safety factor (SF) calibration. SF calibration and different designs for deterministic and probabilistic approaches (i.e. a classic and a robust optimization) are out of the scope of the current work, but can be based on the present findings.

#### 3.2.1 Introduction and concept

As stated before, probabilistic simulations for fully coupled offshore wind turbines including an adequate soil model are desired. To achieve this aim, there are several challenges to be handled. Firstly, an adequate soil model for probabilistic simulations has to be developed. Current soil models are either rudimentary (e.g. apparent fixity length (Zaaijer, 2006)) or numerically expensive (e.g. FE or p-y models (Thieken, et al., 2015)). Furthermore, state-of-the-art models, like p-y curves, do not match experimental results (Hald, et al., 2009), and therefore, have high model errors. Secondly, for many probabilistic parameters, the statistical distributions are unknown. And lastly, the fatigue damage calculation, being decisive for the substructure lifetime assessment, is very CPU intensive and exhibits high uncertainties (Zwick & Muskulus, 2015).

Therefore, in this project, the following steps are conducted to solve these problems and to enable probabilistic calculations for coupled time domain models of offshore wind turbines. The conducted steps correspond to the structure of the rest of section 3.2, which is concluded with a summary and an outlook:

- Development of a soil model that does not increase the computing time significantly, but includes operating point dependent stiffnesses and can be combined with substructural reduction schemes like the Craig-Bampton reduction (Craig Jr. & Bampton, 1968).
- Assessment of the importance of soil models for the overall turbine behavior and of the differences between various p-y models to identify those models that are adequate for coupled dynamics.
- Evaluation of various p-y models using the experimental data of WP7.2.

- Deviation of statistical distributions for important environmental conditions based on offshore measurement data (FINO project <sup>1</sup>) and literature values (e.g. (Zaaijer, 2006) or (Hansen, et al., 2015)).
- Global sensitivity analysis to identify those parameters that have to be treated probabilistically and those that can be fixed to deterministic values.
- Definition of a deterministic and a probabilistic simulation model. Here, the structural design is the same, as an independent optimization of the deterministic and the probabilistic design would be far out of the scope of this project. However, the offshore conditions (e.g. wind speeds, wave heights, etc.) differ, as they are either set deterministic values or follow statistical distributions.
- Calculation of the damage distribution (wind speed versus fatigue lifetime damage) and the uncertainty in the lifetime damage approximation. Comparison of deterministic and probabilistic damages.

### 3.2.2 Wind turbine model

In order to simulate offshore wind turbines using probabilistic methods, an adequate wind turbine model has to be used. This model has to be accurate enough for the present application. However, at the same time, the computing time has to be low enough to manage the high amount of required simulations of a probabilistic approach. Additionally, the model has to include all significant parameters that shall be varied. Therefore, this section gives a short introduction in the overall time domain model being used. Subsequently, an approach to consider soil properties in probabilistic transient simulations is proposed. This approach is based on different soil models. Finally, data of WP7.2 is used to assess the soil-structure interaction models being the basis of the proposed approach of soil consideration.

#### 3.2.2.1 Time domain model

Offshore wind turbines are highly dynamic structures with changing external loads (for example loads resulting from turbulent wind or irregular waves) even in otherwise deterministic simulations (i.e. deterministic simulations are already partly stochastic). Therefore, transient simulations are necessary to model dynamic effects accurately. This is why current standards and guidelines (e.g. (International Electrotechnical Commission, 2009)) demand holistic time domain simulations for the design and certification process of offshore wind turbines. There are several simulation codes being capable of conducting these time domain simulations, for example Bladed, FAST, and HAWC2, to mention a few. Studies showed that the results of these codes are mainly comparable ( (Jonkman, et al., 2012) , (Jonkman & Musial, 2010)). Hence, all of them can be chosen to be used as the basic simulation tool in this work package. As FAST is open source and can be adjusted and expanded easily, for example by additional soil models, it is utilized here. FAST offers up to 23 degrees of freedom (DoF) for a land based turbine, including nine for the rotor blades (three for each blade), four for rotor-teeter motion, drivetrain, generator, and yaw rotation and ten for tower bending and platform movements. This limited number of DoF reduces the computing time to an adequate level. So, FAST is capable of conducting probabilistic simulations with a great number of computations. However, the consideration of offshore substructures in the model is complicated. Substructures are normally modelled using FE methods with beam elements having thousands degrees of freedom. Therefore, a reduction method, based on the work of Craig and Bampton (Craig

---

<sup>1</sup> Research platforms in the North Sea and Baltic Sea funded under the German Federal Ministry for Economic Affairs and Energy and "Projekträger Jülich" (<http://www.fino-offshore.de/en>)

Jr. & Bampton, 1968) and called Component-Mode-Synthesis, is implemented in FAST. This reduction method allows a modal representation of the substructure with about five to 15 degrees of freedom (Damiani, et al., 2013). Nonetheless, this reduction approach has the significant shortcoming that classical soil models, based on nonlinear springs distributed along the piles, cannot be applied. Thence, in FAST the substructure is assumed clamped to the seabed. Since variations of soil parameters in probabilistic analyses can affect the overall turbine behavior significantly, a different approach of taking the soil into account has to be implemented. This approach is presented in the next section.

### 3.2.2.2 Soil model for transient calculations

Probabilistic transient wind turbine simulations need to have manageable computing times. This is why current holistic simulation tools are based on reduction schemes to limit the number of degrees of freedom used for the substructure. A classical soil model based on p-y curves and T-z curves has, firstly, too many degrees of freedom to be efficiently used, and secondly, it cannot be included in a reduction scheme like the Component-Mode-Synthesis of Craig and Bampton (Craig Jr. & Bampton, 1968). Hence, a two-step approach for an effective consideration of soil characteristics in transient simulations was developed. This approach does not add necessarily DoFs to the structural model of the substructure. It was introduced as part of this project in (Häfele, et al., 2016) and refined in (Hübler, et al., 2016) and (Hübler, et al., 2018).

In this section, a short introduction in this method is presented and the most important results are given. For more details, it is referred to (Häfele, et al., 2016), (Hübler, et al., 2016) and (Hübler, et al., 2018). As the approach can be based on different p-y and T-z soil models, some of these models are introduced as well.

To understand the present approach, firstly, the reduction scheme of FAST is explained. It is assumed that the structural assembly of the substructure was derived in the following form, for example as the result of a FE discretization:

$$\mathbf{M}\ddot{\vec{u}} + \mathbf{C}\dot{\vec{u}} + \mathbf{K}\vec{u} = \vec{F} \quad (72)$$

$\mathbf{M}$  is the mass matrix in this equation,  $\mathbf{C}$  the damping matrix,  $\mathbf{K}$  the stiffness matrix,  $\vec{u}$  the displacement vector along all degrees of freedom and  $\vec{F}$  comprises the corresponding external forces. Dots represent time derivatives.

In addition, the vector  $\vec{u}$  is partitioned into the so called vectors of boundary displacements  $\vec{u}_R$  and interior displacements  $\vec{u}_L$  in the following way:

$$\vec{u} = \begin{pmatrix} \vec{u}_R \\ \vec{u}_L \end{pmatrix} \quad (73)$$

Therefore, Eq. (72) can be written as:

$$\begin{pmatrix} \mathbf{M}_{RR} & \mathbf{M}_{RL} \\ \mathbf{M}_{LR} & \mathbf{M}_{LL} \end{pmatrix} \begin{pmatrix} \vec{u}_R \\ \vec{u}_L \end{pmatrix} + \begin{pmatrix} \mathbf{C}_{RR} & \mathbf{C}_{RL} \\ \mathbf{C}_{LR} & \mathbf{C}_{LL} \end{pmatrix} \begin{pmatrix} \dot{\vec{u}}_R \\ \dot{\vec{u}}_L \end{pmatrix} + \begin{pmatrix} \mathbf{K}_{RR} & \mathbf{K}_{RL} \\ \mathbf{K}_{LR} & \mathbf{K}_{LL} \end{pmatrix} \begin{pmatrix} \vec{u}_R \\ \vec{u}_L \end{pmatrix} = \begin{pmatrix} \vec{F}_R \\ \vec{F}_L \end{pmatrix} \quad (74)$$

If no boundary conditions are applied, the stiffness matrix  $\mathbf{K}$  is singular due to rigid body motions. This is why, in the original FAST simulation tool, boundary conditions are applied and the substructure is fixed at the seabed ( $\vec{u}_{base} = 0$ ). This means:

$$\vec{u}_R = \begin{pmatrix} \vec{u}_{int} \\ \vec{u}_{base} \end{pmatrix} \quad (75)$$

where  $\vec{u}_{int}$  is the vector of the displacements at interface nodes between tower and substructure.  $\vec{u}_{base}$  is the vector of the displacements at the bottom of the structure

(mudline). This approach is changed here, so that only the interface nodes are boundary nodes and the base nodes are part of the interior nodes:

$$\vec{u}_R = \vec{u}_{int} \quad (76)$$

and

$$\vec{u}_L = \begin{pmatrix} \vec{u}_I \\ \vec{u}_{base} \end{pmatrix}. \quad (77)$$

It follows:

$$\mathbf{M}_{LL} = \begin{pmatrix} \mathbf{M}_I & \mathbf{M}_{I,base} \\ \mathbf{M}_{base,I} & \mathbf{M}_{base} \end{pmatrix} \quad (78)$$

and

$$\mathbf{K}_{LL} = \begin{pmatrix} \mathbf{K}_I & \mathbf{K}_{I,base} \\ \mathbf{K}_{base,I} & \mathbf{K}_{base} \end{pmatrix}. \quad (79)$$

The stiffness matrix is still singular, as the boundary conditions are not applied anymore ( $\vec{u}_{base} \neq 0$ ). Hence, the matrices  $\mathbf{M}_{base}$  and  $\mathbf{K}_{base}$  containing the terms of the structural system assembly are changed according to Eqs (80) and (81) by adding  $n$  stiffness ( $\mathbf{K}_{soil,i}$ ) and mass matrices ( $\mathbf{M}_{soil,i}$ ) on the main diagonal:

$$\mathbf{M}_{base}^* = \begin{pmatrix} \mathbf{M}_{base,11} + \mathbf{M}_{soil,1} & \cdots & \mathbf{M}_{base,1n} \\ \vdots & \ddots & \vdots \\ \mathbf{M}_{base,n1} & \cdots & \mathbf{M}_{base,nn} + \mathbf{M}_{soil,n} \end{pmatrix}, \quad (80)$$

$$\mathbf{K}_{base}^* = \begin{pmatrix} \mathbf{K}_{base,11} + \mathbf{K}_{soil,1} & \cdots & \mathbf{K}_{base,1n} \\ \vdots & \ddots & \vdots \\ \mathbf{K}_{base,n1} & \cdots & \mathbf{K}_{base,nn} + \mathbf{K}_{soil,n} \end{pmatrix}. \quad (81)$$

This removes the singularity of  $\mathbf{K}$  and it follows:

$$\begin{pmatrix} \mathbf{M}_{RR} & \mathbf{M}_{RL} \\ \mathbf{M}_{LR} & \mathbf{M}_{LL}^* \end{pmatrix} \begin{pmatrix} \vec{u}_R \\ \vec{u}_L \end{pmatrix} + \begin{pmatrix} \mathbf{C}_{RR} & \mathbf{C}_{RL} \\ \mathbf{C}_{LR} & \mathbf{C}_{LL} \end{pmatrix} \begin{pmatrix} \dot{\vec{u}}_R \\ \dot{\vec{u}}_L \end{pmatrix} + \begin{pmatrix} \mathbf{K}_{RR} & \mathbf{K}_{RL} \\ \mathbf{K}_{LR} & \mathbf{K}_{LL}^* \end{pmatrix} \begin{pmatrix} \vec{u}_R \\ \vec{u}_L \end{pmatrix} = \begin{pmatrix} \vec{F}_R \\ \vec{F}_L \end{pmatrix}, \quad (82)$$

with

$$\mathbf{M}_{LL}^* = \begin{pmatrix} \mathbf{M}_I & \mathbf{M}_{I,base} \\ \mathbf{M}_{base,I} & \mathbf{M}_{base}^* \end{pmatrix} \quad (83)$$

and

$$\mathbf{K}_{LL}^* = \begin{pmatrix} \mathbf{K}_I & \mathbf{K}_{I,base} \\ \mathbf{K}_{base,I} & \mathbf{K}_{base}^* \end{pmatrix}. \quad (84)$$

Up to here, the number of degrees of freedom was not reduced and it is still the same as for the FE discretization. To reduce the size of  $\vec{u}_L$ , a Ritz transformation is applied and the number of DoFs is reduced to  $m$  generalized interior coordinates ( $\vec{q}_m$ ). As the boundary displacements  $\vec{u}_R$  are not affected by the Component-Mode-Synthesis, it follows:

$$\begin{pmatrix} \vec{u}_R \\ \vec{u}_L \end{pmatrix} = \Phi \begin{pmatrix} \vec{u}_R \\ \vec{q}_m \end{pmatrix}, \quad (85)$$

with

$$\Phi = \begin{pmatrix} \mathbf{I} & \mathbf{0} \\ \Phi_R & \Phi_L \end{pmatrix}, \quad (86)$$

where  $\Phi_R$  are the constraint modes,  $\Phi_L$  are the fixed-interface normal modes,  $\mathbf{I}$  is the identity matrix, and  $\mathbf{0}$  is the zero matrix.

The constraint modes  $\Phi_R$  can be easily calculated by using Eq. (82), when the homogenous, static case of the rigid body is considered and all boundary DoFs are set to unit displacement. Eq. (82) simplifies to:

$$\begin{pmatrix} \mathbf{K}_{RR} & \mathbf{K}_{RL} \\ \mathbf{K}_{LR} & \mathbf{K}_{LL}^* \end{pmatrix} \begin{pmatrix} \vec{1} \\ \vec{0} \end{pmatrix} = \begin{pmatrix} \vec{0} \\ \vec{0} \end{pmatrix} \quad (87)$$

and it follows:

$$\Phi_R = -\mathbf{K}_{LL}^{*-1} \mathbf{K}_{LR}. \quad (88)$$

The matrix of the fixed-interface normal modes  $\Phi_L$  comprises the first  $m$  eigenvectors of the eigenvalue problem:

$$\mathbf{K}_{LL}^* \Phi_L = \Omega_m^2 \mathbf{M}_{LL}^* \Phi_L. \quad (89)$$

With  $\Phi_m$  being the truncated subset of  $\Phi_L$  and Eq. (82), the Ritz transformation leads to:

$$\begin{pmatrix} \mathbf{M}_{BB} & \mathbf{M}_{Bm} \\ \mathbf{M}_{mB} & \mathbf{I} \end{pmatrix} \begin{pmatrix} \vec{u}_R \\ \vec{q}_m \end{pmatrix} + \begin{pmatrix} \mathbf{0} & \mathbf{0} \\ \mathbf{0} & 2\xi\Omega_m \end{pmatrix} \begin{pmatrix} \vec{u}_R \\ \vec{q}_m \end{pmatrix} + \begin{pmatrix} \mathbf{K}_{BB} & \mathbf{0} \\ \mathbf{0} & \Omega_m^2 \end{pmatrix} \begin{pmatrix} \vec{u}_R \\ \vec{q}_m \end{pmatrix} = \begin{pmatrix} \vec{F}_R + \Phi_R^T \vec{F}_L \\ \Phi_m^T \vec{F}_L \end{pmatrix}, \quad (90)$$

with

$$\mathbf{M}_{BB} = \mathbf{M}_{RR} + \mathbf{M}_{RL} \Phi_R + \Phi_R^T \mathbf{M}_{LR} + \Phi_R^T \mathbf{M}_{LL}^* \Phi_R, \quad (91)$$

$$\mathbf{M}_{mB} = \Phi_m^T \mathbf{M}_{LR} + \Phi_m^T \mathbf{M}_{LL}^* \Phi_R, \quad (92)$$

$$\mathbf{M}_{Bm} = \mathbf{M}_{mB}^T, \quad (93)$$

$$\mathbf{K}_{BB} = \mathbf{K}_{RR} + \mathbf{K}_{RL} \Phi_R \quad (94)$$

and  $\Omega_m$  being the diagonal matrix of the eigenvalues of  $\Phi_L$ .  $\xi$  is the critical viscous damping that affects the fixed-interface normal nodes.  $\mathbf{K}$  was singular, but  $\Phi^T \mathbf{K} \Phi$  is regular, because  $\det(\Omega_m^2) > 0$  and  $\det(\mathbf{K}_{BB}) > 0$ .

It can be concluded that the present approach of including the soil behavior directly in the reduced structural behavior can be very beneficial. It is very effective, as it does not add additional DoFs to the system and the computing time is not increased significantly. Furthermore, the approach is very flexible. It is not given how the mass and stiffness matrices are computed. All different kinds of soil models are possible. Some of them are presented subsequently.

However, the main disadvantage of the proposed method has to be mentioned first. Since the reduction scheme is only applied once at the beginning of a time domain simulation, the soil-structure interaction is linearized. The soil matrices are constant and cannot be changed during the simulation. This means, the matrices are not directly load depended as they are in reality. Hence, an operation point has to be chosen in advance to use soil matrices that correspond to the acting loads. Figure 51 according to (Häfele, et al., 2016) illustrates the procedure. An adequate method of choosing an operating point is presented in the following in this section.

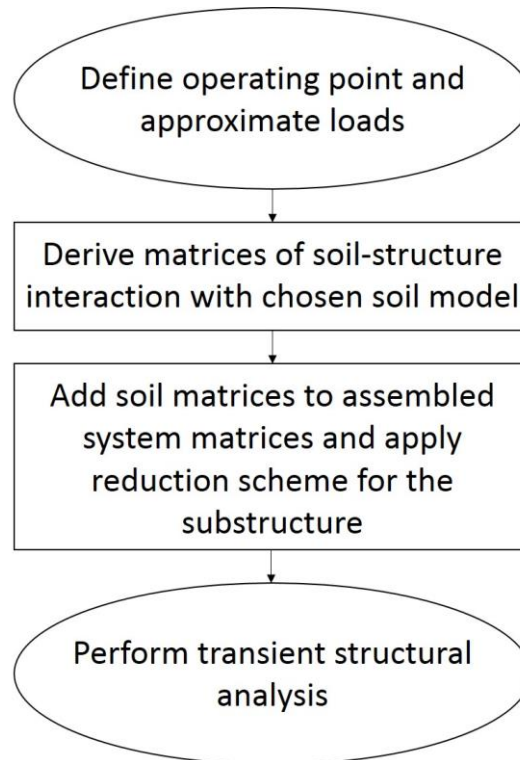


Figure 51: Scheme of proposed soil consideration according to (Häfele, et al., 2016)

A key point of the present soil consideration are the stiffness and mass matrices. It is not specified how to compute these matrices. Nevertheless, it is state of the art to use static p-y and T-z curves to determine the stiffnesses in case of pile foundations. Therefore, for the computation of the matrices, in this project, the first step is a discretization of a pile in the FE solver ANSYS using linear Timoshenko beam elements. Then, the pile is assembled with non-linear spring elements in all spatial coordinate directions along its length. Current guidelines recommend to calculate the stiffnesses for the p-y and T-z curves according to API (American Petroleum Institute, 2002). However, it was shown for instance by Achmus (Achmus, 2011), Hald et al. (Hald, et al., 2009) and Hübler et al. (Hübler, et al., 2018) that calculated stiffnesses differ significantly from experimental results. Hence, other methods to calculate spring stiffnesses were developed by Kallehave et al. (Kallehave, et al., 2012), Sørensen (Sørensen, 2012), Kirsch et al. (Kirsch, et al., 2014), and Thieken et al. (Thieken, et al., 2015), to mention a few. For the axial stiffnesses, CPT-based methods are already included in current guidelines (API, 2007). Here, the different models are only introduced briefly. A good overview and a comparison of the models can be found in (Thieken, et al., 2015). For detailed information it is referred to the original sources given above.

The most common approach of calculating the soil resistance ( $p$ ) depending on the horizontal displacement of the pile ( $y$ ) is given in the API (American Petroleum Institute, 2002):

$$p = A p_u \tanh\left(\frac{k_{ini} z}{A p_u} y\right). \quad (95)$$

Here,  $A$  is a calibration factor depending on the type of loading.  $p_u$  is the ultimate bedding resistance depending on the depth ( $z$ ).  $D$  is the pile diameter and  $\gamma'$  is the buoyant unit weight.  $k_{ini}$  is an initial stiffness coefficient being a function of the internal friction angle

( $\varphi'$ ) and  $z$ . The exact formulation and dependencies of these values can be found in the standard.

The spring stiffnesses of the linearized springs ( $k_{lat}$ ) for the FE model can be calculated using the derivative of Eq. (95) and the distance between the discrete springs ( $dz$ ):

$$k_{lat} = \frac{\partial}{\partial y} \left[ A p_u \tanh \left( \frac{k_{ini} z}{A p_u} y \right) \right] dz = \frac{k_{ini} z dz}{\cosh^2 \left( \frac{k_{ini} z}{A p_u} y \right)}. \quad (96)$$

However, as stated before, the stiffnesses calculated using this method differ remarkable from measurements. This difference is, in particular, apparent for the initial stiffness and piles with large diameters. Therefore, Wiemann et al. (Wiemann, et al., 2004) and Kallehave et al. (Kallehave, et al., 2012) proposed the following changes of the initial stiffness coefficient:

$$k_{Wiemann} = k_{ini} \left( \frac{D_{ref}}{D} \right)^{\frac{4(1-a)}{4+a}} \quad (97)$$

with the reference values  $D_{ref} = 0.61m$  and  $a = 0.5$  to  $0.6$  and

$$k_{Kallehave} = \frac{1}{z} k_{ini} z_{ref} \left( \frac{z}{z_{ref}} \right)^m \left( \frac{D}{D_{ref}} \right)^{0.5} \quad (98)$$

with  $z_{ref} = 2.5m$  and  $m = 0.6$ . The reference diameter remains unchanged ( $D_{ref} = 0.61m$ ).

The changes that are proposed by Sørensen (Sørensen, 2012) and (Sørensen, et al., 2010)) do not focus on the initial stiffnesses, but on errors occurring under ultimate loads. He formulates in (Sørensen, 2012) without using the original value of the initial stiffness coefficient ( $k_{ini}$ ):

$$k_{Sørensen} = \frac{1}{z} a \left( \frac{z}{z_{ref}} \right)^b \left( \frac{D}{D_{ref}} \right)^c \left( \frac{E_s}{E_{s,ref}} \right)^d. \quad (99)$$

Here,  $a = 1MPa$  is a reference stiffness. For the dimensionless coefficients, the following values are recommended:  $b = 0.3$ ,  $c = 0.5$ , and  $d = 0.8$ . For the reference values  $z_{ref} = 1m$ ,  $D_{ref} = 1m$ , and  $E_{s,ref} = 1MPa$  are proposed.  $E_s$  is the static soil stiffness modulus. Kirsch et al. (Kirsch, et al., 2014) give a formulation that takes into account the underestimation of the initial soil stiffness and the overestimation for ultimate loads. So, firstly, a reduced internal friction angle  $\varphi'_{red} = \varphi' - 0.5(D - 2)$  is introduced. Secondly, the initial stiffness coefficient  $k_{red} = f(\varphi'_{red})$  is calculated. Based on this, the following expression with  $E_{sd}$  being the dynamic soil stiffness modulus is suggested:

$$k_{Kirsch} = k_{red} \left[ 1 + \left( 1 - \frac{p}{p_u} \right) \left( \frac{E_{sd}}{E_s} - 1 \right) \right]. \quad (100)$$

In (Thieken, et al., 2015), Thieken et al. developed a significantly different p-y model. It is based on completely new “basic p-y curves” taking both, the underestimation for small loads and the overestimation of the soil stiffness for high loads, into account. Subsequently, the “basic p-y curves” are iteratively changed to take the interaction of the deflection line with the bedding resistance into account and to consider the pile tip effect. For details it is referred to (Thieken, et al., 2015).

So far, only p-y models were presented. These models are important for the horizontal stiffness. T-z curves are used for the vertical stiffness of the soil. Here, a classical approach is presented in (American Petroleum Institute, 2002). It defines an unit end bearing capacity ( $q$ ) and a shaft friction ( $f$ ) that can be used to calculate the spring

stiffnesses for the spring at the end of the pile ( $k_q$ ) and for springs parallel to the whole pile ( $k_{ax}$ ), respectively. Both spring stiffnesses depend on the mobilized axial displacement. In (American Petroleum Institute, 2002) the following recommendations are given:

$$q = \min(q_{max}, p' N_q) \quad (101)$$

and

$$f = \min(f_{max}, K p_0 \tan(\delta)). \quad (102)$$

Here,  $q_{max}$  is the limit unit end bearing capacity given in the standard for different soil densities. The same applies for the limit skin friction ( $f_{max}$ ), the dimensionless bearing capacity factor ( $N_q$ ), and the soil pile friction angle ( $\delta$ ).  $p'$  is the effective overburden pressure at a given depth and  $K$  is the coefficient of lateral pressure. This approach is slightly changed in newer standards (API, 2007) and other methods of calculating the shaft friction and the unit end bearing capacity are introduced. These methods (ICP, UWA, FURGO and NGL) are mainly based on cone penetration tests (CPTs). For the unit skin friction, the general equation (103) is proposed. Values for the constants  $a$  to  $e$ ,  $u$  and  $v$  are given in the standard for different approaches.

$$f = u q_{c,z} \left( \frac{\sigma'_{v0}}{p_a} \right)^a A_r^b \left[ \max\left(v, \frac{L-z}{D}\right) \right]^{-c} (\tan(\delta_{cv}))^d \left[ \min\left(1, \frac{L-z}{D} \frac{1}{v}\right) \right]^e. \quad (103)$$

$q_{c,z}$  is the CPT cone tip resistance at depth  $z$ .  $\sigma'_{v0}$  is the soil effective vertical in-situ stress at depth  $z$ . The atmospheric pressure is  $p_a$ .  $A_r$  is defined as the pile displacement ratio  $A_r = 1 - \left(\frac{D_i}{D_o}\right)^2$  using the inner and outer pile diameter ( $D_i$  and  $D_o$ ). The embedded length is  $L$  and  $\delta_{cv}$  is the pile-soil constant volume interface friction angle.

For the unit end bearing capacity, different approaches, all based on the average value of  $q_{c,z}$  between  $1.5 D_o$  above the pile tip to  $1.5 D_o$  below pile tip level ( $q_{c,av,1.5D}$ ), are given in the standard. The concept of FURGO-05 is given as an example. Details can be found in (API, 2007).

$$q_{FURGO} = 8.5 p_a \left( \frac{q_{c,av,1.5D}}{p_a} \right)^{0.5} A_r^{0.25}. \quad (104)$$

Summarizing the soil models: Many different soil models based on p-y and T-z curves exist for the lateral and the axial stiffnesses of the soil. All these models can be used to calculate the needed spring stiffnesses for the FE-model of the pile. For a chosen operating point, the FE model can be linearized, and subsequently, it can be reduced to a single mass and stiffness matrix using a Guyan reduction (Guyan, 2065). The computed matrices have the following symmetric form, as axial and lateral behavior are uncoupled and dissipation is neglected:

$$\mathbf{K}_{soil,pile} = \begin{pmatrix} k_{xx} & 0 & 0 & 0 & -k_{x\theta} & 0 \\ 0 & k_{yy} & 0 & k_{y\phi} & 0 & 0 \\ 0 & 0 & k_{zz} & 0 & 0 & 0 \\ 0 & k_{y\phi} & 0 & k_{\phi\phi} & 0 & 0 \\ -k_{x\theta} & 0 & 0 & 0 & k_{\theta\theta} & 0 \\ 0 & 0 & 0 & 0 & 0 & k_{\psi\psi} \end{pmatrix}. \quad (105)$$

These stiffness and mass matrices can be used in the reduction scheme of FAST to include soil characteristics in transient simulations as proposed.

As stated before, the proposed method is very flexible. Not only soil models based on different p-y and T-z curves in combination with an FE model of the pile can be used to calculate the matrices. Different approaches to generate the matrices needed could be experimental investigations or a full FE model of the pile and the surrounding soil. The FE approach is used as part of the IRPWind project in (Hübler, et al., 2016) to calculate soil matrices for a suction bucket foundation. In this case, the form of the matrices changes. Furthermore the matrices become non-symmetrical. Both does not influence the implementation in the reduction scheme.

$$\mathbf{K}_{soil,bucket} = \begin{pmatrix} k_{xx} & 0 & k_{yx} & 0 & -k_{x\theta} & 0 \\ 0 & k_{yy} & k_{yz} & k_{y\phi} & 0 & 0 \\ k_{zx} & k_{zy} & k_{zz} & -k_{z\phi} & -k_{z\theta} & 0 \\ 0 & k_{y\phi} & -k_{\phi z} & k_{\phi\phi} & 0 & 0 \\ -k_{x\theta} & 0 & -k_{\theta z} & 0 & k_{\theta\theta} & 0 \\ 0 & 0 & 0 & 0 & 0 & k_{\psi\psi} \end{pmatrix}. \quad (106)$$

In Figure 51, the first step is the choice of an operating point. This choice influences the soil stiffness, and therefore, it affects the results of time domain simulations of the whole wind turbine. The challenge is to develop an effective way to determine the stiffnesses for a given operating point. An approach linking environmental conditions with the loads at mudline, being decisive for the soil stiffness, is proposed in (Hübler, et al., 2018) and is summarized here.

Firstly, it has to be defined what is meant in terms of environmental conditions in the present case. Wind speeds and wave heights have a major influence on the acting loads. Therefore, these two parameters are related to environmental conditions. However, for non-rotationally symmetric substructures (like jackets), the direction of the wind and the waves is at least similarly important. That is why, for non-rotationally symmetric substructures, the direction is a third condition parameter. It is assumed that wind and wave act in the same direction, as it is recommended by current standards (International Electrotechnical Commission, 2009). Other environmental conditions are considered to be less significant. Therefore, they are neglected to simplify the approach.

Secondly, the loads being decisive for the soil stiffness have to be defined. The overturning moment and the horizontal shear force at mudline are important for the lateral stiffness. The vertical force determines the axial stiffness. All loads vary periodically. Therefore, for the operating points a representative value has to be chosen. In this case, the maximum values of the loads are selected. This is a simplification that has to be performed due to unmanageable time-variant stiffnesses. The selection of maximum values is supposed to be conservative, as it leads to minimum stiffnesses.

Thirdly, a correlation between the environmental conditions and the loads of interest has to be identified. Time domain simulations of the whole turbine for wind speeds between  $v_{wind} = 0 \text{ m/s}$  and  $v_{wind} = 40 \text{ m/s}$ , for wave heights between  $h_s = 0 \text{ m}$  and  $h_s = 14 \text{ m}$ , and wind and wave directions between  $\alpha = -45^\circ$  and  $\alpha = 45^\circ$  are computed. The relevant results of these simulations are the loads at mudline for the given, varying environmental conditions.

The simulation results are used as sampling or data points for response surfaces. The challenge is to define functions that can be fitted to the data points using a least square algorithm. Polynomial approaches can be applied, if the data space is divided into several subsections (c.f. Figure 52). The subsection highly depend on the turbine controller. Therefore, here, the data space is divided into three subsections depending on the wind

speed that correlates with the controller actions. In the first section (below rated wind speed), the blade-pitch controller is inactive. After reaching the rated speed, it starts to pitch the blades (section 2). After having reached the cut-off wind speed (third section), the blades are pitched out completely (pitch angle of  $90^\circ$ ) and the turbine is shut down. The non-linear behavior and the importance of the piecewise definition is clarified in Figure 52 according to (Hübler, et al., 2016).

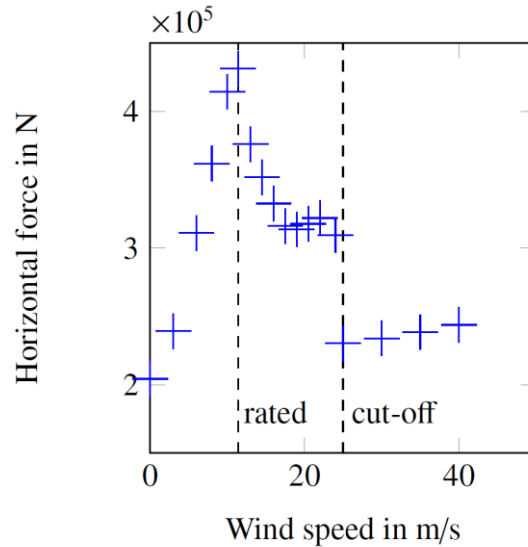


Figure 52: Illustration of the full data space for the response surface according to (Hübler, et al., 2016)

On the basis of this segmentation, polynomials of a degree one to three are fitted in all three dimensions (wind speed, wave height, and direction). The coefficients of the polynomials are calculated using a linear regression for each subsection and force. Without losing significant accuracy, the degree of the polynomials is chosen as low as possible. Figure 52 shows, for example, that above cut-off a polynomial degree of one might be sufficient. An example of a two-dimensional response surface (wind speed and wave height) is given in Figure 53.

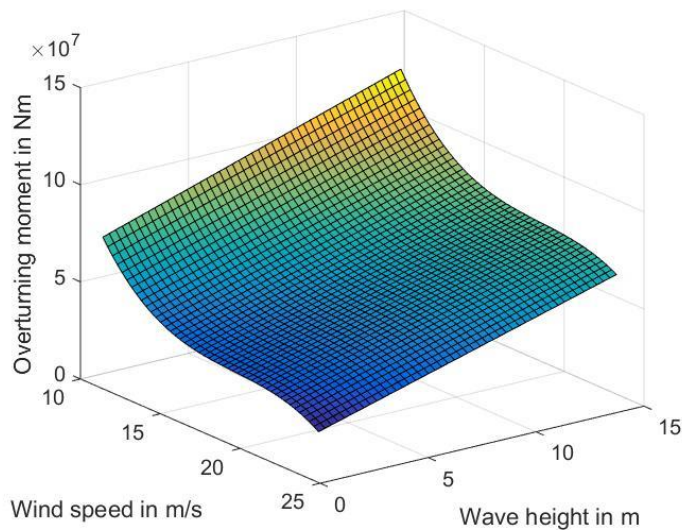


Figure 53: Response surface for an OC3 Monopile

The presented approach of linking the loads with the most important environmental conditions using multi-dimensional, piecewise polynomial response surfaces enables an estimation of the loads at the mudline. Surely, several simplifications are applied and it is only a rough approximation. Nonetheless, the determination of the soil stiffness for a given operating point using this response surface method is adequate, as the sensitivity of the soil stiffness to the loads is neither that high nor is its impact on the overall simulation that decisive. In (Hübler, et al., 2018), it is shown that this rough approximation is sufficient.

For specific and detailed results, it is referred to the underlying literature ( (Häfele, et al., 2016) , (Hübler, et al., 2016) and (Hübler, et al., 2018)). Only some general results are presented here to give an overview. Furthermore, some results focusing on the different soil models are given, as these results are relevant for the investigations in the next section.

Figure 54, according to (Häfele, et al., 2016), shows a power spectral density of the reaction force of a jacket substructure. Three different approaches for the soil-structure interaction are applied. Firstly, the structure is clamped to the seabed (standard approach in FAST). Secondly, an apparent fixity length approach according to (Zaaijer, 2006) is used. This means that the substructure is still clamped, but to a position below the mudline. This gives the substructure an additional flexibility that approximates the real soil flexibility. Thirdly, the new approach is used. The stiffness matrices are computed according to (API, 2007) with initial stiffnesses. It becomes apparent that the dynamic behavior is fundamentally changed, as the second bending eigenfrequency is shifted from about 1.2Hz to about 0.8Hz, which is more than 30%. This shift results in different loads especially for fatigue. Therefore, even the current simplified approach of considering a linearized soil behavior can lead to significantly more realistic results.

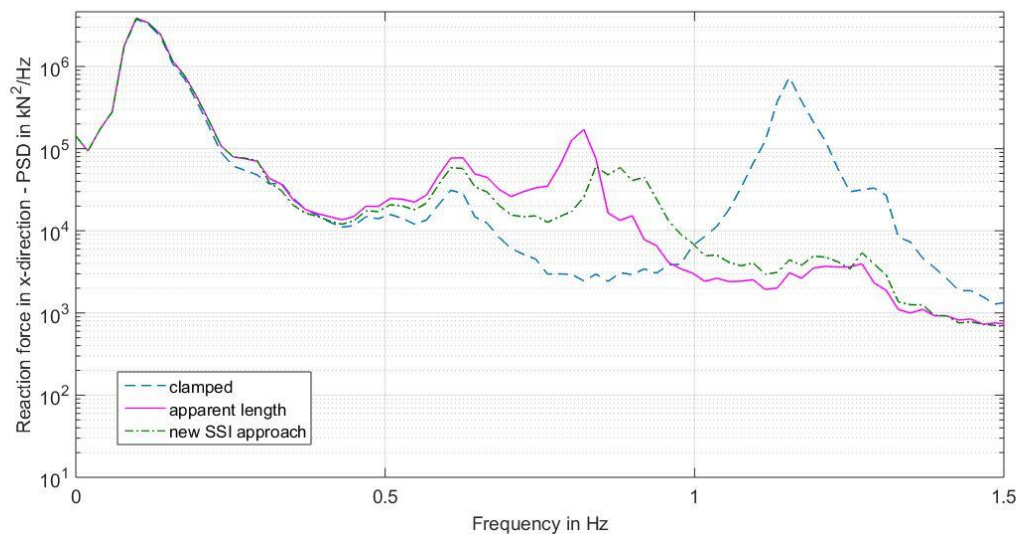


Figure 54: PSD of the OC4-jacket shear force at mudline (cf. (Häfele, et al., 2016))

Concerning the soil models, being used to compute stiffness matrices, Figure 55 and Figure 56 show PSDs with different models being used. For all simulations, the operating point is at rated wind speed. Figure 55 shows the PSDs for different axial models and Figure 56 for lateral models. It becomes clear that the influence of axial models is quite small. Hence, a neglect of the effect of different axial soil models for the dynamic behavior is an acceptable approximation. This does not mean that the axial soil behavior can be totally neglected. Only the differences between the models are not significant for the dynamic behavior. For static considerations, like the calculation of maximum bearing capacities, this is definitely not the case, as shown in Section 3.1. Lateral soil models have significant influence. A difference of nearly 10% in the second bending eigenfrequency between the different models arises. Thence, it is crucial to select soil model carefully. For a well-founded selection of soil models, it has to be investigated, which numerical model fits experimental data best. That is why, in the next section, an analysis of the soil models, based on the experiments in WP7.2 of the IRPWind project (Deliverable D72.2), is presented. The analysis is not meant to be a detailed investigation of soil behavior. The dynamic tests were not the main objective of the experiments in WP7.2. However, the conducted dynamic experiments can help to get an idea of the quality of the soil models with a special focus on dynamic behavior.

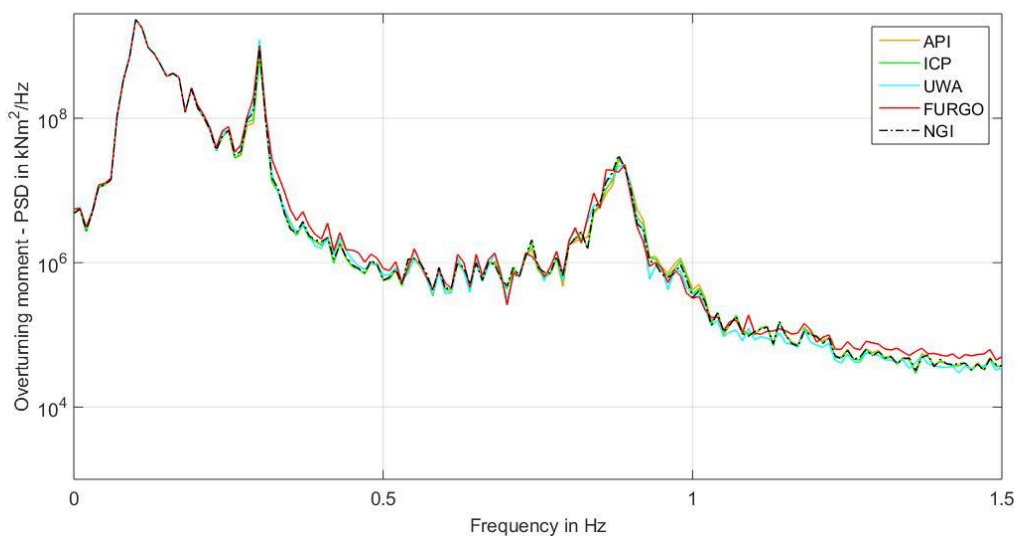


Figure 55: PSD for the OC4-jacket with different axial soil model (cf. (Hübler, et al., 2018))

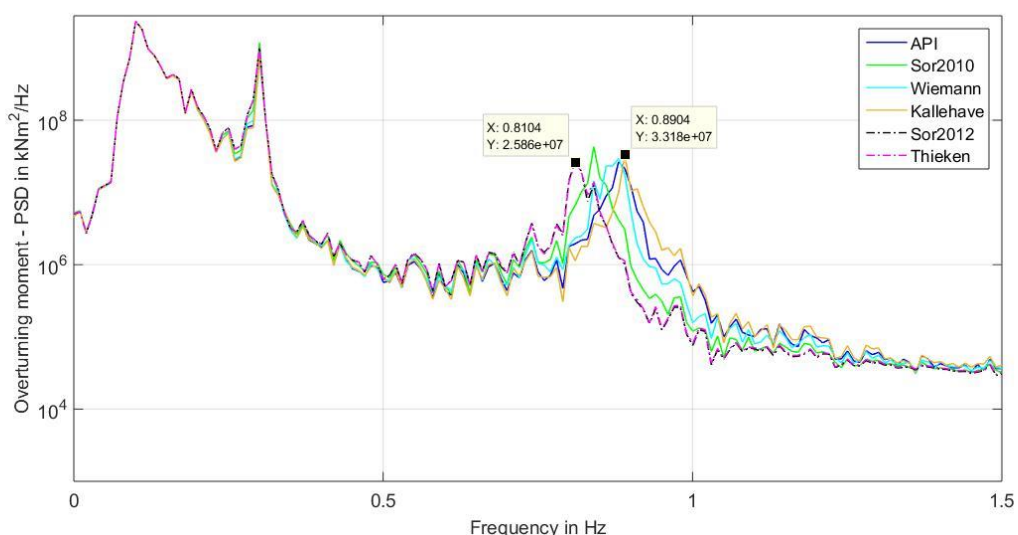


Figure 56: PSD for the OC4-jacket with different lateral soil models (cf. (Hübler, et al., 2016))

### 3.2.2.3 Assessment of basic soil models with data from WP7.2

The general objective of the geotechnical experiments with model structures on a large scale in WP7.2 of the IRPWind project is to support probabilistic calculations and the evaluation of the reliability of offshore wind turbine support structures and their foundations performed in this WP. Here, the focus is on the evaluation of the maximum static bearing capacity of mainly axially loaded piles. This work is described in Section 3.1. Furthermore, a probabilistic model for maximum static bearing capacities was developed in WP7.2 on the basis of the experimental data. This work is part of the already published deliverable D72.2 on the “Report on geotechnical tests with model structures” (cf. Section 2.3 in D72.2). A detailed description of all tests and the data gained is given in D72.2 as well. However, some additional experiments, focusing on the dynamic behavior of the pile-

soil combination, were conducted as well. These tests are designed to examine eigenfrequencies, mode shapes and damping ratios of the pile-soil combination. The results are compared to FE results being computed using the different p-y and T-z models introduced in the previous section. This is supposed to enable a more profound evaluation of the soil models used.

The tests are described briefly in this section. Subsequently, a concise summary of the analysis methods is given. The results of the analysis are presented and compared to results of FE calculations using different soil models. For further information, it is referred to (Hübler, et al., 2018). Finally, the analysis itself, but also the soil models are evaluated based on the present results.

A detailed description of the dynamic tests is given in deliverable D72.2. Here, only a short overview is given. The dynamic tests concentrate on the dynamic behavior of the piles at different embedded lengths and examine eigenfrequencies, mode shapes, and the damping of the soil-pile combination. Six piles were tested during, in between, and after the installation process. Piles 1, 3, and 4 had sensors only above the soil, whereas piles 2, 5 and 6 had sensors below the surface as well. For piles 2 and 5, there were only strain gauges below the surface. Pile 6 had low sensitive accelerometers in addition. Above the ground, all six piles were equipped with four high sensitive triaxial accelerometers. These accelerometers had to be detached during the ramming itself.

The measurements with these accelerometers took place during installation breaks and after the pile installation. To measure in between, the ramming process was stopped every 1m and dynamic tests were performed. The tests consisted of several excitations with an impact hammer in all three directions and at different heights.

For piles 2, 5, and 6, measurements during the ramming and below the surface were possible using the strain gauges and the low sensitive accelerometers. These measurements have the advantage of a much higher energy input into the pile due to the ramming. Furthermore, measurements along the whole pile and not only at positions above the ground were possible. The disadvantages of measurements during the ramming are a less clearly defined and uniaxial excitation. The excitation force was neither constant, nor measured and the precise value of the embedded length was not known, as it changes during the ramming process. Furthermore and even more important, the dynamic behavior is disturbed by the hammer on top of the pile.

For the analysis of modal properties of structures using measurement data, there are many different approaches. Rudimentary approaches, like the fast Fourier transform (FFT) or power spectral densities (PSDs) that are combined with visual peak picking for the eigenfrequencies or taking the natural logarithms of the ratio of any two successive amplitudes for the logarithmic decrement (damping), can neither be automatized nor are they very accurate. Even quite common methods of the system identification, like the frequency domain decomposition (FDD) that is based on PSDs and peak picking, cannot be automatized. Therefore, system identification through data driven stochastic subspace identification (SSI), firstly introduced by Van Overschee and de Moor (VanOverschee & DeMoor, 1991), is conducted here. This method is based on output-only measurement data and fits the data without using a physical model like FE or multi-body models. The automation of the system identification is done using triangulation-based extraction of model parameters (TEMP) based on the work of Häckell (Häckel & Rolfes, 2013). The SSI in combination with the TEMP method identifies automatically eigenfrequencies, mode shapes, and damping ratios of the piles at different embedded lengths for all piles.

After this short introduction to the experiments and methods used for the analysis, results of the experiments are presented. As the dynamic behavior of the pile is different for the two types of excitation (ramming and impact hammer), the results are presented separately. At first the impact hammer results are discussed.

The impact hammer tests were conducted for all six piles at different embedded lengths. Using SSI, it is possible to detect three main eigenfrequencies being present for nearly all tests. These eigenfrequencies can be associated to the first and second bending dominating modes and a dominating radial or “breathing” mode of the cross section area of the pile. All other eigenfrequencies are either quite high and not of interest, or not stable and not detectable for all tests. Therefore, these three mode shapes are further analyzed. Figure 57 and Figure 58 show the mode shapes of the bending dominating modes (from now on called “first” and “second bending” modes) exemplarily for pile 5 with an embedded length of 3.7m. The radial mode shape cannot be pictured properly using the measurement data. Only one accelerometer at each height was attached to the piles and the mode shape affects mainly the cross section area. Still, to illustrate the mode shape, Figure 59 shows an FE calculation of this radial mode shape.

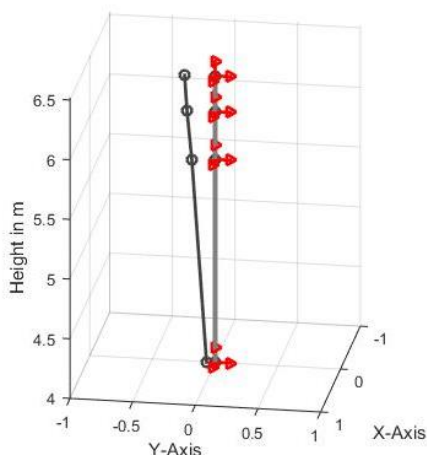


Figure 57: First bending mode of pile 5 with 3.7m embedded length ( $f=18.5\text{Hz}$ )

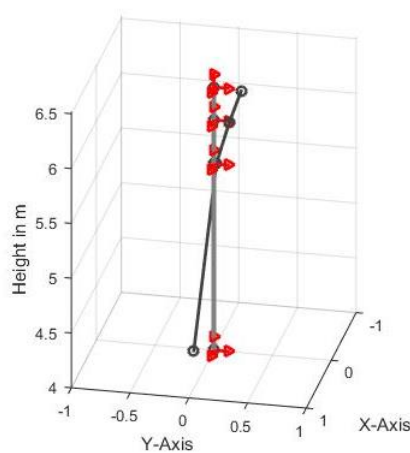


Figure 58: Second bending mode of pile 5 with 3.7m embedded length ( $f=151\text{Hz}$ )

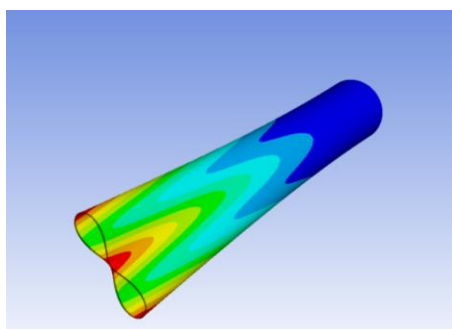


Figure 59: FE-calculation of the dominating radial or “breathing” mode at the end of the pile; cross section deformation ( $f=139\text{Hz}$ )

It is obvious that the embedded length influences the natural frequencies and the damping of the pile-soil combination. The effect of the embedded length is shown in Figure 60 and Figure 61. Here  $d_1$  and  $d_2$  are the two different diameters of the piles.

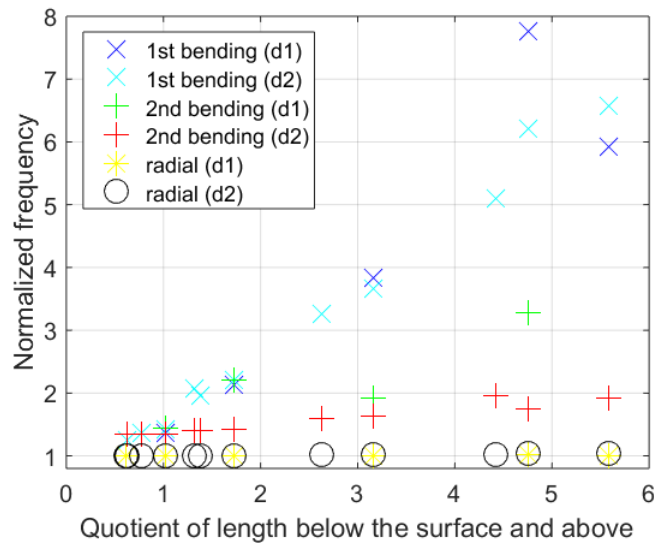


Figure 60: Normalized frequency depending on the embedded length

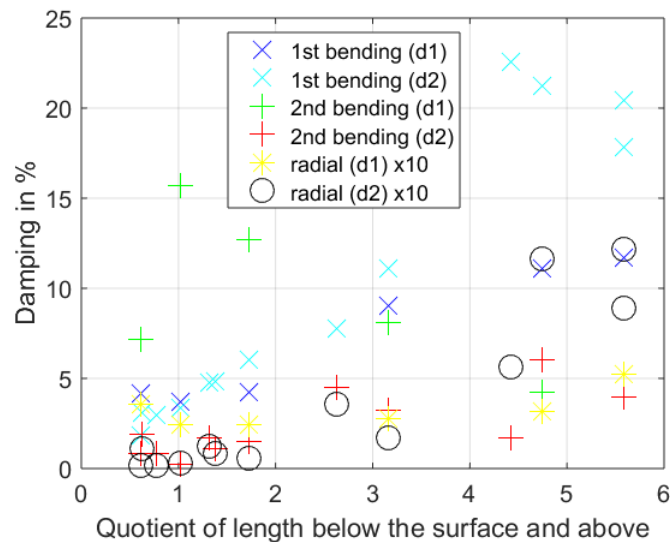


Figure 61: Damping depending on the embedded length and the mode shape

The frequencies of the bending modes are increasing along with the embedded length. This is plausible, as the pile is supported by the surrounding soil and less of it can freely vibrate. However, for the radial mode, this effect is nearly not apparent. This can be explained using Figure 59. The radial mode shape only affects the top of the pile. Hence, the end of the pile being below the surface does not influence this mode shape.

The damping ratios are more interesting, as the results are not obvious in advance. Clearly, it can be assumed that a higher embedded length will increase damping. This will be the case, since an increasing embedded length leads to more interaction between pile and soil and more energy can be dissipated through the soil (geometrical damping). So, the increase in damping ratios of the first bending mode, shown in Figure 61, is as expected. However, for the second bending mode, the experiments show a different behavior. Here, no definite trend is apparent. Generally, it can be stated that there are some lengths with higher damping ratios and some with lower ones. Probably, a change in the form of the mode shape leads to this outcome. As the embedded length increases, the zero crossing point (point of no deflection) changes. This can lead to less soil-structure

interaction at higher embedded lengths, and therefore, to smaller damping ratios (material damping in the soil). For the radial mode shape, firstly, it has to be pointed out that the damping values are multiplied by a factor of ten in Figure 61. This is done for reasons of clear illustration. Having that in mind, the damping for this mode shape is very small. Again, this can be explained by the appearance of this mode shape in the uppermost section of the pile. That is why there is nearly no interaction with the soil. Mainly material damping of the pile itself occurs, which is much lower than geometrical or material damping of the soil. Overall, the results of the damping have to be considered with care. Damping data is, as it is quite common, scattering a lot. However, since fairly high number of measurements was conducted, the results are still valid.

For the second part of the experiments, the dynamic behavior of the pile-soil combination during the ramming process is analyzed. These experiments had the advantage of a much higher energy input and of continuous measurements. On the downside, the excitation was only in axial direction and the hammer on top of the pile is disturbing the dynamic behavior of the pile. The data is analyzed using SSI and the TEMP method. Two mode shapes are detected without doubt. This is again the radial mode and additionally the first axial mode. The first bending mode is partly recognizable. Eigenfrequencies and damping ratios over all hammer blows or embedded lengths are shown, exemplarily for pile 6, in Figure 62 and Figure 63, respectively. Here, only the results of the strain gauges are presented. The data of the 2000g accelerometers is comparable, but there are some issues concerning the low sensitivities. For the eigenfrequencies, the high scattering becomes apparent. Especially for the axial mode, there are high deviation. This is because of low sensitivities in combination with high damping ratios and not totally free decay processes (the hammer excitations are quite close to each other). Still, it can be recognized that the frequency increases while the pile is driven into the soil. There are some outliers at about 2.9m and 4m. It is assumed that these outliers are a result of the ramming itself or of interaction effects of the hammer with the pile, since they disappear after having stopped the ramming at 3m and 4.1m. It might be also possible that these outliers are due to mode switches (i.e. another mode was detected). However, as there are no other pronounced modes, this reason is fairly unlikely. The first bending mode can only be detected in some cases. However, there is the same trend of higher frequencies for higher embedded lengths. The results of the radial mode support the results achieved by the impact hammer tests. There is nearly no change in the eigenfrequency over all embedded lengths. For the damping ratios in Figure 63, firstly, it has to be explained why there are such different, but stable results for different embedded lengths. Again, this can be traced back to different ramming cycles. The ramming was stopped at 0.7m, 1.5m, 3m, 4.1m, 5m, 6m, and at the end at 6.7m. These values correspond quite well to the different sections that can be seen in Figure 63 for the axial mode. Therefore, these differences are not of predominating relevance for the pile behavior itself. They only demonstrate how problematic the measurements during the ramming with hammer on top of the pile are. More important are the high damping ratios and changes in the damping. Firstly, the axial mode is heavily damped. This is the reason why it cannot be detected by impact hammer tests. Secondly, all mode shapes experience nearly constant damping ratios (or at least no trends are recognizable). This result does not agree with the previous results and cannot be explained so far. Higher embedded lengths should result in more soil-pile interaction, and therefore, in more damping. That is why this phenomena has to be further investigated in following studies. An interaction effect with the hammer on top of the pile has to be analyzed.

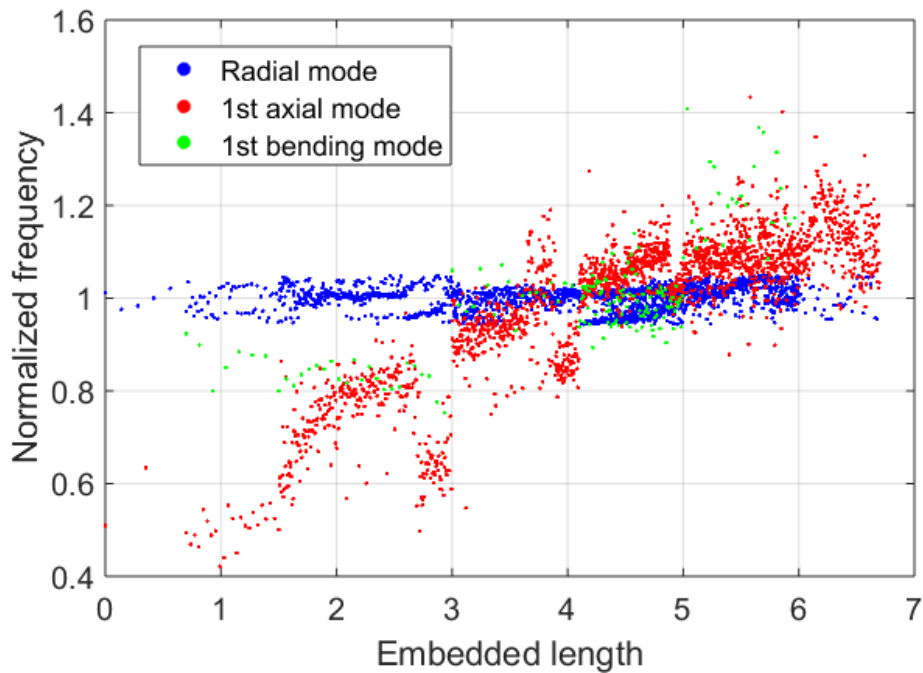


Figure 62: Normalized frequencies of pile 6 during the ramming process

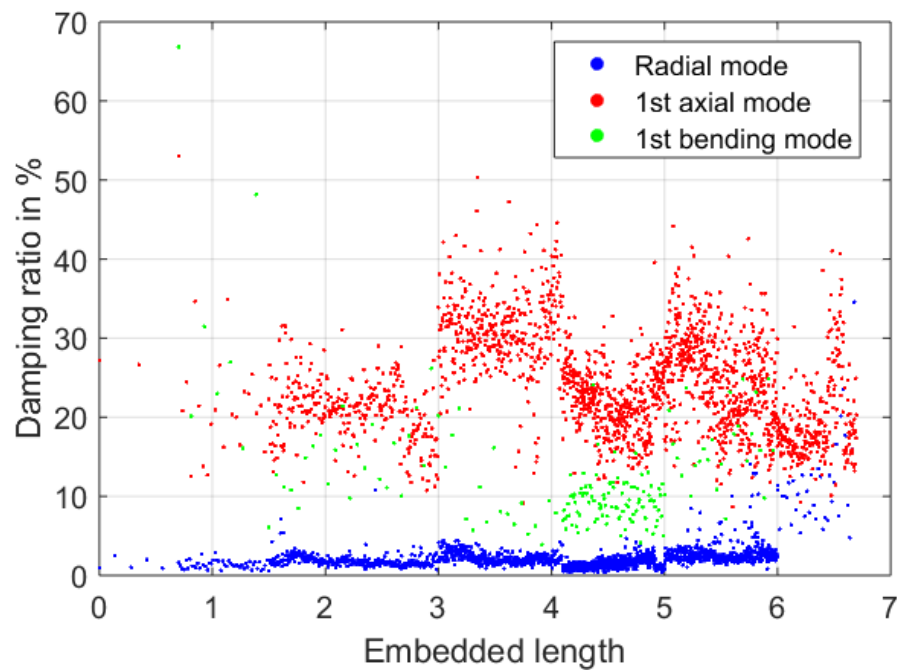


Figure 63: Damping ratios of pile 6 during the ramming process

P-y and T-z based soil models are used in this report to calculate the needed soil matrices. To conclude this section on soil models, the just presented results of the dynamic tests in WP7.2 are compared to results of FE simulations. Here, the focus is on the dynamic behavior. Only the experiments with impact hammer excitations are taken into account. For the tests during the ramming, the precise embedded lengths are not known, and therefore, comparisons would be less accurate. Furthermore, the load level during the ramming is unknown. As the soil stiffness depends on the load level, numerical

calculations would only be rough estimates. For the FE calculations, the piles are modelled as linear Timoshenko beam elements, and the surrounding soil is represented by springs in all spatial coordinate directions along the embedded length of the pile. The spring stiffnesses are based on the different soil models. The FE model is the same as in section 3.2.2.2 for the deviation of the soil matrices and as in (Hübler, et al., 2018). Computed eigenfrequencies of the FE calculations are compared to the experimental results. This is done for different embedded lengths. A consideration of damping ratios is not part of this analysis, as the utilized soil models do not include damping. Furthermore, radial modes are neglected, since beam elements are not capable of computing them. Excitations with the impact hammer during the experiments do not lead to significant displacements of the pile in the soil. Hence, it is only a marginal simplification if small loads, and therefore, initial soil conditions are assumed.

To evaluate the different soil models, measured and calculated bending eigenfrequencies are compared. Figure 64 and Figure 65 show the normalized first bending frequency of the piles with the larger and smaller diameter for different embedded lengths respectively. The frequencies are normalized with the experimental values. It becomes clear that the results of the soil models significantly differ and mostly do not fit the experiments. The standard model of the API predicts frequencies that are about 10% too low. The approaches of Sørensen (Sørensen, et al., 2010), (Sørensen, 2012)) show even higher deviations. This can be explained by the purpose of these approaches. They focus on extreme loads, but in these experiments only small loads were applied. Wiemann et al. (Wiemann, et al., 2004) concentrate on extreme loads as well. However, their approach focuses on piles with large diameters and uses a reference diameter of  $D_{ref} = 0.61m$ . As the piles in the present experiments are of about the same diameter, the changes compared to the API model are marginal. The model of Kallehave et al. (Kallehave, et al., 2012) fits the experiments the best. For this approach, the focus is on initial conditions as they are present here. However, in some cases, even this model shows differences of about 25%. Thieken et al. (Thieken, et al., 2015) try to cover initial and ultimate conditions with their new approach. However, it is clear that for initial conditions the eigenfrequencies are massively overestimated. It has to be mentioned that the approach of Thieken et al. is much more sensitive to varying loads. Therefore, for this approach, it might be a significant simplification to assume initial conditions, as the hammer excitations still introduce some loads, though these loads are fairly small. However, for loads greater than zero the soil becomes significantly softer for this approach, and therefore, the calculated eigenfrequencies – being to high so far - are getting closer to the measured ones. For all other approaches, the effect of the non-zero loads, if present, is leading to greater differences compared to the experimental results, as the predicted eigenfrequencies are already too small. However, as neither the loads at mudline nor the displacements were measured a quantitative assessment of this effect is not possible.

For the second bending mode, the identification is not that clear. Therefore, it is abstained from judging the soil models on this basis as well. However, for the second bending mode, the numerical calculations fit the experiments even worse, and the errors are changing for different embedded lengths, which is not the case for the first bending mode. For the sake of completeness, the normalized second bending eigenfrequencies for piles with smaller diameters are displayed in Figure 66.

After all, the comparisons of experiments and numerical models show that none of these soil models can really predict the dynamic behavior of the piles, as deviations of up to

25% for the best model occur. It has to be pointed out that all investigated p-y curves were initially developed for static loads. Still, currently, they are used in dynamic wind turbine applications. This fact explains, at least partly, the deviations between the numerical and experimental results. However, if models are chosen carefully according to their intended load conditions, model errors can be reduced. Models that focus on initial conditions can deliver the best results for these conditions. Whether models that focus on ultimate loads are best suitable for high load conditions or not, cannot be investigated using the present data, but it would be valuable to investigate it.

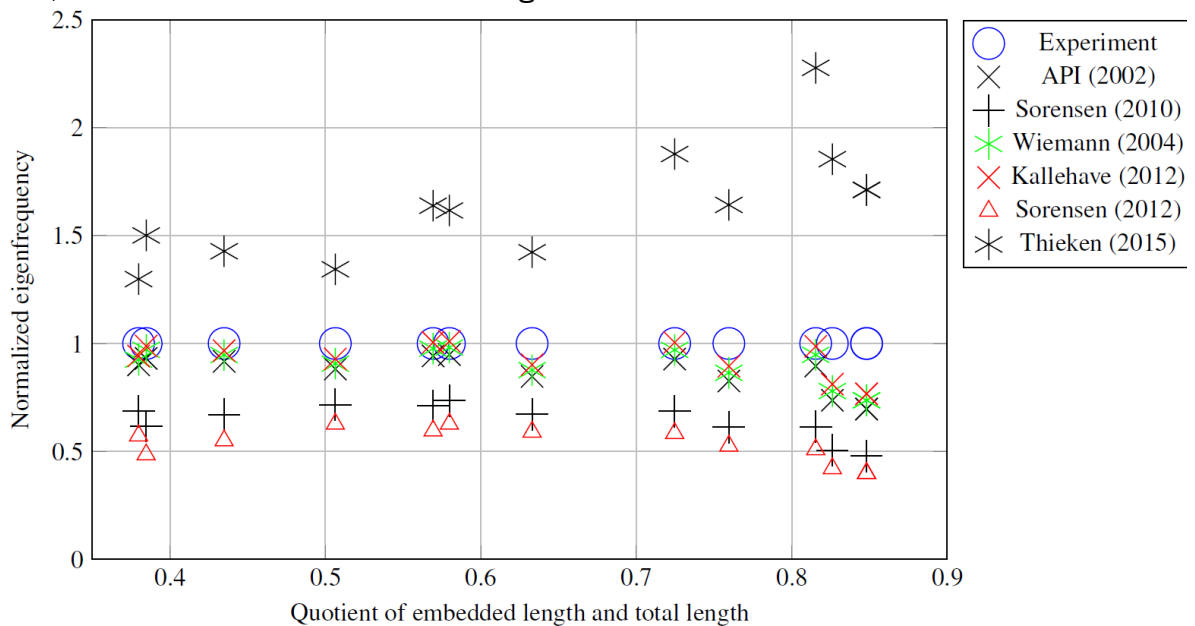


Figure 64: Normalized first bending eigenfrequencies of the piles with larger diameter for different embedded lengths calculated using different soil models

### 3.2.3 Statistical distributions of input parameters

Section 3.2.2 focuses on a time domain model of an offshore wind turbine including an adequate soil model. This model can be used in deterministic and probabilistic calculations. For deterministic calculations, only a single value for each input is needed, whereas for probabilistic simulations, statistical distributions for all input parameters are needed. In this section, statistical distributions for various inputs are derived. This is either done from the literature or using real offshore measurement data. Since not all possible parameters can be varied, the focus is on environmental conditions like wind, wave, and soil conditions, material parameters of the substructure, and local geometrical parameters of the substructure and foundation. Local geometrical parameters are, for example, fabrication tolerances. Global or larger changes of the geometry, resulting from design changes, are not analyzed. All parameters being investigated are summarized in Table 20. For soil properties, several values of the same parameter are applied, as the soil model consists of three different layers. The same applies to substructure components, as the substructure has various piles and braces with different wall thicknesses etc.

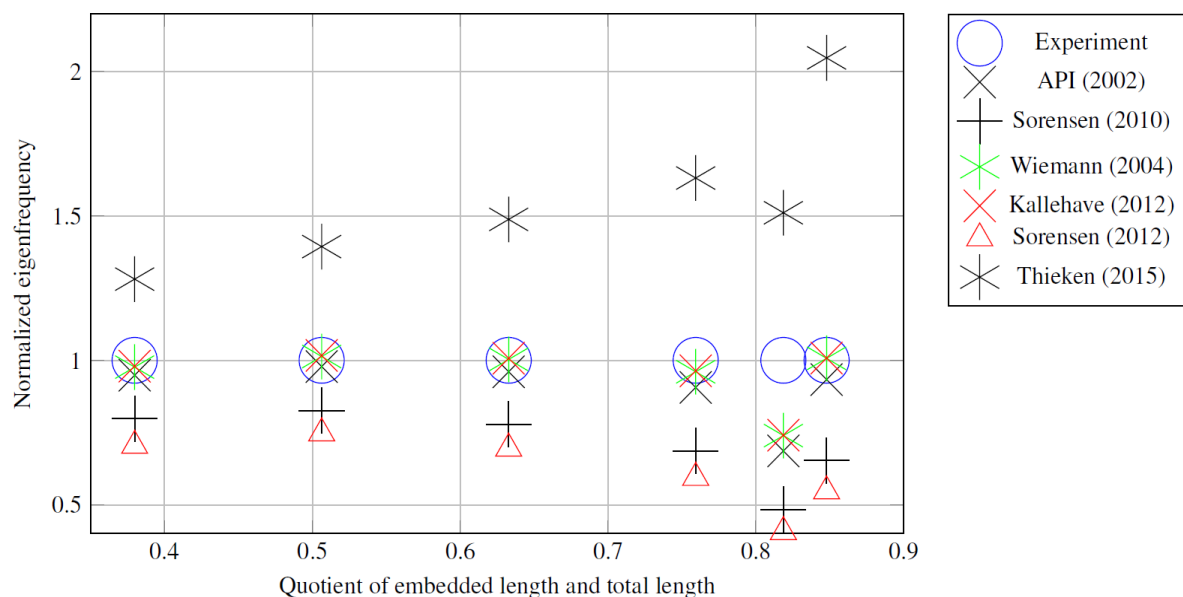


Figure 65: Normalized first bending eigenfrequencies of the piles with smaller diameter for different embedded lengths calculated using different soil models

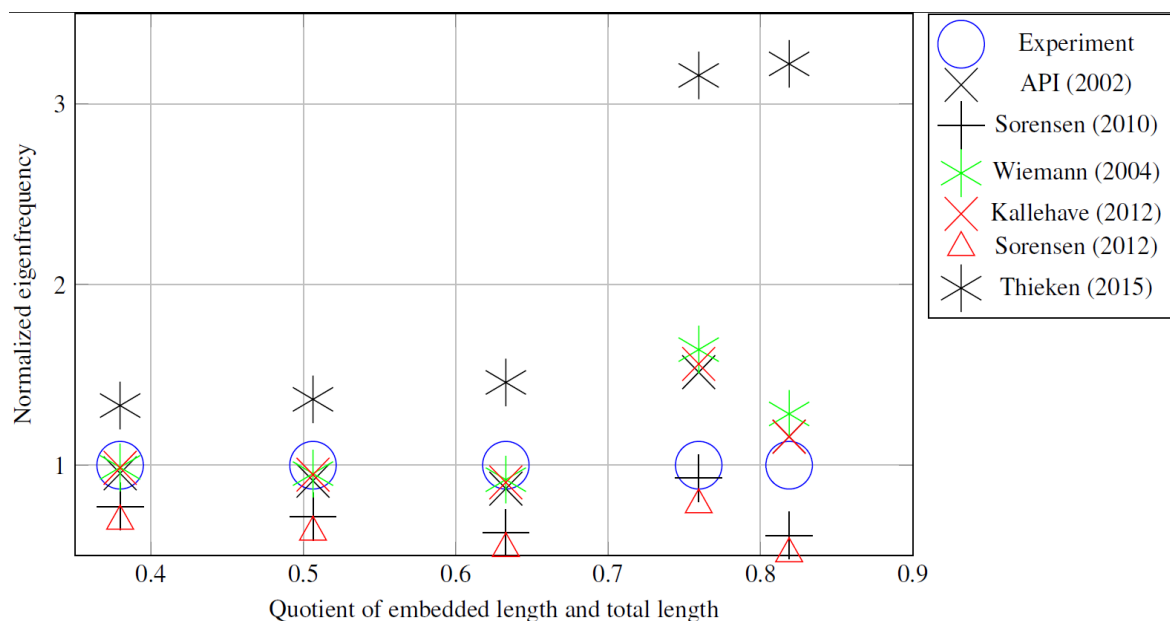


Figure 66: Normalized second bending eigenfrequencies of the piles with smaller diameter for different embedded lengths calculated using different soil models

Table 20: List of all parameters that are varied (MG: marine growth, SS: substructure, FD: foundation)

Wind	Wave	Soil	Material	Geometry
Wind speed	Water depth	Unit weight	Young mod. (SS)	Hub mass
Wind shear exp.	Water density	Friction angle	Poisson ratio (SS)	Nacelle mass
Wind direction	Wave height	Embedded length	Steel density (SS)	Platform mass
Air density	Wave direction	Relative density	Young mod. (FD)	Diameter (SS)
Turb. Intensity	Wave period	Cone tip resistance	Poisson ratio (FD)	Wall thickn. (SS)
Yaw error	MG thickness	Soil layer thickn.	Steel density (FD)	Diameter (FD)

Vertical flow angle    MG density    Shear modulus    Wall thickn. (FD)

To keep the model practicable and due to a lack of information, in most cases it is abstained from using correlated input parameters. For all inputs, statistical distributions were either derived from a literature research or real measurement data is used. Some distributions are given in Table 21. For further information, it is referred to (Hübler, et al., 2017) and (Hübler, et al., 2017), which are both based on the work in the IRPWIND project.

**Table 21: Parameter distributions**

Parameter	Unit	Distribution	Mean	CoV	Notes
Wind speed	m/s	Weibull (Wbl)	10.94	2.32	Values are Wbl parameters a and b
Water depth	m	Normal (N)	20	0.04	-
Air density	kg/m <sup>3</sup>	Bi-modal Gumbel	1.21	0.022	$\mu_2=1.25$ , $CoV_2=0.016$ and $p=0.87$
Wind direction	°	Kernel	-	-	No parametric fit appropriate
MG thickness	m	Uniform	-	-	0m to 0.2m
Soil lay. thickn. 1	m	Uniform	-	-	9m to 19m
Young mod. (SS)	GPa	Log-N (LN)	210	0.02	-
Friction angle 1	°	Truncated LN	33	0.15	29° to 45° (boundaries)
Vert. flow angle	°	Normal (N)	0	1	-
Diameter (SS)	m	Truncated N	0.06	0.1	0.0587m to 0.0613m (boundaries)

For wind and wave conditions, measurement data is available. Therefore, conditional probability distributions (i.e.  $P(Y = y|X = x)$  with  $X$  being the independent random variable,  $Y$  the dependent variable, and  $P$  the probability function) are derived directly from offshore measurement data. Distributions are determined for the wind speed, significant wave height, wave peak period, wind and wave direction, turbulence intensity, and the wind shear exponent using FINO3 data. FINO3 is a measurement mast in the North Sea, which is funded by the German Federal Ministry for Economic Affairs and Energy and “Projekträger Jülich”<sup>2</sup>. It is located 80km west of the island Sylt near to the wind farm DanTysk. Information on the available data and the conducted data processing can be found in (Hübler, et al., 2017). For reasons of simplicity, it is abstained from describing the data in detail. Several statistical distributions are fitted to the processed data using a maximum likelihood estimation. In case of several distinct peaks, multi-modal distributions are fitted as well. As some environmental inputs are conditioned by others, dependencies have to be defined. The dependencies and the selected distributions can be found in Table 22. One way to include dependencies in statistical distributions is to split up the data of the dependent parameters into several bins of the independent parameters. To illustrate this approach, for example, the wave peak period is fitted in several bins of 0.5m wave height (e.g.  $P(T_p) = P(T_p|1.5m \leq H_s < 2.0m)$ ). The bin widths for the dependent parameters are summarized in Table 22 as well.

Visual inspections and Kolmogorov-Smirnov tests are used to find the best fitting distribution for each parameter. For one parameter, if possible, only one distribution is chosen, i.e. the same type of distribution is applied in all bins of the same parameter.

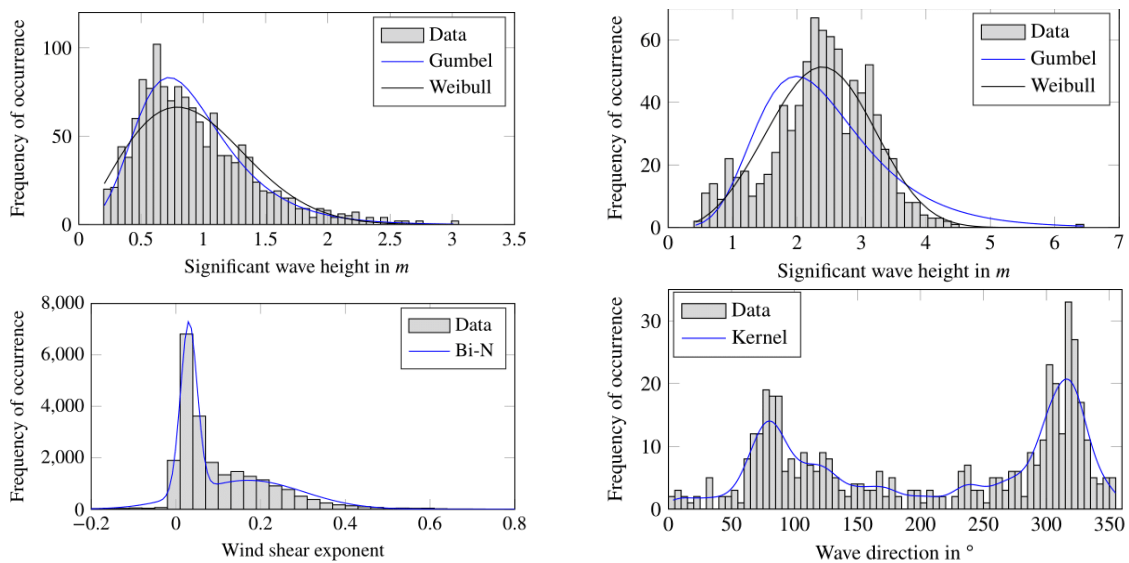
Directional parameters are continuous distributions ( $0^\circ=360^\circ$ ) and feature several peaks. Therefore, classical distributions can hardly fit the data, and a non-parametric kernel density estimation (KDE) is used to fit directional parameters.

Some resulting distributions are plotted in Figure 67. For further information it is referred to (Hübler, et al., 2017).

<sup>2</sup> Raw data of FINO3 is freely available for research purposes. See [www.fino3.de/en](http://www.fino3.de/en)

**Table 22: Conditional statistical distributions for environmental inputs derived from FINO3 data**

Parameter	Dependencies	Bin widths	Statistical distribution
Wind speed	-	-	Weibull
Wind direction	Wind speed	2m/s	Kernel (non-parametric)
Wave height	Wind speed	2m/s	Gumbel
Wave period	Wave height	0.5m	Bi-modal LN
Wave direction	Wave height and Wind direction	1.0m and 36°	Kernel (non-parametric)
Turb. Intensity	Wind speed	2m/s	Weibull
Wind shear exp.	Wind speed	2m/s	Bi-modal N


**Figure 67: Frequency distribution plots for different environmental conditions**

### 3.2.4 Sensitivity analysis

Taking Table 20 into account, it is obvious that the number of probabilistic parameters is fairly high. The computational effort of probabilistic calculations increases for higher numbers of probabilistic inputs. Furthermore, commonly, it can be assumed that the scattering of some parameters can be neglected and deterministic values can be used without losing significant accuracy. Therefore, it is valuable to identify those parameters that have to be treated in a probabilistic manner, and those that can be approximated with deterministic values. For this identification, global sensitivity analyses are used. In the literature, all different kinds of global sensitivity analyses can be found. A straightforward and the most frequently used approach is the one-at-a-time (OAT) analysis. The general concept of the OAT analysis is to vary one parameter while keeping all others fixed. In most cases, only maxima and minima of the parameters are tested. The OAT procedure has the advantage that the model has to be evaluated only a few times (two times the number of parameters). However, interactions between the parameters and non-linear effects of each parameter are completely neglected. On the other hand, approaches with enormous computational costs, like the plain variance-based sensitivity analysis (Saltelli, et al., 2008), exist. These approaches model all interactions and high-order effects. Therefore, for highly non-linear systems, it can be beneficial to utilize these sophisticated approaches. The challenge, in the context of offshore wind turbine modelling, is that the system behaves highly non-linear and, at the same time, the

computational effort of the numerical simulation is fairly high. The first fact suggests the use of variance-based methods and the second one of OAT analyses. To handle these two contradicting features, in this project, a new global sensitivity analysis was developed, published in (Hübler, et al., 2017), and evaluated in (Hübler, et al., 2017). The concept of this new approach is a stepwise selection. It starts with a OAT analysis and ends with a variance-based one. The general approach is illustrated in Figure 68. For the mathematical details, it is referred to (Hübler, et al., 2017). In this report, the four steps are concisely summarized, and subsequently, results of the conducted sensitivity analyses for a jacket and a monopile substructure are given.

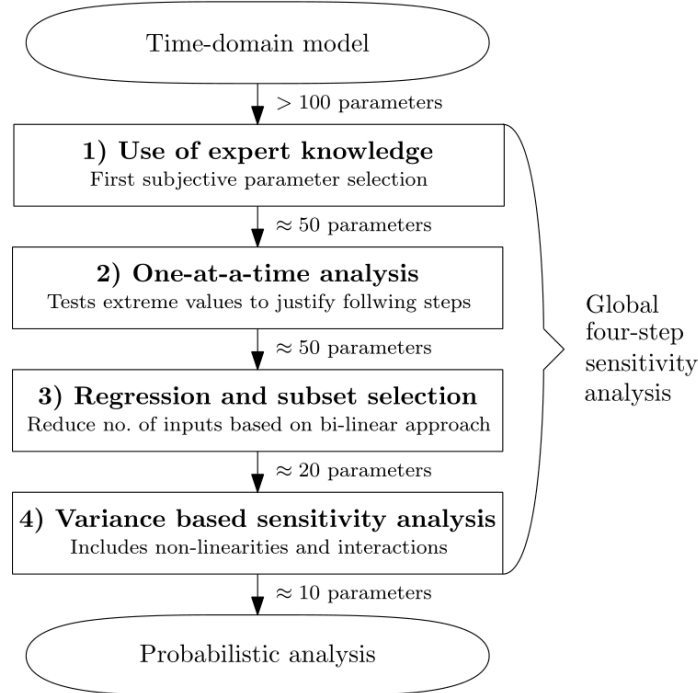


Figure 68: Scheme of the new global four-step sensitivity analysis (cf. (Hübler, et al., 2017))

Step one is a significant reduction of parameters by the use of expert knowledge and decision making. This step is highly subjective, but it is necessary to get a starting set of probabilistic parameters. The decision whether parameters are treated as deterministic is based on the expert knowledge and a broad literature research. Furthermore, the aspect of missing probabilistic data for some parameters is taken into account. Nevertheless, an isolated consideration of the probabilistic parameters is not possible. There are interactions of probabilistic inputs with deterministic values as well. For example, depending on the deterministic control algorithm, the effect of statistically distributed wind speeds is different.

Using this starting subset of probabilistic parameters, the second step is a OAT analysis. This step is intended to clarify whether further steps are valuable or the probabilistic subset cannot be reduced significantly. Only if some, but not nearly all, inputs are detected to be influential, additional steps are helpful. However, the second step does not reduce the probabilistic subset itself, as the neglect of interactions and high-order effects leads to a high risk of reducing the probabilistic subset too much and of not including influential, highly interactive parameters.

After having clarified that the probabilistic subset can be reduced, the third step is a regression analysis being combined with an automatized subset selection. The whole data space (not only maxima and minima) is analyzed using the regression. Furthermore, all

parameters are varied at the same time. However, regressions give only a (in this work bi-linear) approximation of the real simulation model. Due to the bi-linear approximation, high-order effects are neglected in this step, but some interaction effects are covered. A better alternative for this third step compared to the bi-linear regression is presented in (Hübler, et al., 2017). There, a kriging meta-model is proposed, and the better performance is shown.

The fourth and last step of the multi-step sensitivity analysis is a global variance-based sensitivity analysis. This analysis includes all non-linear high-order effects and interactions between all input parameters. Therefore, on the one hand, it conserves the whole complexity of the time domain model. On the other hand, it needs a large number of model evaluations, as conditional variances are analyzed. This means, the influence of keeping one factor fixed on the total variance is investigated. A variance-based analysis needs  $n \times (m + 2)$  model evaluations, with  $m$  being the number of inputs and  $n$  the number samples ( $>750$ ). This leads to more than 35,000 model evaluations for 50 parameters compared to 100 model evaluations for the OAT analysis ( $2 \times m$ ). The use of the four-step approach can reduce the number of model evaluation by a factor of about four compared to the plain variance-based approach without neglecting non-linear effects.

The proposed four-step approach is used to identify the significant probabilistic parameters of two substructures of offshore wind turbines (a jacket and a monopile substructure) and for different outputs (ultimate and fatigue loads). For details in the modelling and interim results, it is referred to (Hübler, et al., 2017). Here, only the overall and general conclusions concerning non-influential and the most important parameters are stated. For both substructures, only a very limited number of parameters is really influential. Some parameter, like the internal friction angle or the unit weight of the soil (for the monopile), influence all outputs, whereas others only influence either ultimate or fatigue loads. Resonance effects are highly influenced by soil and geometrical parameters. This can be concluded, as for soil and geometric parameters total effects are much higher than first order indices. This means that they exhibit interaction effects. For other parameters, like the air density, this is not the case. For these parameters, interaction is less pronounced. Furthermore, interaction effects are more relevant for the fatigue loads. After all, the parameters in Table 23 are the most influential ones for the monopile and the jacket, respectively. These parameters are, as shown, structure dependent. An additional slight site dependency is probable. Still, the most influential parameters in any case are five environmental conditions determining the wind and wave loads (wind speed and direction and wave height, period, and direction). At least these five parameters should always be treated in a probabilistic manner. So far, in most cases, only the two wind parameters are varied (by using several bins). The three wave inputs are only changed deterministically depending on the wind speed and are constant in each wind speed bin.

**Table 23: List of influential parameters for the monopile and the jacket selected using the four-step algorithm**

<b>Monopile</b>	<b>Jacket</b>
Wind speed	Wind speed
Wind direction	Wind direction
Significant wave height	Significant wave height
Wave peak period	Wave peak period
Wave direction	Wave direction
Soil friction angle 3	MG thickness
Soil unit weight 3	Water depth
MG thickness	Soil friction angle 3
Diameter foundation piles	Cone tip resistance 3
Relative density of the soil 3	Cone tip resistance 2
Soil unit weight 2	Soil unit weight 2
Embedded length	
Water depth	
Relative density of the soil 2	

### 3.2.5 Deterministic and probabilistic design

Fully coupled aero-elastic time domain simulations for offshore wind turbines are quite time-consuming, even if deterministic input parameters are assumed. If all sensitive parameters (c.f. Table 23) are treated probabilistically, simulations are not manageable in adequate computing times. This is the case, as for each “design” (i.e. variation of the original design due to the scattering of the soil/structural inputs) a high amount of simulations has to be conducted because of scattering loads (wind and wave inputs). Zwick and Muskulus (Zwick & Muskulus, 2015) showed that even if only some environmental conditions (for the load calculation) are assumed to be probabilistic, the uncertainty in fatigue damages is high and many simulations are needed. Hence, in this work, not all parameters, being determined to be sensitive, are utilized, but only the most important ones. Taking the first five parameters of Table 23, only load parameters are treated probabilistically. This allows a much more efficient probabilistic simulation, as only one “design” has to be simulated. Despite the simplification that structural and soil parameters are not varied, this procedure is still a significant improvement compared to the state of the art. So far, commonly, only different wind speeds (and random seeds for the consideration of the stochastic nature of wind and waves) are used. For each wind speed, all other conditions are assumed to be constant. Here, a full probabilistic and stochastic simulation for the load side with scattering wind speeds, wind directions, wave heights, wave directions, wave peak periods, turbulence intensities, and wind shear exponents (probabilistic aspect) and different random seeds for irregular waves and turbulent wind (stochastic aspect) is conducted. The outcomes of these probabilistic calculations are compared to the results of deterministic simulations (only different wind speeds and random seeds).

For offshore substructures being made of steel, in general, the fatigue limit state is decisive and not the ultimate limit state. This is why the focus of this work is on fatigue damages.

For the probabilistic model, the environmental inputs of Table 22 are used. Further information can be found in (Hübler, et al., 2018). For the deterministic one, in each wind speed bin, the mean value of the probabilistic model is applied, and aligned wind and wave directions are assumed, as it is done in (Zwick & Muskulus, 2015). These values are

summarized in Table 24. Furthermore, the following additional assumptions are made for both simulations:

- The turbulent wind field is calculated using the Kaimal model.
- The JONSWAP spectrum is utilized to compute irregular waves.
- The soil conditions of the OC3 phase II model (monopile) (Jonkman & Musial, 2010) are applied.
- Current, second-order and breaking waves, wave spreading effects, marine growth and degradation effects are not taken into account.

**Table 24: Environmental conditions for the deterministic case**

Wind speed (m/s)	2	4	6	8	10	12	14	16	18	20	22	24	26
Wind dir. (°)	0	0	0	0	0	0	0	0	0	0	0	0	0
Wind shear exp. (-)	-0,02	0,04	0,05	0,07	0,09	0,10	0,12	0,11	0,10	0,10	0,09	0,08	0,10
Turb. Int. (%)	12,0	7,3	5,8	5,2	5,0	4,9	5,2	5,5	5,9	6,2	6,6	7,0	7,5
Wave height (m)	0,84	0,89	1,01	1,23	1,51	1,82	2,19	2,68	3,20	3,73	4,38	4,98	5,83
Wave period (s)	7,15	7,13	7,15	7,11	7,18	7,38	7,65	8,12	8,67	9,24	9,98	10,7	11,6
Wave dir. (°)	0	0	0	0	0	0	0	0	0	0	0	0	0

The simulations are conducted using the simulation framework FASTv8 (Jonkman, 2013) of the “National Renewable Energy Laboratory” (NREL). The soil model that was developed in this project (see section 3.2.2.2) and applies soil structure interaction matrices at the base joints is used to enhance the FASTv8 code. The required soil matrices are based on non-linear spring models (p-y curves). In axial direction, the CPT method of FUGRO (API, 2007) is applied and in lateral the model of Kallehave et al. (Kallehave, et al., 2012). The decision for the lateral soil model is based on the experimental comparisons in section 3.2.2.3. Initial stiffnesses are assumed.

The NREL 5MW reference wind turbine (Jonkman, et al., 2009) with the OC3 monopile (Jonkman & Musial, 2010) as substructure is used. Simulation lengths of 10 minutes and lengths of initial transient (i.e. the lengths of the simulation that have to be removed to exclude all transients due to the start of a simulation) between 60 and 720 seconds, depending on the wind speed, are chosen according to (Hübler, et al., 2018).

The results of the time domain simulations using FAST are, inter alia, time series of forces, moments, and stresses for each element of the substructure. These time series are used for the fatigue damage analysis. The fatigue analysis is done according to Eurocode 3, part 1-9 (European Committee for Standardization, 2010). Here, a detail of 71MPa for butt welds (transversal welds) and an additional reduction due to a size effect ( $t > 25\text{mm}$ ) are assumed. Since for monopiles shear stresses ( $\tau$ ) are in most cases significantly lower than direct stresses ( $\sigma$ ), the normal stress transverse to the welds can be approximated as follows:

$$\sigma_{\perp} = \frac{F_z}{A} + \frac{\sqrt{M_x^2 + M_y^2}}{S}, \quad (107)$$

where,  $A$  and  $S$  are the cross section area and the section modulus, respectively. This approach is a conservative simplification, as the maximum normal stress ( $M = \sqrt{M_x^2 + M_y^2}$ ) is assumed independent of the wind direction. For all hot spot stresses, a Rainflow counting evaluates the stress cycles. A conservative linear damage accumulation according to the Palmgren-Miner rule is assumed, as recommended by the current standards. The damage ( $D_j$ ) for each time series ( $j$ ) is calculated using the number of cycles ( $n_k$ ) associated to a stress amplitude ( $\Delta\sigma_{\perp,k}$ ) and the endurance (maximum number of cycles;  $N_k$ ) for the same stress amplitude.  $K$  is the number of considered stress amplitudes:

$$D_j = \sum_{k=1}^K \frac{n_k}{N_k}, \quad (108)$$

The slope of the S-N curve is three before and five after the fatigue limit. This differs slightly from the Eurocode approach, where an additional cut-off limit at  $N = 10^8$  is presumed. The damage at each position of the substructure is calculated by adding up the resulting damages of all 10 minute time series, weighting them by their occurrence probability, and extrapolating them to 20 years lifetime (cf. Equation (109)). The overall lifetime damage of the substructure is determined by taking the maximum damage of all positions along the substructure. A detailed description of the damage calculations procedure is given in (Hübler, et al., 2018).

### 3.2.6 Damage distribution and failure probabilities

Due to the use of probabilistic input parameters the overall fatigue damage is scattering, and therefore, it subjected to high uncertainties, if limited sampling is applied, which is always the case due to limited computational resources. For a jacket substructure, Zwick and Muskulus (Zwick & Muskulus, 2015) already showed that, even for deterministic inputs (only different seeds and wind speeds) the error in fatigue damages due to finite sampling occurring with a probability of 1% (1% error) is up to 29%, if six 10min simulations are conducted. For probabilistic environmental states, scattering in each wind speed bin, a considerable increase in the uncertainty of the lifetime damage due to finite sampling is predicted. This increase is, for example, shown by Häfele et al. (Häfele, et al., 2017) (Häfele, et al., 2017). Therefore, a study of convergence to determine the number of simulations ( $N$ ) that is needed to determine the damage probability density function (PDF) with a certain reliability is conducted. For this purpose, 10000 simulations for the probabilistic case and 500 for the deterministic one are carried out in each wind speed bin. Subsequently, 10000 random combinations of  $N_{min} = 6$  up to  $N_{max} = 10000$  simulations ( $N_{max} = 500$  for the deterministic case) are selected using a bootstrapping procedure. The bootstrapping approach allows to approximate the uncertainty for different combination sizes. As the uncertainty depends on the wind speed, Figure 69 (right) shows the 1% error for the probabilistic case for all wind speeds and several combinations sizes. As a comparison, Figure 69 (left) displays the deterministic case. The highly differently scaled vertical axes should be noted.

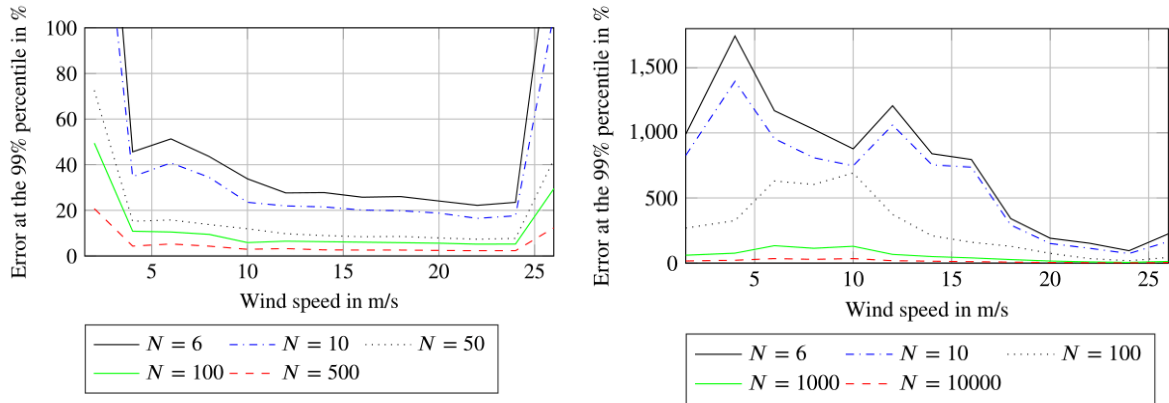
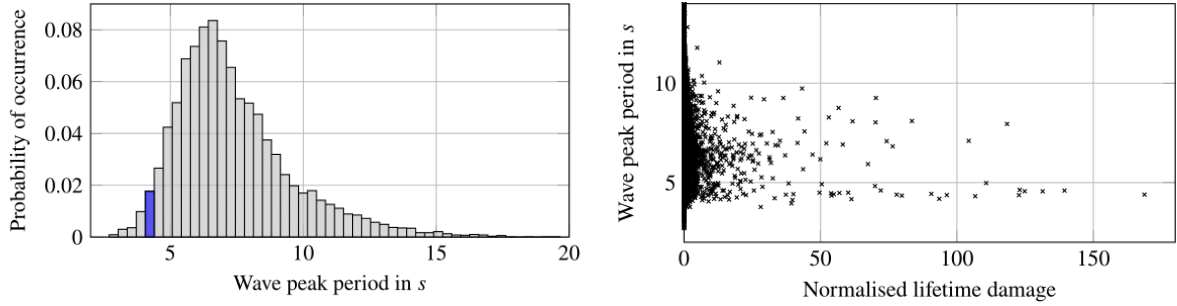


Figure 69: 1% error of the lifetime damage for different wind speeds and number of simulations for the deterministic case (left) and the probabilistic case (right)

The enormous amount of simulations ( $N > 1000$ ) needed for probabilistic case to reach small uncertainties is remarkable. A comparison with the deterministic conditions proves that this is a result of scattering environmental conditions, since for the deterministic case, simulation numbers of  $N = 50$  are mostly sufficient. As the high uncertainty increases computing times significantly, this effect is investigated in detail. At first, the scattering of the lifetime damage in one wind speed bin is analyzed. For example, for the wind speed of 11-13 m/s, 95% of the fatigue damages (for a single 10 minute simulation) are in the range of zero to three times the mean damage, but there are some rare values exceeding the mean by a factor of 100 and more. As outliers dominate the convergence behavior and influence the mean damage significantly, it is important to know the reasons for the scattering of the damage in each wind speed bin. The physical reason for these high damages is resonance. Monopiles with medium to large diameters are heavily influenced by wave loads. If waves excite the natural frequency of the wind turbine, high damages occur. The first eigenfrequency of the OC3 monopile is 0.25 Hz (Jonkman & Musial, 2010). Most wave peak frequencies are lower with 0.1-0.15 Hz (c.f. Table 24). However, for the probabilistic simulation approach, the environmental conditions scatter and higher wave peak frequencies occasionally occur. Figure 70 (left) displays the wave peak period distribution for wind speeds between 11 and 13 m/s. The rare occurrence of waves with a peak period of 4 s (0.25 Hz) is obvious. Figure 70 (right) illustrates that these rare resonance cases are the reason for the outliers of the fatigue damage, as the highest damages occur for peak periods of about 4 s. For  $T_p = 8$  s, being exactly double the eigenperiod, high fatigue damages might occur as well. This analysis makes clear that, firstly, the scattering of damages is higher, if probabilistic inputs are used, and secondly, higher mean damages occur for the probabilistic case.

Based on these findings, damage PDFs for the probabilistic and the deterministic case are computed. In a first step, the total lifetime damage has to be calculated. The total lifetime damage is the sum of the weighted damages over all wind speed bins ( $n_{bins}$ ) with a weighting according to the occurrence probability of the wind speeds  $p(v_s)$  and the overall lifetime in minutes ( $t_{lifetime}$ ):

$$D_{total} = \frac{t_{lifetime}}{10min} \sum_{i=1}^{n_{bins}} D_i p(v_s) \quad (109)$$



**Figure 70: Investigation of high uncertainties in fatigue damages by analyzing resonance effects. Wave peak period distribution (left) and wave peak period versus fatigue damage (right)**

As shown, damages in each wind speed bin scatter a lot. Therefore, to calculate an “extrapolated” lifetime damage ( $\bar{D}_{total}$ ),  $N_{max} = 10000$  ( $N_{max} = 500$  for the deterministic case) 10min damages in each wind speed bin are randomly chosen leading to an adaption of Eq. (109), where  $D_{i,j}$  is the 10min damage in wind speed bin  $i$  and sample  $j$ :

$$\bar{D}_{total} = \frac{t_{lifetime}}{10min} \sum_{i=1}^{n_{bins}} \left( \frac{1}{N_{max}} \sum_{j=1}^{N_{max}} D_{i,j} \right) p(v_s) \quad (110)$$

This procedure enables us to calculate an approximate of the total lifetime damage taking scattering load conditions into account. Nevertheless, this is still only one value. For the same conditions, other total lifetime damages are possible as well just by selecting other samples in the bootstrap algorithm. Hence, to calculate the damage PDF,  $p(\bar{D}_{total})$ , 10000 bootstrap re-samples of the total lifetime damage are drawn (i.e. Eq. (110) is evaluated 10000 times). The resulting PDFs for the deterministic and the probabilistic case are shown in Figure 71.

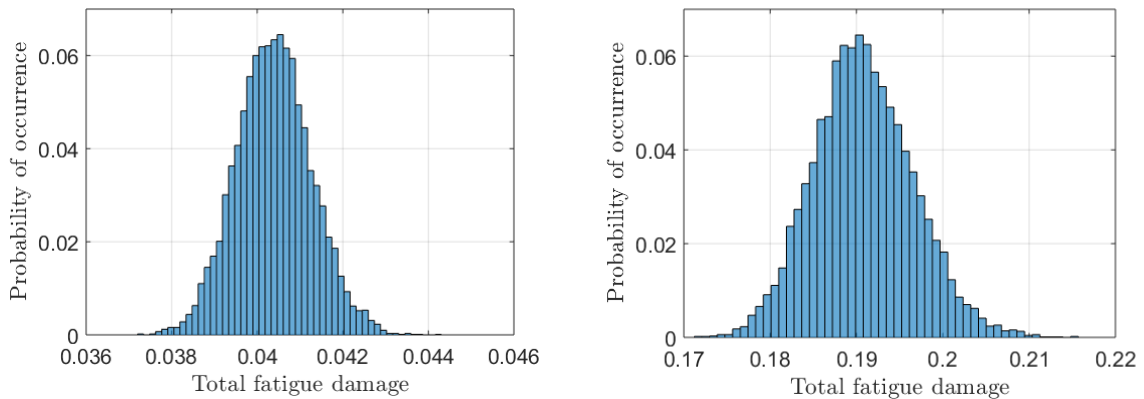


**Figure 71: PDFs of the total fatigue damage for the deterministic case (left) and the probabilistic one (right)**

It is apparent that the probabilistic case has much higher fatigue damages by a factor of about five. This higher fatigue damage is of substantial importance, as it shows that current deterministic designs are not always conservative and probabilistic approaches can lead to significantly smaller lifetimes. On the other hand, it makes clear that safety factors that are currently used and that guarantee safe designs even for underestimated damages as just shown might be significantly reduced, even if only partly probabilistic models, as done here, are applied. Using the current approach, at least one significant uncertainty factor (i.e. uncertainty due to limited sampling while scattering environmental

conditions are applied) is identified. It has to be mentioned that the computational effort of probabilistic approach is significantly higher. Here, twenty times more simulations were used.

### 3.2.7 Summary and conclusion

The general aim of the work, described in section 3.2, is to conduct probabilistic calculations of fully coupled offshore wind turbines to gain a first insight in the reliability of substructures, based on sophisticated, non-linear aero-elastic simulations. Furthermore, the objective was to create a basis for SF calibration, and to compare the results of deterministic simulations and probabilistic ones.

Although it has to be mentioned that several simplifications are applied, the general aim was achieved, and a comparison between probabilistic and deterministic simulations was conducted. The most important simplifications are the limited amount of probabilistic parameters (only wind and wave parameters), and the focus on fatigue loads. Both simplifications are legitimate in the first place, as the chosen probabilistic parameters are the most influential (see Section 3.2.4), and fatigue is design driving for OWT substructures in most cases. The comparison shows that probabilistic fatigue damages can be significantly higher than deterministic ones. As, in this study, the same SFs are applied for both types of analyses, it can be concluded that SFs can be massively reduced, if probabilistic calculations (probabilistic only in wind and wave inputs) are conducted. Furthermore, these results demonstrate a possible weight saving potential, as present structures are designed with deterministic approaches which, on the one hand, underestimate loads significantly, and on the other hand, are not leading to a significant amount of fatigue failures. Hence, there might be a significant load-bearing capacity reserve. A quantification of this weight saving potential is still pending and depends on future investigations concerning the SF calibration.

During the process of conducting probabilistic fatigue simulations (Hübler, et al., 2018) (Häfele, et al., 2017), several other results are achieved. Firstly, a soil model that incorporated the operation point of the turbine and that is suitable for probabilistic simulation was developed (Häfele, et al., 2016) (Hübler, et al., 2016). Secondly, based on soil structure interaction data received from WP7.2, an assessment of current p-y curves was conducted (Hübler, et al., 2018). It was found that present approaches are not sufficient for dynamic simulations, since none of the p-y models is able to predict eigenfrequencies accurately. Subsequently, a database for various probabilistic environmental conditions in the North Sea was created (Hübler, et al., 2017), and can be used in future research projects. And lastly, the most influential probabilistic parameters were identified using global sensitivity analyses (Hübler, et al., 2017) (Hübler, et al., 2017). It was shown that only a small amount of parameters, mainly wind and wave, and some soil parameters, have to be treated probabilistically.

After all, despite the simplification that were applied, the present probabilistic simulations are a solid basis for further investigations and for SF calibrations.

## 4. Failure statistics and current reliability level (Fraunhofer IEE)

Subject of this section is the reliability of offshore Support Structures. Due to the fact that no reliability data regarding Support Structures is publicly available yet, the present evaluation focusses on possible and occurring failure modes. As starting point, the first part provides an overview of different types of Support Structures and describes their structure according to RDS-PP®. Results on the reliability of wind turbines in general were published as an open access paper publication (Pfaffel, et al., 2017) and will not be described in this section. The only source covering failure rates of offshore support structures was published in 2015 by Carroll et al. (Carroll, et al., 2015) and states a failure rate of 0.185 failures per year for the tower and foundation in total. No major replacements were observed. Even though no distinction between foundations and towers is possible, support structures can be assumed to be quite reliable.

As Figure 72 depicts, there are several different Support Structure designs used in the offshore wind industry. However monopiles are used in most cases. More than 75 % of all installed wind turbines use monopiles. Except for gravity based foundations all Support Structures are steel constructions. While gravity based foundations (concrete structures) started with a high market share, only a few new gravity based foundations were added during the last years. Due to their low share of the market, concrete Support Structures are not considered in the evaluation.

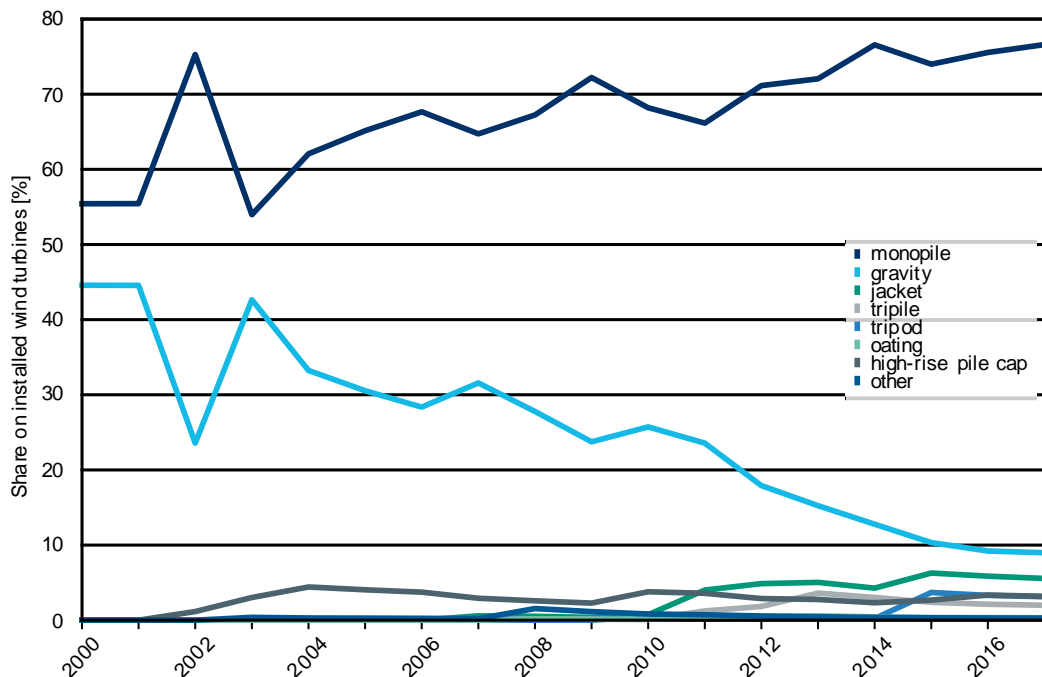


**Figure 72: Market share of different Support Structure designs based on all installed offshore wind turbines**

Caused by a lack of operational experiences and available data, no statistical reliability evaluation of the Support Structures is possible. Nevertheless, the most important failure modes as discussed in the literature are introduced. It is noticed that the focus regarding

Support Structures during operation and maintenance has to be on biofouling, corrosion, scour and the grout connection.

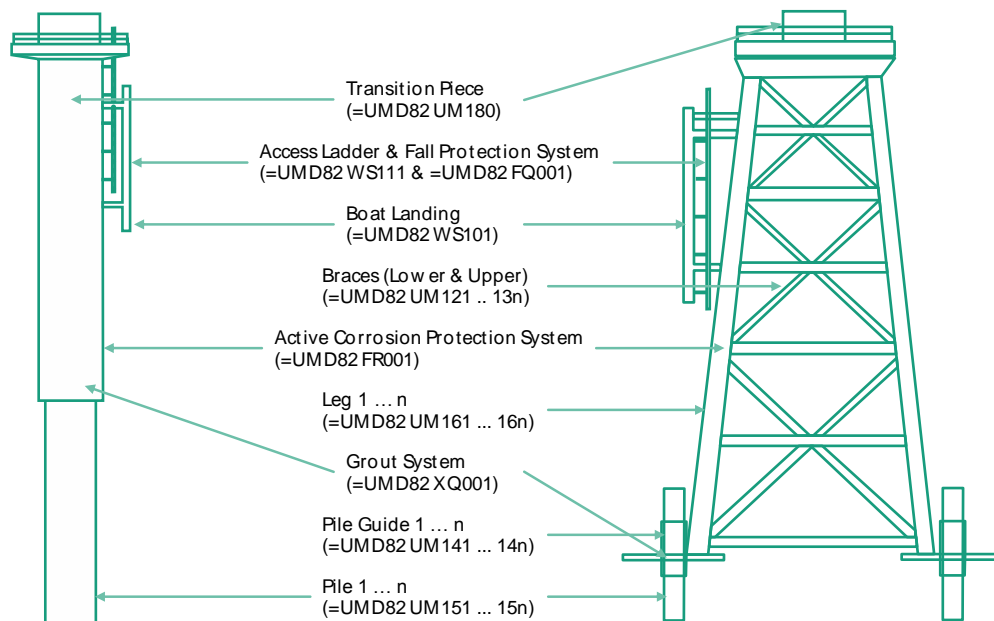
#### 4.1 Design and System Boundary of Support Structures (Fraunhofer IEE)

Figure 73 shows a monopile structure and a jacket structure which very well represent the different Support Structure (=UMD82) designs used in the offshore wind industry. Being welded from many parts the design of jackets, tripods and tripiles is much more complex compared to monopiles. Nevertheless the functional structure according to RDS-PP® is quite similar.

By driving piles into the seabed, a connection to the ground is achieved. As indicated by the name, the monopile consist of one big Pile (=UMD82 UM151) which is driven into the seabed and reaches up to the water surface where the Grout System (=UMD82 XQ001) connects it to the so-called Transition Piece (=UMD82 UM180). The Transition Piece connects the Support Structure to the tower of the wind turbine.

In case of the jacket three to four Piles (=UMD82 UM151 ... 154) are driven into the seabed and only a short length rises up from the soil and is connected to the Pile Guides (=UMD82 UM141 ... 14n) of the jacket structure by the Grout System. In-between the jacket consist of three to four Legs (=UMD82 UM161 ... 16n) as well as of Lower and Upper Braces (=UMD82 UM121 .. 13n) connecting the single Legs to increase the structural strength of the whole construction.

To enable access to the wind turbine both designs comprise a Boat Landing (=UMD82 WS101) as well as an Access Ladder & Fall Protection System (=UMD82 WS111 & =UMD82 FQ001). In order to reach the planned life time, many structures feature an Active Corrosion Protection System (=UMD82 FR001).



**Figure 73: Basic designation of Structural Steel Foundations (=UMD82) according to the RDS-PP® guideline**

## 4.2 Failure Modes of Support Structures (Fraunhofer IEE)

The lifetime of Support Structures mainly depends on the different loads the structure has to bear and is also influenced by environmental conditions such as wind, waves and currents, UV radiation, salty water and salty air. (Heins, 2011) Support Structures are designed to bear loads induced by the wind turbine through the tower as well as to withstand loads due to wind and wave conditions. To ensure the structural integrity of the Support Structure, it is required that design assumptions regarding the condition of the structure persist. Known issues are biofouling, corrosion, scour and faulty grout connections.

Loads on the tower, which are passed on to the Support Structure, are described in (Toft & Sørensen, 2008) and caused by loads due to normal operation, by wake effects from surrounding wind turbines and by extreme wind conditions. (Chella, et al., 2012) discuss impact forces on the Support Structure due to waves. Experiences at the Fino 1 research platform in the North Sea show that extreme waves are a real-world problem. During the 1st November 2006 the platform was hit by waves having significant wave heights of up to 10.54 m. The storm caused heavy damage to a walkway where floor gratings were torn from their mountings and also parts of the railings were heavily demolished. The Support Structure (jacket) itself remained undamaged (Herklotz, n.d.).

These loads can be also influenced by vegetation (biofouling) growing on the surface of the Support Structure which causes additional weight and leads to a change of the natural frequency and drag due to an increased circumference of the Support Structure (Böttcher, 2013). At the research wind farm alpha ventus fouling biomass of about 25 kg per square meter at a water depth of 1 m was found two years after installation while at water depth of 5 m and 10 m fouling barely exceeded 1 kg per square meter. Based on experience from the Fino 1 platform the authors expect a further weight increase at a water depth of 1 m while no mass grow is expected in deeper waters. (Gutow & etal, 2014)

The most important threat to the structural strength of steel-based Support Structures is corrosion. Salty air and water as well as wetting-drying cycles make Support Structures prone to corrosion. Thus corrosion protection is vital for Support Structures. To choose the suitable corrosion protection systems, the Support Structure has to be divided into splash zone, wet and dry zone and immersed zone. (Böttcher, 2013) and (Momber, et al., 2009)

Due to frequent contact to air and oxygen enriched seawater the splash zone and especially welding seams show the highest corrosion potential (Ciang, et al., 2008). For corrosion protection in the splash zone as well as in the wet and dry zone, various coating systems (passive corrosion protection) are available and further research (e.g. (WeserWind, B., 2015)) is carried out. Additional requirements to the coating systems result from mechanical impact damages caused e.g. by docking workboats as well as by scrubbing or loose and swinging parts. (DONG, 2009) Corrosion also occurs in sections where the coating is missing or was not applied properly. According to (Momber, n.d.) screws are also frequently affected by corrosion as well as sections of worn-out coatings (e.g. walkways). (Momber, n.d.)

Within the immersed zone no coating is applied and the Support Structure is made of bare steel. In this case active corrosion protection systems are utilized which can be either based on a galvanic sacrificial anode (zinc or aluminum) as used at the EnBW Baltic 1

wind farm or realized as a cathodic corrosion protection using an external current as used at the alpha ventus test site. In general corrosion protection systems are similar to systems used in the shipping industry or the Oil & Gas sector (Heins, 2011).

Regarding the structural integrity of the Piles, scour is also an issue for Support Structures due to increasing strains and a reduction of the natural frequency (Böttcher, 2013). As van der Tempel shows (Tempel, 2006), lifetime fatigue damage is increasing with increasing scour depth. In a worst case scenario deep scour can also threaten the stability of the whole Support Structure. At the research wind farm alpha ventus scour depths of at maximum 7.2 m (October 2013) were detected. After an rapid increase of the scour depth during the first 3 to 5 months after installation, the later development continued much slower (Kühn, 2013). Scour protection systems can be utilized to avoid or reduce scour. One opportunity is to place rocks around the Support Structure which are too heavy to be washed away (Tempel, et al., 2004). An alternative solution are geotextile sand containers (Heerten & Peters, 2011). For monitoring purposes scour depths can be evaluated using single beam or multi beam echosounder measurements (Kühn, 2013).

The Grout System connects on or more Piles to the rest of the Support Structure by filling the distance between the inner and outer tube with cement. In 2009 slipping of grout connections between monopiles and transition pieces was detected for the first time in offshore wind (Lochte-Holtgreven & Bechtel, 2014). The offshore industry solved this problem by installing additional elastomeric bearings at the concerned wind turbines. As a preventive measure this solution is also installed at newly erected wind turbines (lorc.dk, 2012). Displacement sensors can be used to monitor the grout connection during operation (Weijtjens, 2014).

With growing experience from operation and maintenance of offshore wind farms the main impact factors and failure modes will be better understood and quantitative statements for this critical structural component will be possible.

## 5. References

- Achmus, M., 2011. Bemessung von Monopiles für die Gründung von Offshore-Windenergieanlagen - Konzepte und offene Fragen. *Bautechnik* 88, pp. 602-616.
- Achmus, M. & Müller, M., 2010. Evaluation of pile capacity approaches with respect to piles for wind energy foundations in the North Sea. In: *Frontiers in Offshore Geotechnics Two*. s.l.:CRC Press.
- American Petroleum Institute, 2002. *Recommended Practice for Planning, Designing and Constructing Fixed Offshore Platforms - Working Stress Design. Recommended Practice RP 2A-WSD*, s.l.: s.n.
- American Petroleum Institute, 2014. *Geotechnical and Foundation Design*, s.l.: s.n.
- API, 2007. *Errata and Supplement 3 - API Recommended Practice 2A-WSD, Recommended Practice for Planning, Designing, Constructing Fixed Offshore Platforms - Working Stress Design*, s.l.: s.n.
- Bea, R. G., Jin, Z., Valle, C. & Ramos, R., 1999. Evaluation of Reliability of Platform Pile Foundations. *Journal of Geotechnical and Geoenvironmental Engineering*, 128(8), pp. 696-704.
- Böttcher, J., 2013. *Jörg, Handbuch Offshore-Windenergie: Rechtliche, technische und wirtschaftliche Aspekte*, s.l.: s.n.
- BOWNESS, D. & M.M.K., L., 2002. *Fracture mechanics assessment of fatigue cracks in offshore tubular structures. HSE Offshore Technology Report 2000/077 for HSE, EPSRC, and Chevron Oil.*, London: The Stationery Office.
- BS 7910, 2013. *Guide to methods for assessing the acceptability of flaws in metallic structures.*, London: British Standards Institution.
- Carroll, J., McDonald, A. & McMillan, D., 2015. Failure rate, repair time and unscheduled O&M cost analysis of offshore wind turbines. *Wind Energy*.
- Cathie, D., 2012. *Offshore pile design according to international practice*. s.l.:Free published presentation.
- CEB-fip, 2013. *fib Model Code for concrete structures2010*. Lausanne: Ernst & Son.
- Chella, M. A., A., T. & Myrhaug, D., 2012. An Overview of Wave Impact Forces on Offshore Wind Turbine Substructures. *Energy Procedia*, Volume 20, p. 217-226.
- Chen, J.-Y. & Gilbert, R., 2014. Insights into the Performance Reliability of Offshore Piles Based on Experience in Hurricanes. *From Soil Behavior Fundamentals to Innovations in Geotechnical Engineering*, pp. 283-292.
- Chen, J.-Y.et al., 2009. Analyses of Pile Capacity for Offshore Structures in Hurricane Katrina. *Contemporary Topics in Deep Foundations*, ASCE, pp. 239-246.
- Ciang, C. C., Lee, J.-R. & Bang, H.-J., 2008. Structural health monitoring for a wind turbine system: A review of damage detection methods. *Meas. Sci. Technol.*, 19(12), p. 122001.
- Cornelissen, H. A. W., 1984. *Fatigue Failure of Concrete in Tension*, Delft: HERON.
- Craig Jr., R. R. & Bampton, M. C. C., 1968. Coupling of Substructures for Dynamic Analyses. *AIAA Journal* 6 (7), pp. 1313-1319.
- Dallyn, P., El-Hamalawi, A., P. A. & K. R., 2015. Experimental testing of grouted connections for offshore substructures: A critical review.. *Structures*, Volume 3, pp. 90-108.
- Damiani, R., Jonkman, J., Robertson, A. & Song, H., 2013. *Assessing the Importance of Nonlinearities in the Development of a Substructure Model for the Wind Turbine CAE Tool FAST*. Nanted, s.n.

- De Wries, W. & et.al, 2011. *Support Structure Concepts for Deep Water Sites. UpWind Project Deliverable Report D4.2.8*, s.l.: UpWind.
- DIN 1054, 2010. *Baugrund-Sicherheitsnachweise im Erd und Grundbau*, s.l.: Deutsches Institut für Normung.
- DIN EN 61400-3, 2010. *Windenergieanlagen - Teil 3-1: Auslegungsanforderungen für Windenergieanlagen auf offener See*, s.l.: Deutsches Institut für Normung.
- Dithinde, M., Phoon, K., DeWet, M. & Retief, J., 2011. Characterization of the Model Uncertainty in the Static Pile Design Formula. *Journal of Geotechnical and Geoenvironmental Engineering*, 137(1), pp. 70-85.
- DNV GL, 2015. *RP-C 210. Probabilistic methods for planning of inspection for fatigue cracks in offshore Structures.* s.l., DNVGL.
- DNVGL-RP-0419, 2016. *Analysis of grouted connections using the finite element method – Recommended Practice.*, Copenhagen: Det Norske Veritas.
- DNVGL-ST-0126, 2016. *Support structures for wind turbines*, s.l.: DNVGL.
- DNVGL-ST-C502, 2017. *Offshore Concrete Structures*, s.l.: DNVGL.
- DNV-RP-C203, 2011. *Fatigue Design of Offshore Steel Structures, Recommended practice*, s.l.: Det Norske Veritas.
- DONG, 2009. *Korrosionsschutz in der maritimen Technik*, Copenhagen: Wind Kraft Journal.
- Eurocode 0, 2010. *DIN EN 1990: Eurocode: Grundlagen der Tragwerksplanung*, s.l.: Deutsches Institut für Normung.
- European Committee for Standardization, 2010. *Eurocode 3: Design of steel structures – Part 1-9: Fatigue*, s.l.: EN 1993-1-9.
- Germanischer Lloyd, 2005. *Rules and Guidelines, IV Industrial Services, Guideline for the Certification of Offshore Wind Turbines*, s.l.: Germanischer Lloyd Wind Energie GmbH.
- Gilbert, R. & Tang, W., 1995. *Model Uncertainty in Offshore Geotechnical Reliability*. Houston, USA, s.n.
- Guyan, R. J., 2065. Reduction of stiffness and mass matrices. *AIAA journal* 3.2, p. 380.
- Gutow, L. & etal, 2014. *Rapid increase of benthic structural and functional diversity at the alpha ventus offshore test site,* in *Ecological research at the Offshore Windfarm alpha ventus: Challenges, results and perspectives,*, Wiesbaden: Springer.
- Häckel, M. & Rolfes, R., 2013. Monitoring a 5MW offshore wind energy converter-Condition parameters and triangulation based extraction of modal parameters. *Mechanical Systems and Signal Processing*, 40(1), pp. 322-343.
- Häfele, J., Hübler, C., Gebhardt, C. G. & Rolfes, R., 2016. An improved two-step soil-structure interaction modeling method for dynamical analyses of offshore wind turbines. *Applied Ocean Research*, 55, pp. 141-150.
- Häfele, J., Hübler, C., Gebhardt, C. G. & Rolfes, R., 2017. A comprehensive fatigue load set reduction study for offshore wind turbines with jacket substructures. *Renewable Energy*.
- Häfele, J., Hübler, C., Gebhardt, C. G. & Rolfes, R., 2017. *Efficient Fatigue Limit State Design Load Sets for Jacket Substructures Considering Probability Distributions of Environmental States*. San Francisco, s.n.
- Hald, T. et al., 2009. *Revisiting monopile design using py curves. Results from full scale measurements on Horns Rev.* s.l., s.n.
- Hansen, M. et al., 2015. *Probabilistic Safety Assessment of Offshore Wind Turbines (PSA-OWT)*, s.l.: Leibniz Universität Hannover.

Heerten, G. & Peters, K., 2011. Kolkschutz für Offshore-Windenergieanlagen in der Nordsee. *geotechnik*, 34(1), p. 51–58.

Heins, O., 2011. *Korrosionsschutz von Offshore-Windenergieanlagen: Einteilung, Normung und praktische Erfahrungen..* [Online] Available at: [http://www.htg-online.de/fileadmin/user\\_upload/korrosionsfragen/downloads/HTG-Kongress\\_Wuerzburg\\_09-09-2011/HTG-2011\\_Korrosion](http://www.htg-online.de/fileadmin/user_upload/korrosionsfragen/downloads/HTG-Kongress_Wuerzburg_09-09-2011/HTG-2011_Korrosion)

Herklotz, K., n.d. *Oceanographic Results of Two Years Operation of the First Offshore Wind Research Platform in the German Bight - FINO1.*, s.l.: s.n.

Holicky, M., Markova, J. & Gulvanessian, H., 2007. *Code Calibration Allowing for Reliability Differentiation and Production Quality.* London, s.n.

Hübler, C., Gebhardt, C. G. & Rolfes, R., 2017. Development of a comprehensive database of scattering environmental conditions and simulation constraints for offshore wind turbines. *Wind Energy Science*, pp. 491-505.

Hübler, C., Gebhardt, C. G. & Rolfes, R., 2017. Hierarchical Four-Step Global Sensitivity Analysis of Offshore Wind Turbines Based on Aeroelastic Time Domain Simulations. *Renewable Energy*.

Hübler, C., Gebhardt, C. G. & Rolfes, R., 2018. Methodologies for fatigue assessment of offshore wind. *Wind Energy*.

Hübler, C., Häfele, J., C.G., G. & Rolfes, R., 2018. Experimentally supported consideration of operating point dependent soil properties in coupled dynamics of offshore wind turbines. *Marine Structures*, p. 18e37.

Hübler, C., Häfele, J., Ehrmann, E. & Rolfes, R., 2016. *Effective consideration of soil characteristics in time domain simulations of bottom fixed offshore wind turbines.* Rhodos, s.n.

Hübler, C., Müller, F., Gebhardt, C. G. & Rolfes, R., 2017. *Global Sensitivity Analysis of Offshore Wind Turbine Substructures.* Dresden, s.n.

Yang, Z., Jardine, R., Guo, W. & Chow, F., 2015. A new openly accessible database of tests on piles driven in sands. *Géotechnique Letters*, Volume 5, pp. 12-20.

IEC 61400-1, 2017. *IEC 61400-1. Wind turbines – Part 1: Design requirements. 4th edition*, Geneva: IEC.

IEC 61400-6, 2017. *IEC 61400-6 Wind Energy Generation Systems – Part 6: Tower and Foundation Design Requirements*, Geneva: FDIS .

International Electrotechnical Commission, 2009. *Wind turbines - Part 3. 2009. Design requirements for offshore wind turbines, Standard IEC-61400-3:2009, EN 61400-3*, s.l.: s.n.

Jamiolkowski, M., Ghionna, V., Lancellotta, R. & Pasqualini, E., 1988. *New Correlations of Penetration Tests for Design Practice.* Orlando, s.n.

Jardine, R., Chow, F., Overy, R. & Standing, J., 2005. *ICP design methods for driven piles in sands and clays.* London: Thomas Telford Publishing.

JCSS , 2012. *Probabilistic Model Code - PART 3.12 Fatigue properties for metallic structures. Draft .*, s.l.: Joint Committee for Structural Safety.

Jonkman, J., 2013. The New Modularization Framework for the FAST Wind Turbine CAE Tool. *51st AIAA Aerospace Sciences Meeting, including the New Horizons Forum and Aerospace Exposition.*

Jonkman, J., Butterfield, S., Musial, W. & Scott, G., 2009. *Definition of a 5MW Reference Wind Turbine for Offshore System Development*, s.l.: National Renewable Energy Laboratory.

Jonkman, J. & Musial, W., 2010. *Offshore Code Comparison Collaboration (OC3) for IEA Task 23 - Offshore Wind Technology and Deployment*. Tech. Rep. NREL/TP-5000-48191, s.l.: National Renewable Energy Laboratory.

Jonkman, J. et al., 2012. *Offshore Code Comparison Collaboration Continuation (OC4), Phase I - Results of Coupled Simulations of an Offshore Wind Turbine with Jacket Support Structure*. Rhodos, s.n.

Kallehave, D., LeBlanc Thilsted, C. & Liingaard, M., 2012. *Modification of the API p-y formulation of initial stiffness of sand*. London, s.n.

Kirsch, F., Richter, T. & Coronel, M., 2014. Geotechnische Aspekte bei der Gründungsdimensionierung von Offshore-Windenergieanlagen auf Monopfählen mit sehr großen Durchmessern. *Ernst & Sohn Verlag für Architektur und technische Wissenschaften GmbH & Co. KG, Berlin · Stahlbau Spezial 2014 – Erneuerbare Energien*.

Kühn, B., 2013. *Geological research at alpha ventus: The spatiotemporal development of scours*, s.l.: Alpha Ventus.

Kulhawy, F. & Mayne, P., 1990. *Manual on Estimating Soil Properties for Foundation Design*. s.l.: Electric Power Research Institute.

Lantsoght, E., 2014. *Fatigue of concrete under compression - Database and proposal for high strength concrete*. Report nr. 25.5-14-04, Delft: Delft University of Technology.

Lehane, B., Schneider, J. & Xu, X., 2005. *review of design methods for offshore driven piles in siliceous sand*, s.l.: University of Western Australia Geomechanics Group.

Lindley, D. V., 1976. *Introduction to Probability and Statistics from a Bayesian Viewpoint, Vol. 1\_2*. Cambridge: Cambridge University Press.

Lochte-Holtgreven, S. & Bechtel, A., 2014. Grout-Verbindungen in Monopile-Tragstrukturen von Offshore-Windenergieanlagen. *Stahlbau*, 83(4), pp. 273-277.

lorc.dk, 2012. *Overcoming problems with crumbling grout*. [Online] Available at: <http://www.lorc.dk/oceanwise-magazine/archive/2012-2/overcoming-problems-with-crumbling-grout>

Lotsberg, I., 2013. Structural mechanics for design of grouted connections in monopile wind turbine structures.. *Marine Structures*, Volume 32, p. 113–135.

Madsen, C., Kragh-Poulsen, J., Thage, K. & Andreassen, M., 2017. *Analytical and numerical investigation of bolted steel ring flange connection for offshore wind monopile foundations*. Stavanger, Norway, First Conference of Computational Methods in Offshore Technology.

Momber, A., n.d. *Inspektion und Reparatur von Offshore-Wind-Konstruktionen*, s.l.: Muehlhan AG.

Momber, A., Plagemann, P., Stenzel, V. & M., S., 2009. Beurteilung von Korrosionsschutzsystemen für Offshore-Windenergietürme - Teil 1: Problemstellung und Versuchsdurchführung. *Stahlbau*, 78(4), pp. 259-266.

Natarajan, A. & Holley, W., 2008. Statistical extreme load extrapolation with quadratic distortions for wind turbines.. *Journal of solar Energy Engineering (031017)*, Volume 130, pp. 1-7.

Pfaffel, S., Faulstich, S. & K., R., 2017. Performance and Reliability of Wind Turbines: A Review. *Energies*, 10(11), p. 1904.

Phoon, K. & Kulhawy, F., 1999. Characterization of geotechnical variability. *Canadian Geotechnical Journal*, Volume 36, pp. 612-624.

Rodriguez, A. et al., 2018. *DEVELOPMENT OF NEW METHODOLOGIES TO ASSESS THE STRUCTURAL INTEGRITY OF THE GROUTED JOINT OF A 10 MW WIND TURBINE SUBSTRUCTURE*. Madrid, OMAE, p. 12.

- Saltelli, A. et al., 2008. *Global sensitivity analysis: the primer*. s.l.:John Wiley & Sons.
- Santos, B. et al., 2017. *D7.21. Report on Validation of design of grouted joints*, Brussels: IRPWIND.EU.
- Schaumann, P., Lochte-Holtgreven, S. & Eichstadt, R., 2013. *Numerical investigation on local degradation and vertical misalignment of grouted joint in monopile foundations..* Anchorage, Alaska, USA., ISOPE 2013.
- Schittkowski, K., 1986. NLPQL: A FORTRAN Subroutine Solving Non-Linear Programming Problems. *Ann. Operat. Res.*, 5, p. 485–500.
- Schmoor, K., 2017. *Probabilistische Analyse zum Sicherheitsniveau von Offshore-Gründungspfählen (PhD Thesis)*, s.l.: Institute for Geotechnical Engineering, Leibniz University Hannover.
- Schneider, J., Xu, X. & Lehane, B., 2008. Database Assessment of CPT-Based Design Methods for Axial Capacity of Driven Piles in Siliceous Sands. *Journal of Geotechnical and Geoenvironmental Engineering*, 134(9), pp. 1227-1244.
- Simpson, B., 2012. *Eurocode 7: Fundamental issues and some implications for users*. s.l., s.n.
- Slot, R. & Andersen, T., 2014. *Fatigue behavior and reliability of high strength concrete*. MSc thesis, Aalborg: Aalborg University.
- Sørensen, J. & Toft, H., 2014. *Safety Factors – IEC 61400-1 ed. 4 - background document.*, Copenhagen: DTU Wind Energy.
- Sørensen, S., 2012. *Soil-structure interaction for non-slender, large-diameter offshore monopiles*. PhD Thesis, Aalborg University Denmark, Department of Civil Engineering: s.n.
- Sørensen, S. P. H., Ibsen, L. B. & Augustesen, A. H., 2010. Effects of diameter on initial stiffness of p-y curves for large-diameter piles in sand. *Numerical Methods in Geotechnical Engineering*.
- Tempel, J. v. d., 2006. *Design of support structures for offshore wind turbines*. [S.l.: s.n.], op. 2006., s.l.: s.n.
- Tempel, J. v. d., Zaaier, M. & Subroto, H., 2004. *The effects of Scour on the design of Offshore Wind Turbines.*, Delft: TU Delft.
- Thieken, K., Achmus, M. & Lemke, K., 2015. A new static p-y-approach for piles with arbitrary dimensions in sand. *Geotechnik* 38 (4).
- Toft, H. S. & Sørensen, J. D., 2008. *Reliability Analysis of Wind Turbines*, Aalborg: Aalborg university.
- VanOverschee, P. & DeMoor, B., 1991. Subspace algorithms for the stochastic identification problem. *Decision Control*, Volume 2, p. 1321–1326.
- Wandji, W., Natarajan, A. & Dimitrov, N., 2018. Probabilistic structural assessment of conical grouted joint using numerical modelling.. *Journal of Ocean Engineering*, p. Under Review.
- Weijtjens, W. e., 2014. *Monitoring of offshore turbines for design and O&M: an overview of the activities of OWI-Lab*, s.l.: OWI-Lab.
- WeserWind, B., 2015. *KOWIND*, Hannover: TIB - Technische Informationsbibliothek Universitätsbibliothek Hannover.
- Wiemann, J., Lesny, K. & Richwien, W., 2004. *Evaluation of the Pile Diameter Effects on Soil-Pile Stiffness*. s.l., s.n.
- Zaaier, M. B., 2006. Foundation modelling to assess dynamic behaviour of offshore wind turbines. *Applied Ocean Research* 28.1, pp. 45-57.

Zwick, D. & Muskulus, M., 2015. The simulation error caused by input loading variability in offshore wind turbine structural analysis. *Wind Energy*, Issue 18, pp. 1421-1432.